

CFD Based Analysis and Parametric Study of a Novel Wind Turbine Design: the Dual Vertical Axis Wind Turbine

Gabriel Naccache

A Thesis

In the Department

Of

Mechanical and Industrial Engineering

Presented in Partial Fulfillment of the Requirements

For the Degree of

Master of Applied Science (Mechanical Engineering) at

Concordia University

Montreal, Quebec, Canada

August 2016

© Gabriel Naccache, 2016

CONCORDIA UNIVERSITY

School of Graduate Studies

This is to certify that the thesis prepared

By: Gabriel Naccache

Entitled: CFD Based Analysis and Parametric Study of a Novel Wind Turbine Design: the Dual Vertical Axis Wind Turbine

and submitted in partial fulfillment of the requirements for the degree of

Master of Applied Science (Mechanical Engineering)

complies with the regulation of the University and meets the accepted standards with respect to originality and quality.

Signed by the final Examining Committee:

Onur Kuzgunkaya Chair

Liangzhu Wang Examiner

Wahid Ghaly Examiner

Marius Paraschivoiu Supervisor

Approved by: _____

MASc Program Director

Department of Mechanical and Industrial Engineering

____/____/2016

Dean of Faculty

ABSTRACT

CFD Based Analysis and Parametric Study of a Novel Wind Turbine Design: the Dual Vertical Axis Wind Turbine

Gabriel Naccache

Small Vertical Axis Wind Turbines (VAWTs) are good candidates to extract energy from wind in urban areas because they are easy to install, service and do not generate much noise; however, the aerodynamic efficiency of small turbines is low. Here-in a new turbine, with high aerodynamic efficiency, is proposed. The novel design is based on the classical H-Darrieus VAWT. VAWTs produce the highest power when the blade chord is perpendicular to the incoming wind direction. The basic idea behind the proposed turbine is to extend that said region of maximum power by having the blades continue straight instead of following a circular path. This motion can be performed if the blades turn along two axes; hence it was named Dual Vertical Axis Wind Turbine (D-VAWT). The analysis of this new turbine is done through the use of Computational Fluid Dynamics (CFD) with 2D and 3D simulations. While 2D is used to validate the methodology, 3D is used to get an accurate estimate of the turbine performance. The analysis of a single blade is performed and the turbine shows that a power coefficient of 0.4 can be achieved. So far, reaching performance levels high enough to compete with the most efficient VAWTs. The D-VAWT is still far from full optimization, but the analysis presented here shows the hidden potential and serves as proof of concept. The study of the D-VAWT is concluded with a preliminary parametric study of the turbine sensitivity to different incoming wind angles, turbine axes spacing, number of blades, airfoil profile and blade mounting point.

Keywords: Wind Turbine, VAWT, Dual Axis, Innovative, Power Coefficient, CFD, Parametric Study.

ACKNOWLEDGMENTS

I would like to thank my thesis supervisor and mentor, Dr. Marius Paraschivoiu, for his immeasurable support, guidance, and insight. The completion of this thesis would not have been possible without his moral and educational support. I greatly appreciate his availability and approachability as they were key in overcoming many obstacles faced during this thesis. He served as an inspiration and allowed me to produce the best work possible. One could not wish for a better supervisor.

I thank Le Fonds Quebecois de la Recherche sur la Nature et les Technologies (FQRNT) for the funding of this research project. I would also like to thank the Concordia Institute for Water, Energy and Sustainable Systems (CIWESS) and the Natural Sciences and Engineering Research Council of Canada (NSERC) for partial funding of this project through the Collaborative Research and Training Experience (CREATE) program.

My thanks go to Martin Komeili and my colleagues for their advice, their suggestions, and contributing to an enjoyable working environment during my research. I am privileged to have worked with you.

Special thanks to Hany Goma for his moral support and guidance during and before the start of this thesis. I am very grateful to have met him as he helped me discover the joy of research and academia.

I am also sincerely grateful to my close friends, Patrick Larin, Nelson David Hernández Blanco and Abilash Krishnan, for their friendship and support.

Finally, I would like to thank my loving parents, Therese Khoury and Hugues Naccache, for their unconditional love and support at my most challenging times. I am forever grateful to them. I would like to dedicate my thesis to my family and my close friends.

TABLE OF CONTENTS

List of Figures	viii
List of Tables	xii
Nomenclature	xiii
CHAPTER 1: Introduction	1
1.1 Energy Production.....	1
1.2 Wind Energy	2
1.3 Wind Turbines.....	5
1.4 Motivation	9
1.5 Objectives.....	11
1.6 Literature Review	12
1.6.1 Methods of VAWT Analysis	12
1.6.2 Current Research.....	13
1.7 Thesis Outline	18
CHAPTER 2: Methodology Considerations.....	20
2.1 Governing Equations.....	20
2.2 Turbulence Modelling.....	21
2.2.1 Spalart-Allmaras	21
2.2.2 Shear-Stress Transport $k-\omega$	23
2.2.3 Transition Shear-Stress Transport.....	23
2.3 Wall Treatment.....	25
2.4 Original Turbine Geometry	26
2.5 Parameters for the D-VAWT	28
2.5.1 Swept Area.....	28
2.5.2 Coefficient of Power	28

2.5.3	Solidity	30
2.5.4	Axis Eccentricity Factor	30
2.6	Theoretical Power Coefficient in Upstream Translational Region	31
2.7	Analysis Milestones	32
CHAPTER 3: Methodology Validation in 2D		34
3.1	Numerical Setup	34
3.2	Initial Domain	36
3.3	Investigation of Domain size	37
3.4	Different Motion Methodology	38
3.4.1	Motion Type 1	38
3.4.2	Motion Type 2	40
3.4.1	Motion Type 3	40
3.4.2	Results and Discussion	43
3.5	Mesh Convergence Study using SST k- ω Model with $y^+ \sim 1$	44
3.5.1	Meshes	45
3.5.2	Results and Discussion	49
3.6	Turbulence Model Study	50
3.7	Airfoil Validation with Experimental Results	52
3.7.1	Domain and Mesh	52
3.7.2	Results and Discussion	53
3.8	Summary and Conclusions	56
CHAPTER 4: 3D Investigation		58
4.1	Domain	58
4.2	Mesh	59
4.3	Numerical Setup	63
4.4	Results and Discussion	63

4.5	Comparison of 2D and 3D Results.....	69
4.6	Discussion of D-VAWT Performance	70
CHAPTER 5: 2D Parametric Study.....		72
5.1	Introduction to Parametric Study	72
5.2	TSR Study of Original Turbine.....	73
5.3	Incident Wind Angle	76
5.4	Axis Eccentricity Factor (AEF).....	82
5.5	Multi-Blade Turbine Analysis.....	86
5.6	High Lift-to-Drag Airfoil	90
5.7	Blade Mounting Point	92
5.8	Summary and Discussion of Parametric Study	94
CHAPTER 6: Conclusion.....		95
6.1	Summary	95
6.2	Contributions.....	96
6.3	Future Work	96
6.3.1	Future Work Summary	97
References.....		98

LIST OF FIGURES

Figure 1.1: World Total Primary Energy Supply from 1971 to 2013 by fuel (Mtoe). ² Peat and Oil Shale are Aggregated with Coal. ³ Includes Geothermal, Solar, Wind, Heat, etc. [1]	2
Figure 1.2: Canada’s Primary Energy Production by Source in 2013. “Other Renewables” Includes Wind, Solar, Wood/Wood Waste, Biofuels and Municipal Waste [2]	2
Figure 1.3: Global Cumulative Installed Wind Capacity 2000-2015 [3].....	3
Figure 1.4: Cumulative and Annual Installed Capacity in Canada [2].....	3
Figure 1.5: Example of Large Scale Wind Turbines (a) Siemens G2 2.3MW [5], (b) Éole Rotor Darrieus 4.3MW [6].....	4
Figure 1.6: Examples of Small Scale Wind Turbines (a) Helix Wind 5kW Savonius [7], (b) Quiet Revolution 7.5kW [8], (c) WHI 70kW [9]	5
Figure 1.7: Global Installed Energy Capacity and Units [4]	5
Figure 1.8: Main Types of Wind Turbines [10, 11].....	6
Figure 1.9: Different Darrieus Wind Turbines [12].....	6
Figure 1.10: Power Coefficients for Different Rotor Designs [13, 14]	7
Figure 1.11: Top view of a typical H-Darrieus VAWT with Velocity Vectors and Forces, Where θ is the Azimuthal Angle, U_∞ is the Free Stream Velocity, V_{blade} is The Blade Velocity, $U_{relative}$ is The Relative Velocity Seen by the Blade, α is the Effective Angle of Attack, D is the Drag Force, And L is the Lift Force.....	10
Figure 1.12: Torque Variation Versus Azimuthal angle for 2D Simulation H-Darrieus Turbine (a) TSR = 2 and (b) TSR =3 [16]	10
Figure 1.13: Example of D-VAWT (a) Top View (b) 3D CAD Model	11
Figure 1.14: Summary of Methods for VAWT Analysis	13
Figure 1.15: Turbulence Modeling Behavior at High TSR ($\lambda=4.25$) (Left) and Low TSR ($\lambda=2.55$) (Right) [31]	16
Figure 2.1: Law of the Wall [55]	25
Figure 2.2: Top View of a D-VAWT Path	27
Figure 2.3: Steps for Coefficient of Power Calculation (a) Force Based, (b) Torque Based	29

Figure 2.4: Instantaneous Coefficient of Power Curve Based on the Combination of both the Force and Torque Based Methods	30
Figure 2.5: Milestones for the CFD Analysis of the D-VAWT	33
Figure 3.1: Initial Domain with Boundary Conditions	36
Figure 3.2: View of the Rotating Domain and Blade Refinement Region	36
Figure 3.3: Instantaneous C_P vs. Normalized Time of the 10th Cycle for Different Domain Sizes	38
Figure 3.4: Type 1 Motion Illustration	39
Figure 3.5: Mesh Used for Type 1 and 2 Motions	39
Figure 3.6: Rotating Domain Mesh for Type 1 and 2 Motions	40
Figure 3.7: Type 2 Motion Illustration	41
Figure 3.8: Type 3 Motion Illustration	41
Figure 3.9: Overview of Mesh Used for Type 3 Motion	42
Figure 3.10: Deforming Domain Mesh View for Type 3 Motion	42
Figure 3.11: Dynamic Domain Mesh View for Type 3 Motion	43
Figure 3.12: Instantaneous C_P versus Normalized Time of the 10th Cycle for Motion Types	44
Figure 3.13: Rotating Domain Mesh View for Mesh 1	46
Figure 3.14: Refinement Region Mesh Around Blade for Mesh 1	47
Figure 3.15: Boundary Layer Views for Mesh 1 at Leading Edge (Top), Mid-Chord (Middle), and Trailing Edge (Bottom).....	47
Figure 3.16: Rotating Domain Mesh View for Mesh 2	48
Figure 3.17: Refinement Region Mesh Around Blade for Mesh 2.....	48
Figure 3.18: Boundary Layer View for Mesh 3.....	48
Figure 3.19: Average Cycle C_P Convergence Plot for Mesh 1	49
Figure 3.20: Instantaneous C_P versus Normalized Time at 15th Cycle for Mesh and Time Convergence Study Cases.....	50
Figure 3.21: Instantaneous C_P Plots of the 15 th cycle for the Turbulence Model Study Using Mesh 1 at TSR=4.5	51
Figure 3.22: Overview of (a) Domain (b) Mesh, for the Experimental Case Simulation.....	53
Figure 3.23: Mesh Near Blade for (a) $y \sim 30$ (b) $y \sim 1$	53
Figure 3.24: Coefficient of Lift vs Angle of Attack	54

Figure 3.25: Coefficient of Drag vs Angle of Attack	54
Figure 3.26: Ratio of Coefficient of Lift to Coefficient of Drag vs Angle of Attack.....	55
Figure 3.27: Coefficient of Lift vs Coefficient of Drag.....	55
Figure 4.1: 3D Domain for D-VAWT with AR=5	58
Figure 4.2: Rotating Domain Mesh at Symmetry Plane for AR=5 and $y \sim 30$	60
Figure 4.3: Refinement Region Mesh at Symmetry Plane for AR=5 and $y \sim 30$	61
Figure 4.4: Boundary Layer Mesh View at Symmetry Plane for AR=5 and $y \sim 30$	61
Figure 4.5: Cross Section of Mesh Around the Blade AR=5 and $y \sim 30$	61
Figure 4.6: Refinement Region Mesh at Symmetry Plane for AR=5 and $y \sim 1$	62
Figure 4.7: Boundary Layer Mesh View at Symmetry Plane for AR=5 and $y \sim 1$	62
Figure 4.8: Cross Section of Mesh Around the Blade for AR=5 and $y \sim 1$	62
Figure 4.9: Boundary Conditions for 3D Domains.....	63
Figure 4.10: Average C_p per Cycle Convergence for 3D Simulations	64
Figure 4.11: Instantaneous C_p Plots of the Last Cycle for 3D Simulations.....	65
Figure 4.12: Normalized Velocity Deficit ($U_\infty - UU_\infty$) Plots on a Plane of Half a Chord Away in the Span-Wise Direction from the Symmetry Plane at $t/T=0.68$ for Cases (a) SA Strain/Vorticity ($y \sim 30$) with AR =5, (b) SA Strain/Vorticity ($y \sim 30$) with AR =15, (c) SST k- ω ($y \sim 1$) with AR =5, and (d) SST k- ω ($y \sim 1$) with AR =15	67
Figure 4.13: Static Pressure Contour on Half of the Blade Surface for SST k- ω ($y \sim 1$) Model at $t/T=0.33$ for (a) AR = 15 (b) AR = 5	68
Figure 4.14: Turbulent Viscosity Ratio (ν_t/ν) Plots on a Plane of Half a Chord Away in the Span- Wide Direction from the Symmetry Plane at $t/T=0.33$ for Cases (a) SA Strain/Vorticity ($y \sim 30$) with AR =5, (b) SA Strain/Vorticity ($y \sim 30$) with AR =15 and (c) SST k- ω ($y \sim 1$) with AR =5, and (d) SST k- ω ($y \sim 1$) with AR =15	68
Figure 4.15: Comparing Instantaneous C_p for 2D and 3D with AR =5 and 15 Using the SST k- ω Model ($y \sim 1$)	69
Figure 5.1: Instantaneous Blade Angle of Attack for Darrieus Type VAWT vs Azimuthal Angle for Different TSRs	73
Figure 5.2: Average Power Coefficient Convergence per Cycle for Different TSR values for AEF=4.....	74
Figure 5.3: Average C_p per Cycle vs TSR for AEF= 4 with Quadratic Curve Fitting	74

Figure 5.4: Instantaneous C_P for Different TSR Values at AEF =4	75
Figure 5.5: Incident Wind Angle Convention.....	76
Figure 5.6: Average C_P for Different TSRs with Different Incoming Incident Wind Angles with Quadratic Curve Fitting	77
Figure 5.7: Peak C_P for Each Incident Wind Angle.....	78
Figure 5.8: Instantaneous C_P for Different TSR Values for $\varphi = -20^\circ$	79
Figure 5.9: Instantaneous C_P for Different TSR Values for $\varphi = -40^\circ$	79
Figure 5.10: Instantaneous C_P for Different TSR Values for $\varphi = -60^\circ$	79
Figure 5.11: Instantaneous C_P for Different TSR Values for $\varphi = +20^\circ$	80
Figure 5.12: Instantaneous C_P for Different TSR Values for $\varphi = +40^\circ$	80
Figure 5.13: Instantaneous C_P for Different TSR Values for $\varphi = +60^\circ$	80
Figure 5.14: Percent Time Translating vs AEF	82
Figure 5.15: Average CP per Cycle vs TSR for AEF Study with Quadratic Curve Fitting	83
Figure 5.16: Instantaneous CP for Different TSRs with AEF = 8	85
Figure 5.17: Instantaneous CP for Different TSRs with AEF = 12	85
Figure 5.18: View of Deforming Domain at (a) $t/T = 0$ and (b) $t/T = 0.36$	86
Figure 5.19: Close View of Mesh Around Blades at $t/T = 0.36$	87
Figure 5.20: Average Power Coefficient Convergence per Cycle for Different TSR values for Two Bladed Turbine.....	87
Figure 5.21: Average C_P per Cycle vs TSR for a Single and Two Bladed Turbine	88
Figure 5.22: Instantaneous CP of Blade 1 of the Two Bladed Turbine	89
Figure 5.23: Total Instantaneous CP for Two Bladed Turbine.....	89
Figure 5.24: Comparison of Instantaneous C_P at Best TSR for the Single and Two Blade Turbines	90
Figure 5.25: S1223 and NACA 0018 Airfoil Profile.....	91
Figure 5.26: Average CP per Cycle vs TSR for Different Blade Airfoil Profiles	91
Figure 5.27: Instantaneous CP for Different TSRs for the S1223 Airfoil	92
Figure 5.28: Average C_P per Cycle vs TSR for Different Blade Mounting Points (MP).....	93
Figure 5.29: Instantaneous C_P for Different TSRs for the Blade Mounting Point at Half Chord	93

LIST OF TABLES

Table 1.1: Summary of the Most Important Differences between the H-Rotor Darrieus, Rotor Darrieus and HAWT [11]	8
Table 1.2: Comparative Analysis of the Literature Settings for 2D Unsteady Simulations of Darrieus Type VAWTs [32]	16
Table 2.1: D-VAWT Geometrical Characteristics.....	27
Table 2.2: Summary of Theoretical Results	32
Table 3.1: Results Summary for Domain Size Study	37
Table 3.2: Comparison of Results for Different Motion Types.....	43
Table 3.3: Details of Each Mesh Used for Mesh Study.....	46
Table 3.4: Mesh and Time Convergence Study Results	49
Table 3.5: Results for the Turbulence Model Study Using Mesh 1 at TSR =4.5	51
Table 3.6: Percent Error for Airfoil Case Study (Positive is Over Prediction and Negative is Under Prediction).....	56
Table 4.1: 3D Domain Characteristics.....	59
Table 4.2: 3D Meshes Details.....	60
Table 4.3: C_P Results Summary for 3D Simulations	64
Table 5.1: Summary of Peak C_P for the Incident Wind Angle Study.....	78
Table 5.2: Summary of Average C_P per Section at TSR = 5.5 for $\varphi =0^\circ$ and $+20^\circ$	81
Table 5.3: Summary of AEF Study for Peak Performance.....	83
Table 5.4: Summary of AEF Study for Peak and 90% of Peak Performances Using Curve Fitted Data.....	84

NOMENCLATURE

λ	Tip Speed Ratio (TSR)
ω	Angular Velocity [rad/s]
R	Turbine Radius [m]
U_∞	Free Stream Velocity [m/s]
C_p	Coefficient of Power
P	Total Extracted Power [W]
P_a	Available Power in Incoming Wind [W]
ρ	Fluid Density [kg/m ³]
A	Turbine Swept Area [m ²]
θ	Azimuthal Angle [deg]
L	Distance Between Axes of Rotation [m]
C	Chord [m]
D	Turbine Diameter [m]
h	Blade Height [m]
AR	Blade Aspect Ratio [m]
φ	Incoming Incident Wind Direction Angle [deg]
$T_{Rotating}$	Sum of the Torque Produced When the Blade is Rotating for a Single Cycle [N.m]

$F_{Translating}$	Sum of the Tangential Force Produced When the Blade is Translating for a Single Cycle [N]
V_{blade}	Blade Velocity [m/s]
$C_{P, Torque}$	Coefficient of Power for the Rotating Sections
$C_{P, Force}$	Coefficient of Power for the Translational Sections
σ	Solidity
N_b	Number of Blades
ε	Axis Eccentricity Factor (AEF)
A_{AF}	Airfoil Planform Area [m ²]
Re	Reynolds Number Based On Blade Velocity
C_L	Coefficient of Lift
C_D	Coefficient of Drag
Δt	Time Step Size [ms]
T	Period [s]
μ	Dynamic Viscosity [Kg/m.s]
ν_t	Turbulent Kinematic Viscosity [m ² /s]
ν	Kinematic Viscosity [m ² /s]
α	Angle of Attack [deg]

CHAPTER 1: INTRODUCTION

1.1 Energy Production

Global energy consumption has been exponentially increasing over the last few decades, largely due to the increase in energy demand from developing and developed countries related to the growth in global population and the increase in personal demand. A country's economic, social and technological growth are closely tied to the availability of energy. This is especially true for developing countries. Energy has undoubtedly become a basic human need in this modern day era and will continue to be for the distant future. The main consumers of energy are the residential, commercial/institutional, industrial, and transportation sectors.

Figure 1.1 shows the growth of energy supply from 1971 to 2013 as well as the breakdown of energy production by source type as reported by the International Energy Agency (IEA) [1]. From the same figure, one can see that from 1971 until 2013, the bigger portion of the world's energy is still produced from fossil fuels such as coal, petroleum/oil and natural gas. Though energy sources such as nuclear, hydro and renewables have been growing, they still represent a fraction of the total supply. Figure 1.2 shows the breakdown of energy in Canada, published by the Natural Resources Canada (NRCan) [2]. Similarly to before, nearly 90% of the total energy produced is from fossil fuels. As one might know, these sources of energy are finite and more importantly, they produce large amounts of greenhouse gases (GHGs), which in turn damage our environment and increase the effects of climate change.

The need for a sustainable and efficient source of renewable energy is highly in demand and satisfying this need has been an objective for decades. There are a number of available renewable energy sources to tap into, such as solar, wind, geothermal, hydro, biomass and tidal. There has been increased interest in these cleaner and renewable sources of energy as they reduce the reliance on those other finite sources of energy as well greatly reduce the effects of GHGs to help fight climate change.

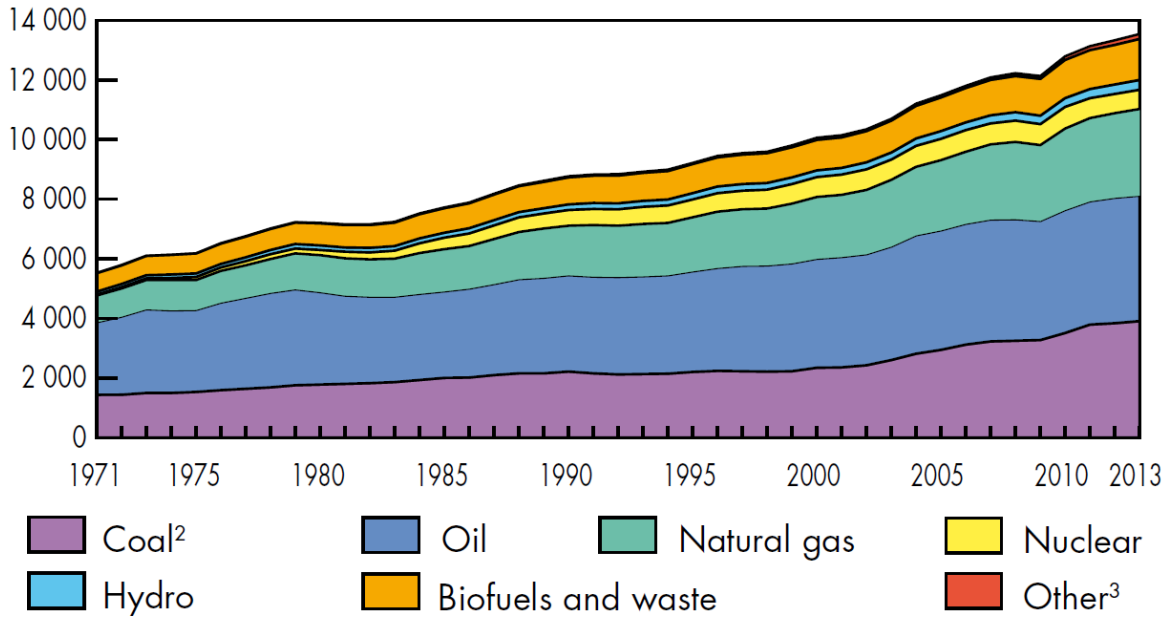


Figure 1.1: World Total Primary Energy Supply from 1971 to 2013 by fuel (Mtoe). ²Peat and Oil Shale are Aggregated with Coal. ³Includes Geothermal, Solar, Wind, Heat, etc. [1]

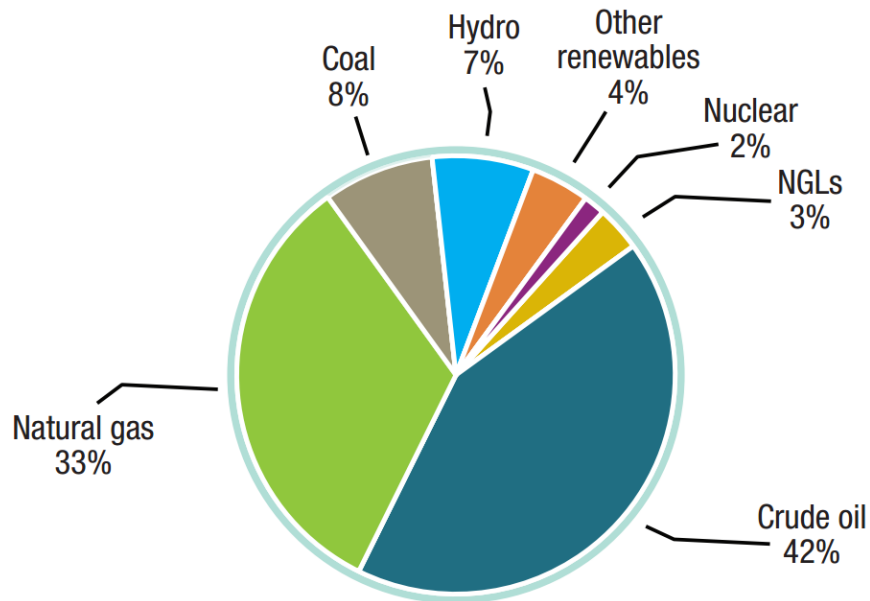


Figure 1.2: Canada's Primary Energy Production by Source in 2013. "Other Renewables" Includes Wind, Solar, Wood/Wood Waste, Biofuels and Municipal Waste [2]

1.2 Wind Energy

Wind energy has shown great potential as a sustainable solution and its production has grown tremendously in recent years. Figure 1.3 shows the growth of wind energy capacity on a global scale as published by the Global Wind Energy Council (GWEC) [3], while Figure 1.4 shows the

wind energy capacity in Canada. Wind energy has been used as both a complementary source of energy as well as a substitute for other sources of energy. The numerous types of wind turbines in sizes and applications make it a very flexible source of energy. The most common way of extracting energy from the wind is through wind turbines. The only stage in which wind turbines pollute the environment is before the installation stage. Once the turbines are installed, they produce negligible amounts of GHGs for the rest of their life cycles. Since their first use, wind turbines have gone through incredible technological advancements and even until now, there is still plenty of room for improvements and development. Wind turbines have gotten more efficient and much bigger since they were first invented thanks to advancements in aerodynamic, structural and material design.

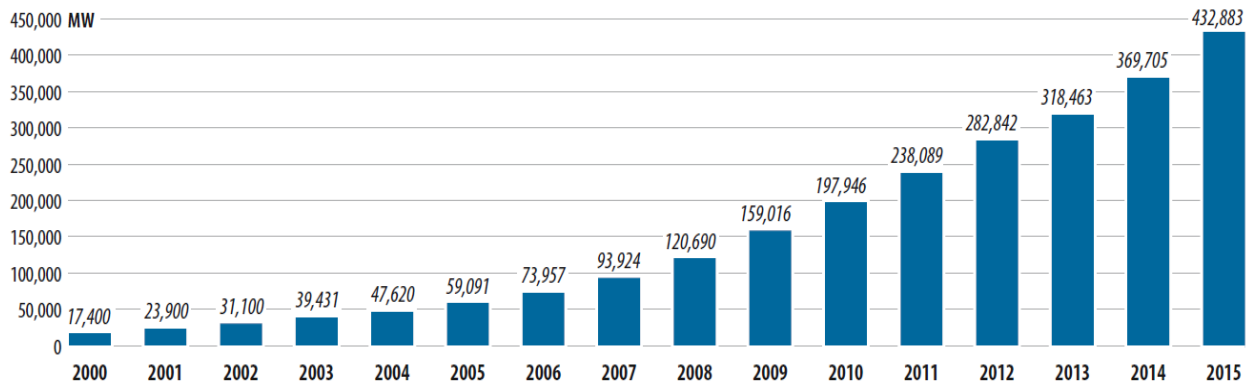


Figure 1.3: Global Cumulative Installed Wind Capacity 2000-2015 [3]

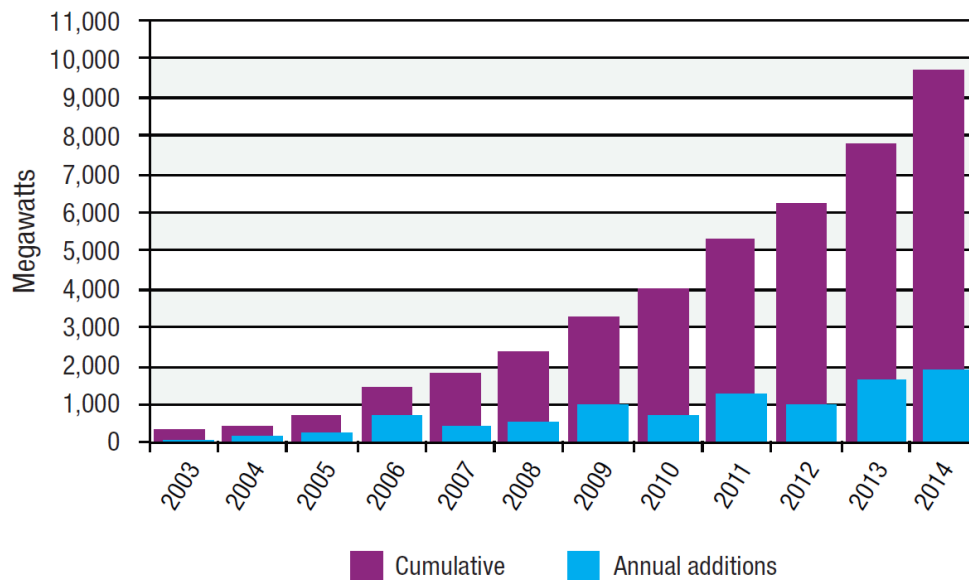


Figure 1.4: Cumulative and Annual Installed Capacity in Canada [2]

Wind turbines of large scale are used for onshore and offshore farms while the small scale turbines are used for urban applications. Large scale turbines are the ones that can typically produce 100kW and above, shown in Figure 1.5, while small scale turbines, shown in Figure 1.6 produce below that threshold. It should be noted that whether a turbine is considered large or small for accreditation purposes, the turbine swept area is used instead as criterion. So far, the large wind turbines have been favored as they were typically more efficient and produced significantly higher amounts of power. However, recent advancements in small scale wind turbines have made them more attractive, especially since distributed energy production is quite an attractive concept, as it is a much cheaper solution because power can be produced locally or near where it would be consumed. Therefore, typical problems faced with large scale turbines such as transportation, transmission cables, and maintenance costs can be avoided. The growth of small wind turbines in terms capacity and number of units can be seen in Figure 1.7, as published by the World Wind Energy Association (WWEA) [4].



(a)



(b)

Figure 1.5: Example of Large Scale Wind Turbines (a) Siemens G2 2.3MW [5], (b) Éole Rotor Darrieus 4.3MW [6]

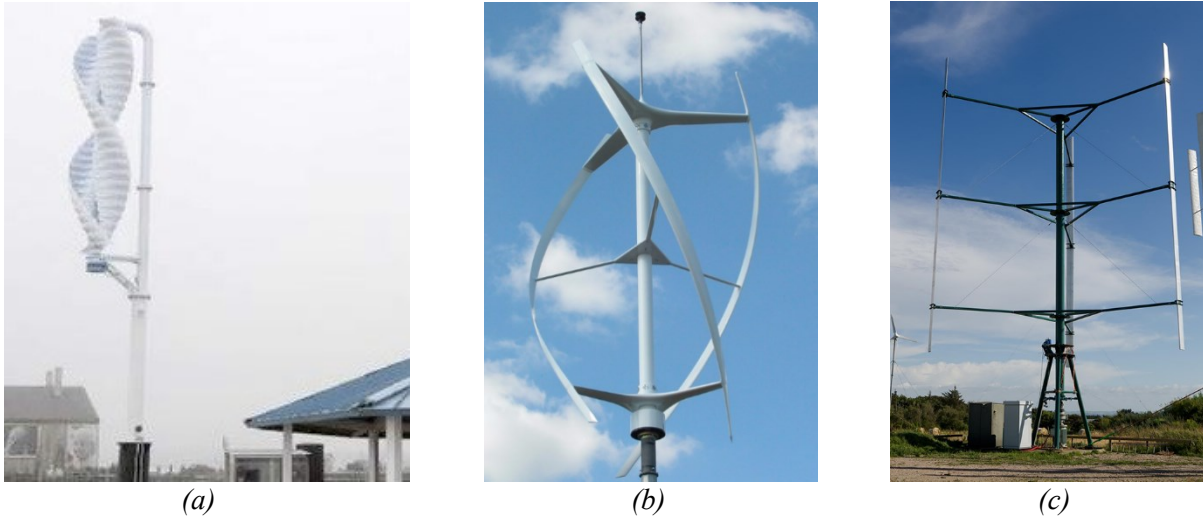


Figure 1.6: Examples of Small Scale Wind Turbines (a) Helix Wind 5kW Savonius [7], (b) Quiet Revolution 7.5kW [8], (c) WHI 70kW [9]

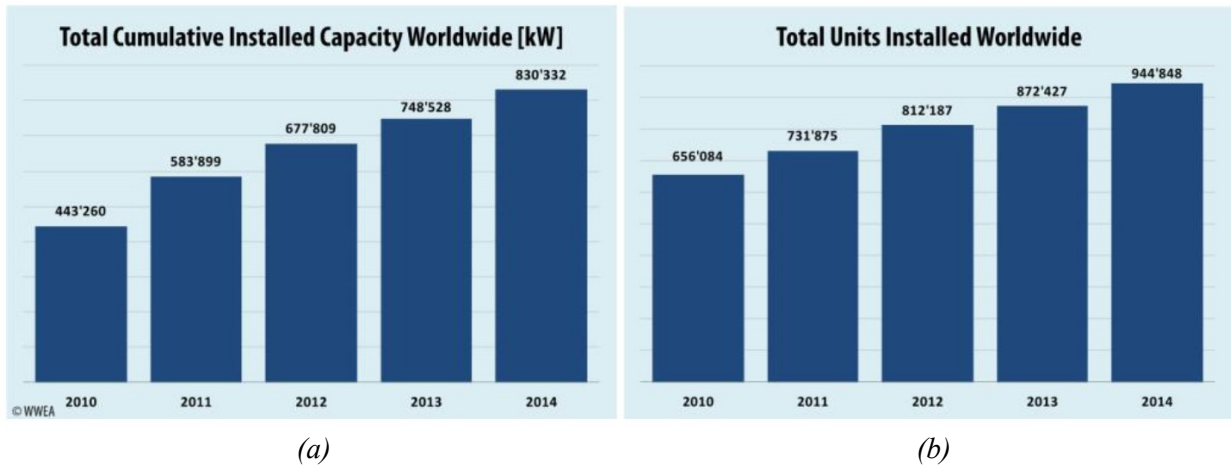


Figure 1.7: Global Installed Energy Capacity and Units [4]

1.3 Wind Turbines

Wind energy can be harnessed by a variety of turbines, which are classified in terms of their axis of rotation. The main types are shown in Figure 1.8. This includes the Horizontal Axis Wind Turbines (HAWT), which have their axes of rotation parallel to the incoming wind, and Vertical Axis Wind Turbines (VAWT), which have their axes of rotation perpendicular to the incoming wind. Typically, HAWTs are used more for large scale energy production, while VAWTs are used for small and large scale applications. The two most common types of VAWTs are the Savonius turbine, which is a drag based turbines, and the Darrieus wind turbine, which is a lift based turbines. There are also a number of different types of Darrieus VAWTs, the most common being the rotor Darrieus, H-rotor Darrieus (H-Darrieus), and helical Darrieus, shown in Figure 1.9. All

the Darrieus type turbines have an airfoil profile for their blade cross-section, but differ in their blade shape. An example of a HAWT, rotor Darrieus VAWT, Savonius VAWT, Helicoidale VAWT and H-rotor VAWT can be seen in Figure 1.5 (a) and (b) and Figure 1.6 (a), (b) and (c), respectively.

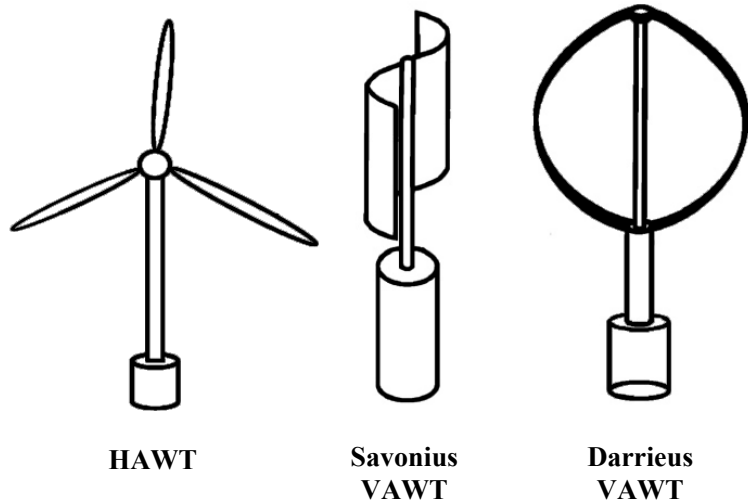


Figure 1.8: Main Types of Wind Turbines [10, 11]

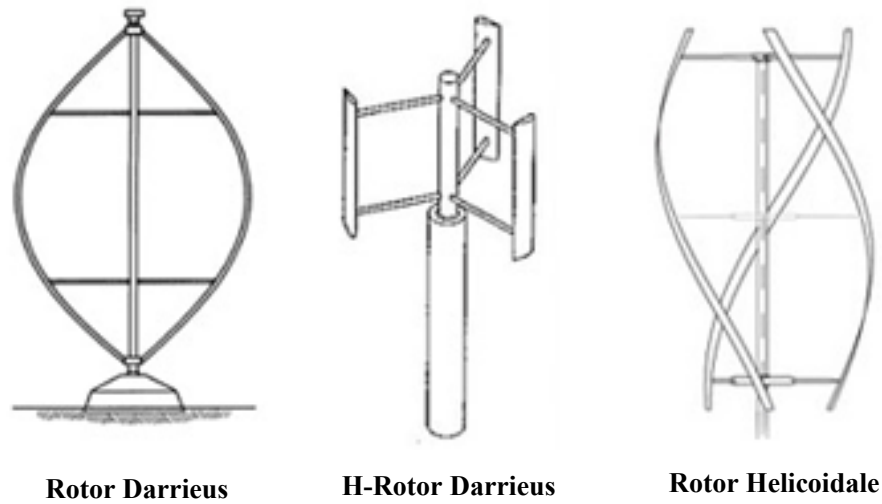


Figure 1.9: Different Darrieus Wind Turbines [12]

The following two dimensionless parameters are commonly used to describe the performance and operating condition of a VAWT. The first is the Tip Speed Ratio (TSR), which is the ratio of the blade speed at the tip to the incoming wind speed.

$$\lambda = TSR = \frac{\omega R}{U_\infty} \quad (1.1)$$

Where ω is the angular velocity of the turbine, R is the radius of the turbine, and U_∞ is the free stream velocity. The second is the Coefficient of Power (C_p) which is the ratio of extracted power to the available power (available kinetic energy per unit time) in the incoming wind. The power coefficient is a measure of the aerodynamic efficiency of turbines.

$$C_p = \text{Power Coefficient} = \frac{P}{\frac{1}{2}\rho U_\infty^3 A} \quad (1.2)$$

Where P is the extracted power from the turbine, ρ is the fluid density, and A is the turbine swept area.

Each of the HAWTs and VAWTs have a number of advantages and disadvantages. Figure 1.10 shows the typical power curves for the most common types of turbines, where it can be seen that HAWTs are typically more aerodynamically efficient and operate at much higher TSR values than VAWTs. A comparison between HAWTs and VAWTs has been investigated by Eriksson et al. [11]. A summary of his study between the H-Rotor Darrieus, Rotor Darrieus and HAWTs can be seen in Table 1.1.

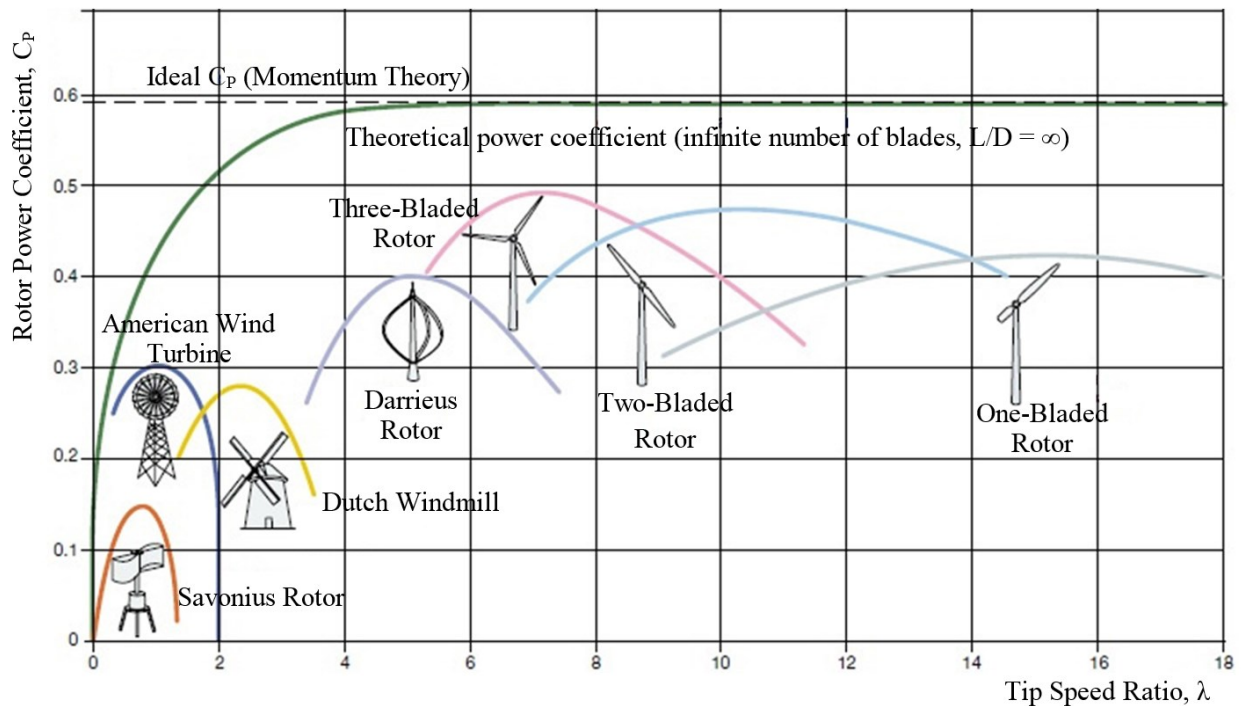


Figure 1.10: Power Coefficients for Different Rotor Designs [13, 14]

Table 1.1: Summary of the Most Important Differences between the H-Rotor Darrieus, Rotor Darrieus and HAWT [11]

	H-rotor	Darrieus	HAWT
Blade profile	Simple	Complicated	Complicated
Yaw mechanism needed	No	No	Yes
Pitch mechanism possible	Yes	No	Yes
Tower	Yes	No	Yes
Guy wires	Optional	Yes	No
Noise	Low	Moderate	High
Blade area	Moderate	Large	Small
Generator position	On ground	On ground	On top of tower
Blade load	Moderate	Low	High
Self starting	No	No	Yes
Tower interference	Small	Small	Large
Foundation	Moderate	Simple	Extensive
Overall structure	Simple	Simple	Complicated

HAWTs are among the most efficient turbines and can be more easily scaled up in size for higher amounts of energy production; however, they are highly dependent on the wind direction, needing to face the wind for optimal performance. An added yawing and pitching mechanism can be added to increase their flexibility at the cost of higher complexity and financial cost. The manufacturing of their blades is more expensive than VAWTs' since the blade cross sectional profile varies along the span, while a number of VAWTs have the same blade profile along the span. Because HAWTs' gearboxes, generators and other mechanical components are at the top of the tower, their maintenance is more difficult, expensive and dangerous. They are also known to be quite noisy since they operate at high tip speed ratios and since the blades are placed at a large height, the sound produced can propagate more easily. Also, another disadvantage from the enormous height of the tower is the flicker of the blades' shadow, which have been known to cause problems for people staying in affected areas. Thus, these turbines have to be placed in remote areas, where additional costs are incurred related to transportation and road building costs.

VAWTs address a number of these disadvantages. They produce much less noise since their operating speeds are lower than HAWTs. Their maintenance is simpler since all components (the gearbox, generator, etc.) are placed on the ground. They typically do not require a yaw control mechanism as their performance is independent of the incoming wind direction. Also, because they have smaller wakes than HAWTs, they can be packed quite closely together, resulting in higher turbine density per unit area. However, VAWTs are generally less aerodynamically

efficient than HAWTs. They are structurally more challenging to design since the loads on the blade continuously change throughout the turbine rotation. The constant change in the blade incident angle puts them more at risk of failure due of fatigue loads. Also, most VAWTs lack self-starting capabilities, except for the Savonius turbine, but it has lower aerodynamic efficiency than other VAWTs.

1.4 Motivation

Small VAWTs are good candidates for urban areas because they are easy to install, service and do not generate much noise. Nevertheless, the wind speed in urban areas is low, leading to low power generation for a given area. To address this weakness a new type of wind turbine is investigated in an attempt to improve the aerodynamic efficiency of small wind turbines. VAWTs produce the highest power when the blade is near perpendicular to the incoming wind direction. This result is confirmed by Paraschivoiu [15]. Figure 1.11 shows the top view of an H-Darrieus turbine as well as the convention for the azimuthal angle, θ , which defines the position of the blade. The maximum power is produced when the blade is at $\theta \sim 90^\circ$, which is confirmed by looking at Figure 1.12, which is the torque graph vs azimuthal angle for an H-Darrieus turbine obtained from Computational Fluid Dynamics (CFD) simulations performed by Zadeh et al. [16]. At this position, the blade sees an effective flow angle and flow velocity that is optimal. Note that the flow reaching the blade is the vector sum of the incoming wind and blade velocities. An example of the velocity vectors seen by the blade is shown Figure 1.11 for a Darrieus turbine with multiple blades at three positions.

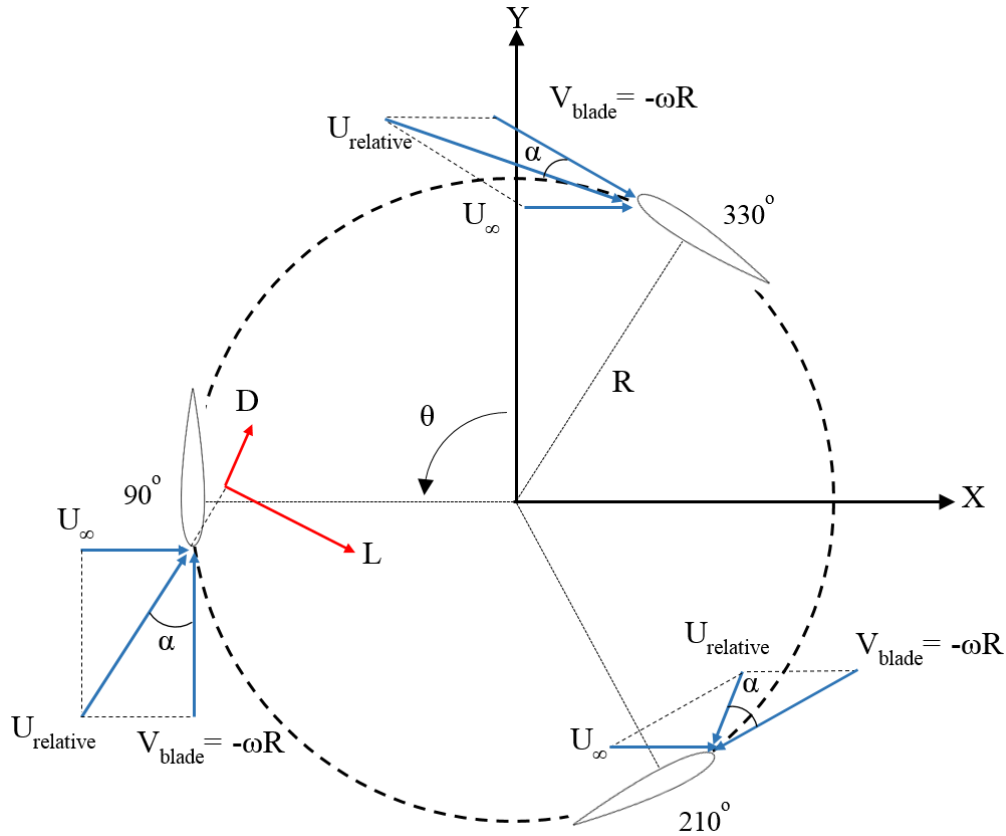


Figure 1.11: Top view of a typical H-Darrieus VAWT with Velocity Vectors and Forces, Where θ is the Azimuthal Angle, U_∞ is the Free Stream Velocity, V_{blade} is The Blade Velocity, $U_{relative}$ is The Relative Velocity Seen by the Blade, α is the Effective Angle of Attack, D is the Drag Force, And L is the Lift Force

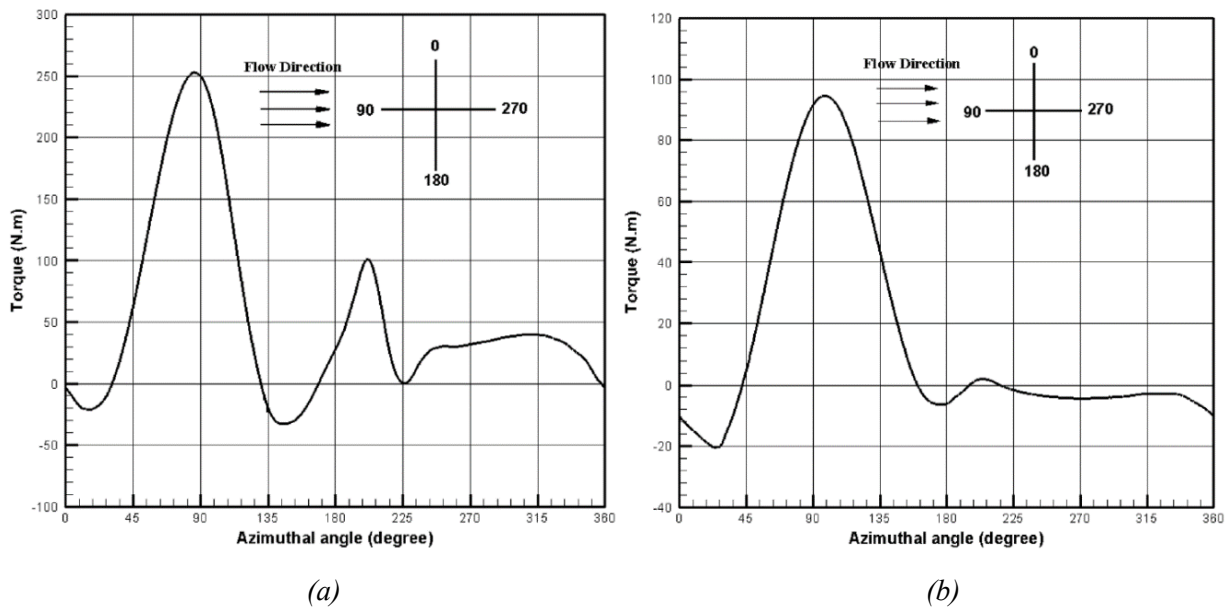


Figure 1.12: Torque Variation Versus Azimuthal angle for 2D Simulation H-Darrieus Turbine (a) $TSR = 2$ and (b) $TSR = 3$ [16]

The new turbine concept, with a similar blade shape as the H-Darrieus, would utilize the location of maximum power and have it extended by letting the blades continue straight in an attempt to increase the overall aerodynamic efficiency of the turbine. This motion can be achieved if the blades turn around two axes, hence it was named Dual Vertical Axis Wind Turbine (D-VAWT). Figure 1.13 shows a top view of the turbine and a 3D CAD model to give a better idea of the geometry and mechanism of the D-VAWT. It should be noted that the mechanism will not be present in any simulations. It is shown here for illustration purposes only.

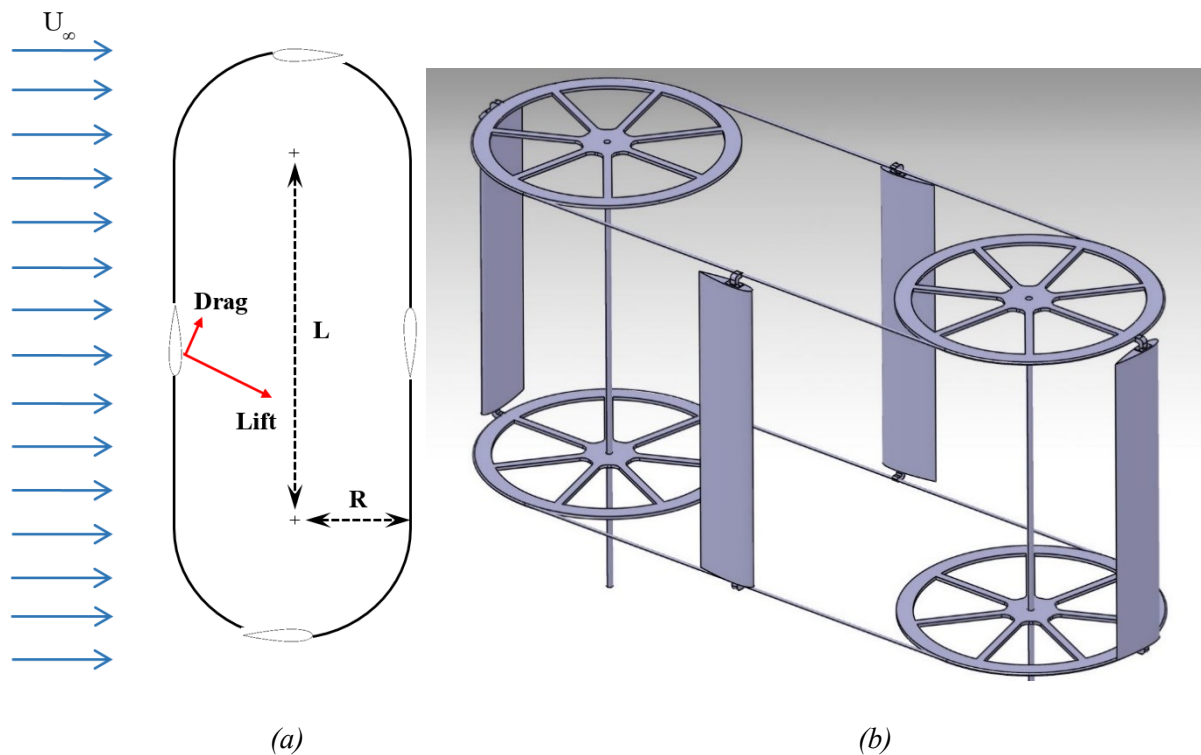


Figure 1.13: Example of D-VAWT (a) Top View (b) 3D CAD Model

1.5 Objectives

- Investigate the feasibility of the D-VAWT design for a single blade analysis using ANSYS Fluent 14.5 [17].
- Develop methodology to specify the motion of a D-VAWT blade as conventional methods for VAWT analysis would not directly apply for the current analysis.
- Perform a domain size, mesh convergence, turbulence model and y^+ study in 2D to determine the most appropriate setup for this analysis as well as find the cheapest mesh possible to be used for the 3D analysis.

- Based on the 2D methodology investigation, 3D simulations are to be performed to get a more accurate prediction of the turbine performance as 2D analysis has a tendency to overestimate power coefficient values as 3D losses are not accounted for.
- Perform a preliminary parametric study of the D-VAWT in 2D as it is possible to use the predicted behavior and trends for future designs of the D-VAWT. Investigation of the TSR behavior of the original turbine as well as the turbine sensitivity to different incoming wind angles, turbine axes spacing, number of blades, airfoil profile and blade mounting point are to be performed.

1.6 Literature Review

In this section, the possible methods of analyzing a VAWT will be outlined followed by a detailed review of current research with a focus on CFD modeling as it will be the tool of analysis in this thesis.

1.6.1 Methods of VAWT Analysis

There are various methods to study the performance of a VAWT. The main two categories are to use either experimental or numerical methods. The methods are summarized in Figure 1.14. Experimental analysis is done in wind tunnels, while numerical analysis is done through modeling of fluid phenomenon. Numerical models can be broken down to Computational Aerodynamics and Computational Fluid Dynamics (CFD). Aerodynamic models are significantly faster than CFD ones, but lack accuracy in predicting VAWT performance, especially when the turbine operates at low TSRs. Aerodynamic models were previously the most common modelling method as the resources needed to perform CFD simulation were too expensive; however with current advancements in computational power, CFD simulations have become much more attractive. For CFD simulations, the Navier-Stokes equations are discretized and solved, providing much more accurate results, but the drawback is higher computation cost and time. Even in CFD, there are various methods of modeling the flow; the most common for engineering applications is the Reynolds Averaged Navier-Stokes (RANS) models with turbulence modeling as it is able to predict VAWTs' performance with satisfactory accuracy. This will be the analysis method of choice for this thesis as it provides enough accuracy with reasonable computational costs. The other more accurate CFD models are the Eddy Simulations, where turbulence is now resolved and only eddies below the grid size are modeled. Though Eddy Simulations are more accurate than

RANS models, they require significantly higher computational cost. The Detached Eddy Simulation (DES) is a hybrid model of the Large Eddy Simulation (LES) and the RANS models. Finally, the most accurate and computationally expensive is the Direct Numerical Simulation (DNS), where the Navier-Stokes equations are completely resolved without any modeling which is the reason it requires tremendous computational cost as the mesh and time step needed are extremely fine. Xin et al. [18] provide more details on most of the methods presented here with relevant research done on Darrieus VAWTs. It should be noted that not all RANS models that exist have been presented here, but only the commonly used ones for VAWT analysis.

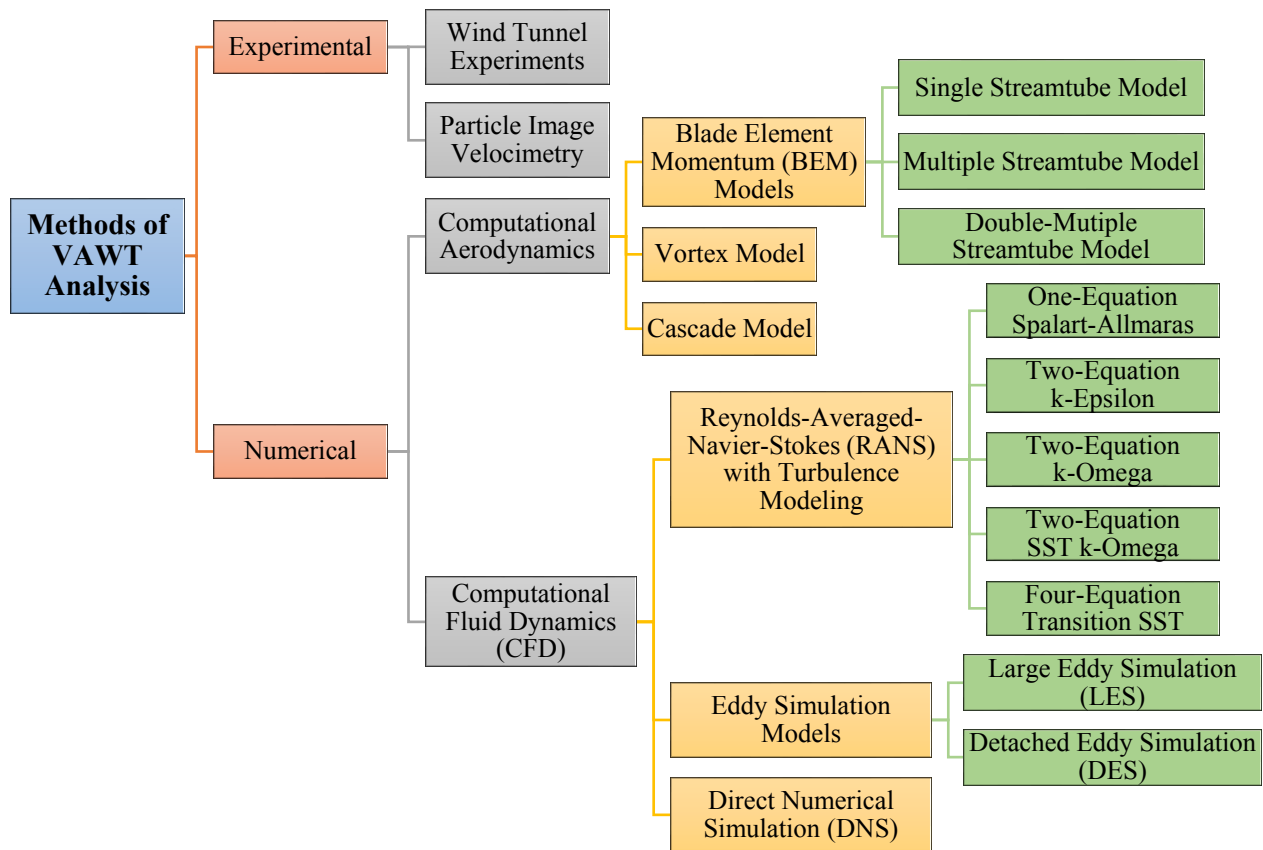


Figure 1.14: Summary of Methods for VAWT Analysis

1.6.2 Current Research

This section focuses on presenting recent research mainly done on VAWTs using CFD, which will constitute the basis of the methodology used during this thesis project. Though more focus will be on the H-Rotor Darrieus (H-Darrieus), as the turbine studied in this thesis resembles it the most

from a geometrical point of view. Interesting and relevant work on new innovative concept turbines will also be presented.

1.6.2.1 New Turbine Concepts

Using a similar idea of extending the maximum power region of a VAWT, Ponta et al. [19, 20] analyzed a Variable Geometry Oval-Trajectory (VGOT) Darrieus wind turbine using the double-multiple streamtube model, where they showed a very small improvement in aerodynamic efficiency over a classical H-Darrieus VAWT. They also showed that the turbine performance was independent of the number of blades, but highly sensitive to the incoming wind direction.

A new concept turbine was investigated by Kinsey et al. [21–23], where it consists of a pair of oscillating hydrofoils moving in a sinusoidal path. Kinsey et al. presented a computational methodology in [21] that agreed very well with their experimental data shown in [23]. They used ANSYS Fluent [17] to solve both 2D and 3D simulations of the unsteady Reynolds-Averaged-Navier-Stokes (URANS) equations. After studying different turbulence models to compute the turbine performance, they showed that the one-equation Spalart-Allmaras (SA) model performed very similarly to the two-equation Shear-Stress Transport (SST) $k-\omega$ model. To simulate the oscillating motion, non-conformal sliding meshes were used inside of a dynamically moving mesh. Sliding meshes are used for the simulation of the pitching motion, while the dynamic mesh is used for the heaving motion. In [22], they showed it is possible to limit losses appearing in 3D simulations, such as tip vortices, from their 2D prediction to about 10% with the use of endplates and a blade aspect ratio larger than 10. Gauthier et al. [24] investigated the blockage effect on the same oscillating-foils hydrokinetic turbine (OFHT) using the finite volume code CD-Adapco STAR CCM + with the overset mesh technique. They showed that the increase in blockage effect and extracted power are linearly related for up to 40% blockage as well as providing a correlation factor to account for that said blockage effect.

1.6.2.2 CFD vs. Aerodynamic Models

Delafin et al. in [25] compared the performance of a rotor Darrieus turbine using 3D CFD simulations of the SST $k-\omega$ model with other aerodynamic models, such as the double-multiple streamtube and vortex models. They showed that the 3D simulations accurately predicted the turbine behavior, while the aerodynamic models over predicted the power for all TSR values.

1.6.2.3 Performance Improvement

Mohamed et al. [26] investigated 25 different airfoil profiles, using the SST $k-\omega$ model in 2D, for an H-Darrieus Configuration. The best airfoil boosted the turbine performance by 10% when compared to the NACA 0018, which is a commonly used airfoil profile and is often used as a baseline for comparison. Yamazaki et al. [27] showed a performance improvement in VAWTs through the shape optimization of airfoil profiles by maximizing certain characteristics of the airfoil. The shape optimization was performed using a Kriging response surface approach, then 2D simulations were performed on the optimized shapes to quantify the improvement from the profile optimization. Xiao et al. [28], using the realizable $k-\epsilon$ model in 2D, studied the impact of fixed and oscillating flaps and showed a performance improvement of 28%.

Lim et al. [29] and Chong et al. [30] performed experimental tests and 2D simulations, using the SST $k-\omega$ model, to optimize an H-Darrieus VAWT using an omni-direction-guide-vane (ODGV). They showed it improved the self-starting capability of the turbine by 182% and its performance by 58% from the original configuration.

1.6.2.4 Study of H-Darrieus VAWTs

Gosselin et al. [31] studied the effects of various parameters for a 3 bladed H-Darrieus turbine. They showed that for a turbine operating at high TSR values, the choice of turbulence model had little effect on the turbine behavior predictions, while for low TSR values, significant differences in behavior were found for different turbulence models. The result for the C_P can be seen in Figure 1.15 for a single blade analysis. They also showed that the SA Strain/Vorticity based model produced 10 times less turbulent viscosity than the SST $k-\omega$ and Transition SST models. Using the SST $k-\omega$ with $y^+ \sim 1$, they compared the turbine performance in 2D and 3D with blade aspect ratios of 7 and 15. The power obtained in 3D for an aspect ratio of 7 and 15 are 41.8% and 69% of the 2D power, respectively. This shows how much 2D simulations overestimate the turbine performance and that increasing the aspect ratio increases the turbine performance as the aerodynamic losses such as tip vortices affect a smaller portion of the blade.

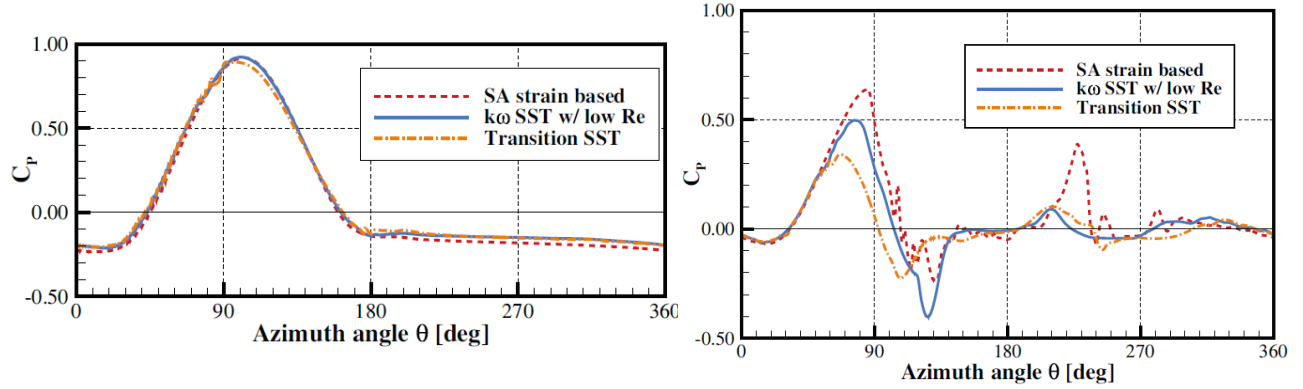


Figure 1.15: Turbulence Modeling Behavior at High TSR ($\lambda=4.25$) (Left) and Low TSR ($\lambda=2.55$) (Right) [31]

Balduzzi et al. [32] compiled a list of commonly used methodologies, including the selection of the turbulence model, domain size, and cycle to cycle convergence criterion to simulate Darrieus VAWTs in 2D. The summary of their findings is shown in Table 1.2. After performing their own investigation, they recommend the SST $k-\omega$ model, $y^+ \sim 1$, and most importantly to have a convergence criterion for the torque variation from to cycle to cycle of less than 0.1%, instead of the commonly used value of 1%. They found that a variation of 1% can continue for up to 10 cycles, leading to a large over estimation from the actual torque value.

Table 1.2: Comparative Analysis of the Literature Settings for 2D Unsteady Simulations of Darrieus Type VAWTs [32]

Simulation settings								
Turbulence Model		Algorithm		Azimuthal increment per timestep		Revolutions to convergence		
Spalart-Allmaras	[33]	SIMPLE	[38, 40, 42, 43]	$\Delta\theta \leq 0.5^\circ$	[37, 45]	rev ≤ 5	[38]	
	$k-\epsilon$							[34]
k- ω	Standard	Discretization scheme	1st order	$1^\circ < \Delta\theta < 2^\circ$	[43]	10 < rev ≤ 15	[33, 39, 42, 43]	
	Realizable							[35-38]
	RNG							[39, 40]
DES & LES	Standard	2nd order	[34, 37, 39, 42, 43]	$\Delta\theta = 2^\circ$	[25,29]	15 < rev	-	
	SST							[42, 43]
	SST-SAS							[44]
[45]								
Domain dimensions								
Inlet		Outlet		Width		Rotating region		
$L_1 \leq 5D$	[38, 40, 44]	$L_2 \leq 10D$	[38, 40, 44]	$W \leq 5D$	[36, 42, 43, 45]	$D_{RR} \leq 1.2D$	[34]	
$5D < L_1 \leq 10D$	[36, 43, 45]	$10D < L_2 \leq 20D$	[36, 45]	$5D < W \leq 10D$	[38, 40, 41, 44]	$1.2D < D_{RR} \leq 1.5D$	[40, 44]	
$10D < L_1$	[35, 37]	$20D < L_2$	[35, 37]	$10D < W$	[35, 37]	$1.5D < D_{RR}$	[35-37]	
Mesh								
y^+		Number of nodes on airfoil	Mesh size		Mesh type			
-1	[34, 41, 42, 45]	$N_N < 200$	$N_E \leq 2.5 \times 10^5$	[34, 38, 40-43]	Structured	[42, 45]		
$1 < y^+ \leq 10$	[36, 39, 44]	$200 < N_N < 2000$	$2.5 \times 10^5 < N_E \leq 1.0 \times 10^6$	[35, 44]	Unstructured	[35-38, 40]		
$30 < y^+$	[38]	$2000 < N_N$	$1.0 \times 10^6 < N_E$	[36, 45]	Unstructured with prismatic BL	[33, 43, 44]		

McNaughton et al. [46] compared the standard form of the SST $k-\omega$ with the SST $k-\omega$ with a correction for low-Reynolds number effects. They tested the models, in 2D with a $y^+ < 1$, for a

turbine operating at Reynolds number of 150,000. They showed an improvement in performance prediction with the low Reynolds correction model. Lanzafame et al. [47] compared, in 2D with a $y^+ < 1$, the two-equation SST $k-\omega$ with the four-equation Transition SST model. The Transition SST showed much better agreement with experimental results than the SST $k-\omega$; however, the Transition SST model is more computationally expensive and required a series of tests to calibrate the local correlation parameters with the experimental values in order to get accurate results.

Though 3D simulations are well known to provide more realistic performance as it is possible to capture secondary flows, wing tip vortices and aerodynamic losses from structural components such as the supporting arms and central shaft, the computational power and time needed are significantly higher than that of 2D's. For that reason, few simulations in literature are done in 3D. Siddiqui et al. [48] compared a 2D Darrieus turbine performance's predictions, using the realizable $k-\epsilon$ model, with 3D by simulating the support arm and central shaft. They found that 2D can overestimate the actual turbine performance by up to 32%. Castelli et al. [35, 49] first performed full 3D flow simulations, using the Realizable $k-\epsilon$ model, to find the loads on the blades, followed by a structural analysis using a Finite Element Method (FEM) code to find the stresses and deformation on the blades. Howell et al. [39] performed 2D and 3D simulations at low Reynolds number and found that 2D largely overestimated the extracted power, while 3D showed reasonable agreement with their experimental results. Rossetti and Pavesi [44] investigated the self-starting capabilities of H-Darrieus VAWTs using BEM, 2D and 3D methods at $TSR = 1$. They found that effects only captured in the 3D simulations, such as secondary flow and tip vortices, had a positive effect on start-up.

Ferreira et al. [45] compared the simulation results in 2D, for turbine cases where dynamic stall occurred, with experimental results from Particle Image Velocimetry (PIV). They found the model that agreed the most with their experimental results was the DES model, followed by the LES model, and finally the two URANS models, the SA and the $k-\epsilon$ model. These results were expected as the Eddy models are known to be more accurate but their drawbacks are the higher computational costs needed.

1.6.2.5 Miscellaneous Studies

Salim et al. [50] investigated the y^+ strategy for turbulent flow for a few simple cases. They suggested that resolving the log-law layer was sufficiently accurate ($30 < y^+ < 60$) without the

need to fully resolve the viscous sublayer ($y^+ < 5$) and to avoid resolving the buffer region ($5 < y^+ < 30$) as neither wall functions nor near-wall modelling accounted for it accurately.

Almohammadi et al. [51] investigated three mesh independency techniques: the General Richardson Extrapolation (GRE), Grid Convergence Index (GCI) and the fitting method. The study was performed in 2D for an H-Darrieus VAWT using the Re-Normalization Group (RNG) k- ϵ and Transition SST models.

Lee et al. [52] performed experiments on airfoils undergoing pure heaving, pitching, and combined motions at Reynolds number of 36,000 to better understand the behavior of unsteady boundary layers on airfoils. With accurate surface pressure measurements, Smoke-wire flow visualization and typical data of lift, drag and moment, CFD validation can be performed with a high level of accuracy because of the broad spectrum of data available for comparison. The airfoil performance was captured during stall and hysteresis as well, providing a complete range for comparison purposes.

1.7 Thesis Outline

This section presents the thesis structure and a brief description of the key points of each chapter.

Chapter 2: The equations for the Navier-Stokes and turbulence models used are presented. The D-VAWT geometrical characteristics and some newly defined parameters are introduced, which are needed for the current analysis. The chapter concludes with a brief theoretical analysis which helps to highlight the potential of the D-VAWT.

Chapter 3: The development and validation of the methodology used for the D-VAWT analysis is presented. The domain size, blade motion prescription, mesh convergence, and turbulence model study with different y^+ strategies are investigated. The chapter concludes with a case study, using the developed methodology, of a static airfoil in 2D and compared with experimental results

Chapter 4: 3D simulations based on the methodology developed in 2D for a single blade with aspect ratios of 5 and 15 are presented. Using two turbulence models with different y^+ strategies, the acquisition of an upper and lower bound value for the C_P estimation for a single blade is presented. Lastly, a brief discussion on the results and performance of the D-VAWT.

Chapter 5: A parametric study in 2D is performed to better understand the behavior of the D-VAWT. The simulations of different TSRs for the original single blade turbine will be first presented. The turbine sensitivity to the incoming wind direction is studied by investigating a range of incoming inlet angles. Next is the investigation of different ratio values of the distance between the two axes to the radius of the turbine, followed by simulating a turbine with two blades, a turbine with a cambered airfoil and finally simulating a different blade mounting point.

CHAPTER 2: METHODOLOGY CONSIDERATIONS

In this chapter, the equations for the Navier-Stokes are presented, followed by the equations for the three turbulence models used in this thesis which are: the one-equation Spalart-Allmaras, the two-equation SST $k-\omega$ and the four-equation Transition SST models. Next will be the wall treatment method used with all three turbulence models. The D-VAWT geometry and parameters will be presented followed by the theoretical analysis for the estimation of the D-VAWT's performance.

2.1 Governing Equations

CFD simulations are performed by solving the discretized Navier-Stokes equations. However, this can be extremely expensive if one wishes to solve the complete Navier-Stokes through DNS simulations. Instead, the time averaged equations, named Reynolds Averaged Navier-Stokes (RANS), are solved, which offers enough accuracy for most engineering applications.

Typically for VAWT analysis, the flow is assumed to be incompressible as it simplifies the equations without loss of accuracy. The strong formulation of the incompressible and unsteady Navier-Stokes equations for Newtonian fluids are:

$$\nabla \cdot \vec{u} = 0 \quad (2.1)$$

$$\rho \frac{\partial \vec{u}}{\partial t} + \rho(\vec{u} \cdot \nabla)\vec{u} = -\nabla p + \mu \nabla^2 \vec{u} + f \quad (2.2)$$

where \vec{u} is the velocity vector, μ is dynamic viscosity and f is body forces.

The instantaneous flow fields such as velocity and pressure are decomposed into mean and fluctuating components such as

$$u_i = \bar{u}_i + u'_i \quad (2.3)$$

$$p = \bar{p} + p' \quad (2.4)$$

where u_i and p are the instantaneous velocity and pressure components, \bar{u}_i and \bar{p} are the mean velocity and pressure components, and u'_i and p' are the fluctuating velocity and pressure components. The fluctuating and mean velocity and pressure components vary both in time and space. The subscript $i = 1, 2$ and 3 refers to the each of the components in the x, y, and z direction,

respectively. Using the above mentioned decomposition and some mathematical manipulation, the RANS equation in conservative form are given by the following:

$$\frac{\partial U_i}{\partial x_i} = 0 \quad (2.5)$$

$$\rho \frac{\partial U_i}{\partial t} + \rho \frac{\partial}{\partial x_j} (U_j U_i + \overline{u'_j u'_i}) = -\frac{\partial P}{\partial x_i} + \frac{\partial}{\partial x_j} (2\mu S_{ij}) \quad (2.6)$$

where $-\overline{u'_j u'_i}$ is the average of the product of the velocity fluctuations in the i and j directions, $-\overline{u'_j u'_i} = \tau_{ij}$, called the specific Reynolds Stress tensor, U_i is the mean velocity in the i direction, and S_{ij} is the strain rate tensor

$$S_{ij} = \frac{1}{2} \left(\frac{\partial u_i}{\partial x_j} + \frac{\partial u_j}{\partial x_i} \right) \quad (2.7)$$

Based on the Boussinesq approximation, the specific Reynolds Stress tensor can be express as a product of eddy viscosity, ν_t , and local mean flow strain rate.

$$-\rho \overline{u'_j u'_i} = \rho \nu_t \left(\frac{\partial U}{\partial y} + \frac{\partial V}{\partial x} \right) \quad (2.8)$$

After simplifying the Navier-Stokes equation in conservation form, we obtain the more common expression for the RANS equation.

$$\rho \frac{\partial U_i}{\partial t} + \rho U_j \frac{\partial U_i}{\partial x_j} = -\frac{\partial P}{\partial x_i} + \frac{\partial}{\partial x_j} (2\mu S_{ij} - \rho \overline{u'_j u'_i}) \quad (2.9)$$

In the above form, there are more unknown variables than equations to solve, meaning the system is not yet closed. The task of turbulence modelling is to find enough equations to solve all the unknowns and solve for the eddy viscosity variable, which relates the RANS equation with the turbulence model equations through the Boussinesq approximation. In the next sub-sections, the equations for each of the turbulence models used in this thesis are presented.

2.2 Turbulence Modelling

2.2.1 Spalart-Allmaras

The first model is the one-equation Spalart-Allmaras (SA) model [53, 54] with *Strain/Vorticity-Based Production*. It should be noted that the Spalart-Allmaras Strain/Vorticity-Based Production is referred to as SA Strain in all graphs and tables in this thesis and in the text it is referred to as

SA Strain/Vorticity. This model was intended for aerospace application, which makes it a good candidate for a Darrieus type VAWT simulations, since the blades have an airfoil shape for their profile.

The governing equation for the SA model is represented by [55]:

$$\frac{\partial}{\partial t}(\rho\tilde{\nu}) + \frac{\partial}{\partial x_i}(\rho\tilde{\nu}u_i) = G_\nu + \frac{1}{\sigma_{\tilde{\nu}}}\left[\frac{\partial}{\partial x_i}\left\{(\mu + \rho\tilde{\nu})\frac{\partial\tilde{\nu}}{\partial x_i}\right\} + C_{b2}\rho\left(\frac{\partial\tilde{\nu}}{\partial x_i}\right)^2\right] - Y_\nu + S_{\tilde{\nu}} \quad (2.10)$$

Where G_ν is the production term, Y_ν is the dissipation term, ν is viscosity, $\sigma_{\tilde{\nu}}$ and C_{b2} are constants, and $S_{\tilde{\nu}}$ is a source term. The transport variable, $\tilde{\nu}$, is equivalent to the turbulent kinematic viscosity, specifically for the near-wall region. The turbulent eddy viscosity is computed by the following:

$$\mu_t = \rho\tilde{\nu}f_{v1} \quad (2.11)$$

where the three closure functions are given by:

$$f_{v1} = \frac{\chi^3}{\chi^3 + C_{v1}^3} \quad (2.12)$$

$$f_{v2} = 1 - \frac{\chi}{\chi + \chi}f_{v1} \quad (2.13)$$

$$f_w = g\left(\frac{1 + c_{w3}^6}{g^6 + c_{w3}^6}\right)^6 \quad (2.14)$$

The production term is given by the following equation:

$$G_\nu = C_{b1}\rho\tilde{S}\tilde{\nu} \quad (2.15)$$

where

$$\tilde{S} = S + \frac{\tilde{\nu}}{\kappa^2 d^2}f_{v2} \quad (2.16)$$

The deformation tensor, S , incorporates both, the strain and vorticity tensors which is represented by:

$$S \equiv |\Omega_{ij}| + C_{prod} \cdot \min(0, |S_{ij}| - |\Omega_{ij}|) \quad (2.17)$$

where

$$C_{prod} = 2.0 \quad (2.18), \quad |\Omega_{ij}| \equiv \sqrt{2\Omega_{ij}\Omega_{ij}} \quad (2.19), \quad |S_{ij}| \equiv \sqrt{2S_{ij}S_{ij}} \quad (2.20)$$

with the mean strain rate, S_{ij} is defined as:

$$S_{ij} = \frac{1}{2} \left(\frac{\partial u_j}{\partial x_i} + \frac{\partial u_i}{\partial x_j} \right) \quad (2.21)$$

2.2.2 Shear-Stress Transport k- ω

The two-equation Shear-Stress Transport (SST) k- ω [56, 57] model has a similar form to the standard k- ω model. It combines the benefits of the k- ϵ model in free flow with the advantages of the standard k- ω for near wall flows. The governing equations are given by the following [55]:

$$\frac{\partial(\rho k)}{\partial t} + \frac{\partial(\rho k u_j)}{\partial x_j} = \frac{\partial}{\partial x_j} \left(\Gamma_k \frac{\partial k}{\partial x_j} \right) + \widetilde{G}_k + -Y_k + S_k \quad (2.22)$$

and

$$\frac{\partial(\rho \omega)}{\partial t} + \frac{\partial(\rho \omega u_j)}{\partial x_j} = \frac{\partial}{\partial x_j} \left(\Gamma_\omega \frac{\partial \omega}{\partial x_j} \right) + G_\omega - Y_\omega + D_\omega + S_\omega \quad (2.23)$$

where \widetilde{G}_k is the generation of turbulence kinetic energy due to the mean velocity gradients, G_ω is the generation of ω , Y_k and Y_ω are the dissipation of k and ω due to turbulence, D_ω is the cross diffusion term, and S_k and S_ω are the defined source terms given by the user. Γ_k and Γ_ω are the effective diffusivities of k and ω , and are calculating using the following equations:

$$\Gamma_k = \mu + \frac{\mu_t}{\sigma_k} \quad (2.24)$$

$$\Gamma_\omega = \mu + \frac{\mu_t}{\sigma_\omega} \quad (2.25)$$

where σ_k and σ_ω are the turbulent Prandle numbers for k and ω , respectively. μ_t is the turbulent viscosity called by the following:

$$\mu_t = \frac{\rho k}{\omega} \frac{1}{\max \left[\frac{1}{\alpha^*}, \frac{SF_2}{\alpha_1 \omega} \right]} \quad (2.26)$$

where S is the Strain rate magnitude. The rest of the equations and closure variable are available in ANSYS Fluent's Theory guide [55].

2.2.3 Transition Shear-Stress Transport

The last turbulence model is the four-equation Transition SST model [58, 59], which is based on coupling the SST k- ω equation with another two transport equations. One transport equation for

the intermittency, γ , and the other for the transition onset criteria, which is represented in terms of momentum-thickness Reynolds number, $R\tilde{e}_\theta$.

The transport equation for intermittency is given by [55]:

$$\frac{\partial(\rho\gamma)}{\partial t} + \frac{\partial(\rho U_j \gamma)}{\partial x_j} = P_{\gamma 1} - E_{\gamma 1} + P_{\gamma 2} - E_{\gamma 2} + \frac{\partial}{\partial x_j} \left[\left(\mu + \frac{\mu_t}{\sigma_\gamma} \right) \frac{\partial \gamma}{\partial x_j} \right] \quad (2.27)$$

where the transition sources are defined as:

$$P_{\gamma 1} = C_{a1} F_{length} \rho S [\gamma F_{onset}]^{c_{\gamma 3}} \quad (2.28)$$

$$E_{\gamma 1} = C_{e1} P_{\gamma 1} \gamma \quad (2.29)$$

where S is the strain rate magnitude, F_{length} is an empirical correlation that controls the length of the transition region, and C_{a1} and C_{e1} are equal to 2 and 1, respectively. The destruction/relaminarization sources are defined as follows:

$$P_{\gamma 2} = C_{a2} \rho \Omega \gamma F_{turb} \quad (2.30)$$

$$E_{\gamma 1} = C_{e2} P_{\gamma 2} \gamma \quad (2.31)$$

where Ω is the vorticity magnitude.

The transport equation for the transition momentum-thickness Reynolds number, $R\tilde{e}_\theta$ is

$$\frac{\partial(\rho R\tilde{e}_\theta)}{\partial t} + \frac{\partial(\rho U_j R\tilde{e}_\theta)}{\partial x_j} = P_{\theta t} + \frac{\partial}{\partial x_j} \left[\sigma_{\theta t} (\mu + \mu_t) \frac{\partial R\tilde{e}_\theta}{\partial x_j} \right] \quad (2.32)$$

where the source term is defined as:

$$P_{\theta t} = c_{\theta t} + \frac{\rho}{t} (Re_{\theta t} - R\tilde{e}_\theta) (1.0 - F_{\theta t}) \quad (2.33)$$

The transition model interacts with SST k - ω turbulence model by modification of the k -equation as follows:

$$\frac{\partial(\rho k)}{\partial t} + \frac{\partial(\rho k u_i)}{\partial x_j} = \frac{\partial}{\partial x_j} \left(\Gamma_k \frac{\partial k}{\partial x_j} \right) + G_k^* - Y_k^* + S_k \quad (2.34)$$

where

$$G_k^* = \gamma_{eff} \tilde{G}_k \quad (2.35)$$

$$Y_k^* = \min(\max(\gamma_{eff}, 0.1), 1.0) Y_k \quad (2.36)$$

where \widetilde{G}_k and Y_k are the original production and destruction terms from the SST k- ω model.

The details of the equations can be found in Fluent's theory guide [55]. The advantage of this model is that it is capable of accurately predicting where and when the flow will change from laminar to transitional and turbulent flow and calculating the flow accordingly. This can be especially important for turbine simulations since depending on the blade position, the flow does indeed change from laminar to turbulent. This happens mainly in the lower section during the turbine rotation, where the blade sees a reduction in the flow speed. This is why this model is expected to provide the most accurate results. This model requires $y^+ < 5$ to capture the transition onset correctly; however, ideally, the y^+ should be less than 1.

2.3 Wall Treatment

Figure 2.1 shows the law of the wall, which is the velocity profile in the near-wall region based on a semi-empirical formula. One can see that profile is composed of three regions in the inner layer, which are dictated by the dimensionless distance, y^+ . The three regions are the viscous sublayer, buffer region and log law region. The y^+ is defined as

$$y^+ = \frac{\rho u_\tau y}{\mu} \quad (2.37)$$

where u_τ is the friction velocity and y is the normal distance from the wall.

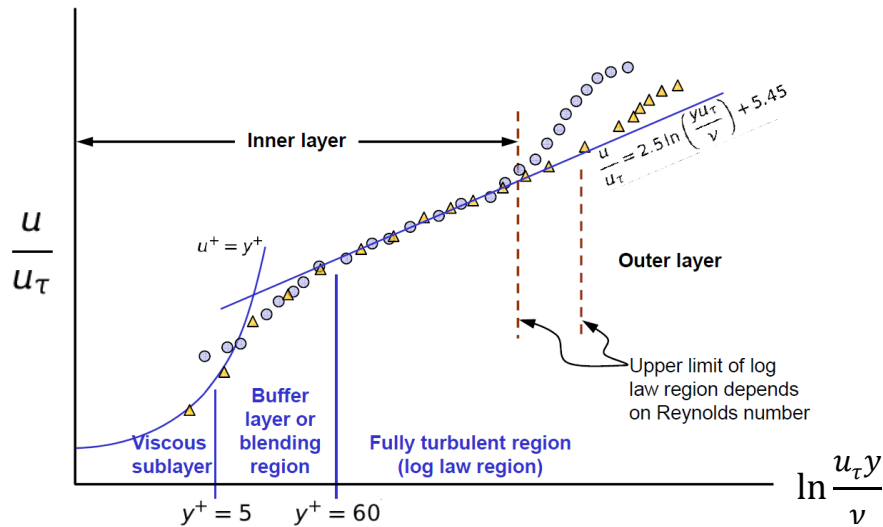


Figure 2.1: Law of the Wall [55]

There are two common approaches of simulating the flow near walls. Wall functions are semi-empirical formulas that bridge the flow between the highly viscous flow in the boundary layer and the free stream flow. The typical range for the smallest element is at $y^+ > 30$, where the flow and its properties below that said y^+ are calculated with the wall functions. If a mesh with elements smaller than y^+ of 15 is used, the flow deteriorates and results in unbound errors [55]. The second approach resolves the flow all the way to the wall, including the viscous sublayer. This obviously requires a much finer mesh to capture the flow details, but typically has higher accuracy in its flow prediction.

For all simulations performed in this thesis, the Enhanced Wall Treatment (EWT) is used, which is the default wall treatment, in Fluent, for the three previously presented turbulence models. The Enhanced Wall function is versatile in its use since it combines the behavior of the two previously mentioned approaches. It allows the use of coarse meshes, where the flow will be resolved to the smallest element, and below that said smallest element, the wall function will take over and approximate the effects. Having said that, if the mesh is fine enough (below $y^+ < 1$), then the flow will be completely resolved without the wall function being activated. EWT performances are thus considered to be independent of the y^+ .

2.4 Original Turbine Geometry

As mentioned before, the idea of the D-VAWT lies in extending the regions where the most power is extracted from a conventional H-Darrieus type VAWT. The D-VAWT's blade path and region nomenclature are shown in Figure 2.2, where the axes spacing, L , is the distance between the two axes of rotation and R is the radius of rotation. The D-VAWT's path is composed of four regions: Rotational Region 1, Upstream Translational Region, Rotation Region 2, and Downstream Translational Region. From the same figure, one can also see the blade starting point. The original dimensions of the investigated turbine are presented in Table 2.1.

For the initial analysis, a ratio of L/R is set as 4. Further investigation will be needed to find the optimal ratio of L/R . Also, it should be noted that a D-VAWT with only a single blade is initially investigated as the mesh and motion methodology needed for more than one blade is more complex and will greatly increase the simulation time, while the initial purpose is to first investigate the methodology and feasibility of this new design. The selected airfoil profile is a NACA 0018 for

its high lift characteristics. The mounting point of the blade is at $1/3 C$ away from the leading edge; however this will also need investigation to find whether it is the optimal mounting point.

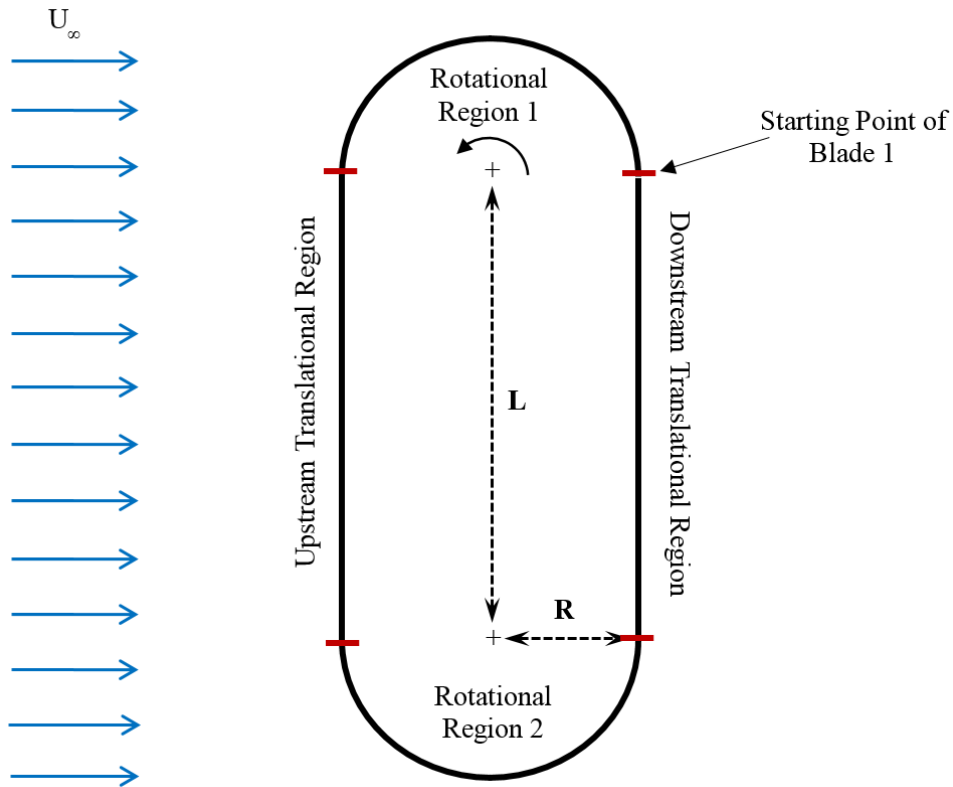


Figure 2.2: Top View of a D-VAWT Path

Table 2.1: D-VAWT Geometrical Characteristics

D-VAWT Characteristics	
Axes Spacing, L	3.2 m
Chord, C	0.4 m
Airfoil Profile	NACA 0018
Radius, R	0.8 m
L/R Ratio	4
Blade Aspect Ratio, AR=h/C	5 and 15

2.5 Parameters for the D-VAWT

Based on their original definitions, some of the previously mentioned parameters are modified to be used appropriately for a D-VAWT and others are newly defined. Since the equation for the TSR is the same for VAWTs and D-VAWTs, it will not be presented again here.

2.5.1 Swept Area

The swept area is defined as the projected area that is normal to the incoming wind. For the D-VAWT case, the swept area becomes a function of the incoming wind direction.

$$A = (L \cos(\varphi) + 2R) h \quad (2.38)$$

Where h is the height of the turbine, which is equal to unity for a 2-D analysis, and φ is the incoming incident wind angle, where $\varphi = 0^\circ$ is for the case shown in Figure 2.2 with the flow normal to the longitudinal side of the turbine or the line connecting the two axes (L).

2.5.2 Coefficient of Power

The coefficient of power is defined as the ratio of extracted power to the available power in the incoming wind. The typical method to calculate the C_P for a VAWT is based on the torque produced by the blade. However, since the D-VAWT blade follows a non-circular path, it is not appropriate to use torque in regions where the blade is not rotating.

Two methods are described here to calculate the coefficient of power with their procedures summarized in Figure 2.3. The $C_{P, \text{Force}}$ (force based method) is obtained by using the forces on the blade in the x and y direction calculated from Fluent, and then finding the power producing force which will be the tangential force on the blade. As for the $C_{P, \text{Torque}}$ (torque based method), it is obtained from the torque on the blade at the appropriate moment center since the center of the blade moment center changes throughout the cycle. To find the moment center, a scheme variable is defined in Fluent that is updated at each time step using a User Defined Function (UDF). The moment center is updated to follow the motion of the blade between the two axes.

Neither methods alone correctly represents the actual C_P performance of a D-VAWT, however, the combination of both is necessary to do so. Similar to regular VAWTs, in the regions where the blade is rotating, the $C_{P, \text{Torque}}$ is used since it is the torque that produces power in those regions. In the regions where the blade moves in a straight path, the $C_{P, \text{Force}}$ is used as the torque would not be appropriate to use in those sections since part of the torque would be seen as stresses on the

mechanism and would not help produce power. The reason the $C_{P, Force}$ is not used for the rotating regions is because the location where the forces apply on the blade (center of pressure) is needed to calculate the turbine torque (power) correctly, which is difficult to obtain during the simulation for all blade positions.

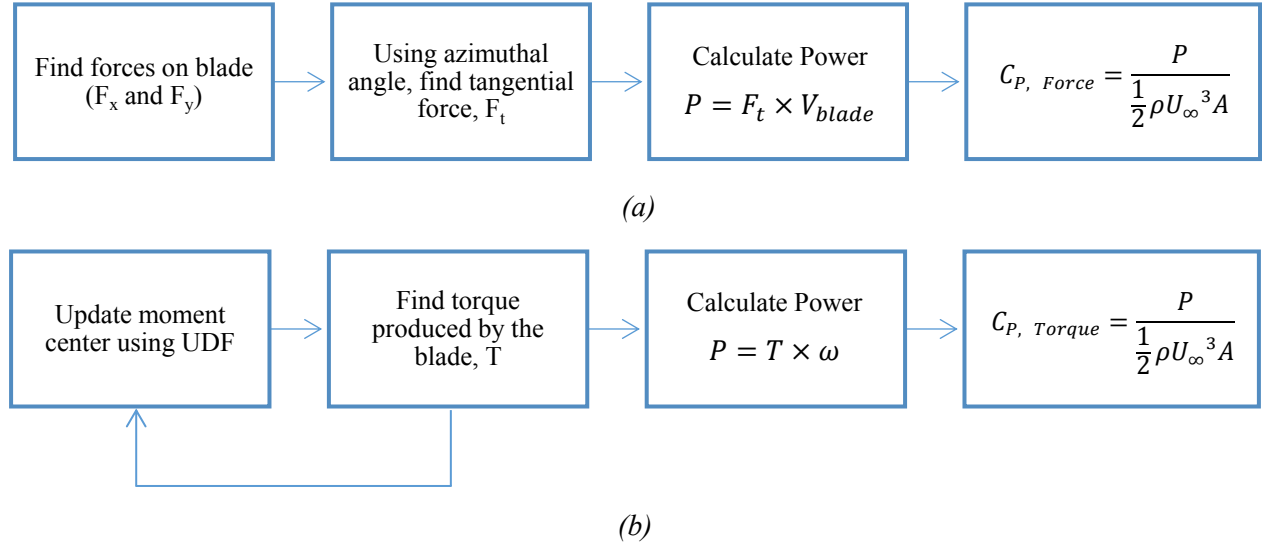


Figure 2.3: Steps for Coefficient of Power Calculation (a) Force Based, (b) Torque Based

The resultant C_P curve obtained from the combination of the two methods can be seen in Figure 2.4 and the equation to calculate the coefficient of power for a D-VAWT during one cycle becomes

$$C_P = \frac{P}{\frac{1}{2}\rho U_\infty^3 A} = \frac{T_{Rotating} \omega + F_{Translating} V_{blade}}{\frac{1}{2}\rho U_\infty^3 A} = C_{P, Torque} + C_{P, Force} \quad (2.39)$$

where $T_{Rotating}$ is the sum of the torque produced when the blade is rotating, $F_{Translating}$ is the sum of the tangential force produced when the blade is translating for a single cycle, $C_{P, Torque}$ is the coefficient of power for the rotational regions, and $C_{P, Force}$ is the coefficient of power for the translational regions.

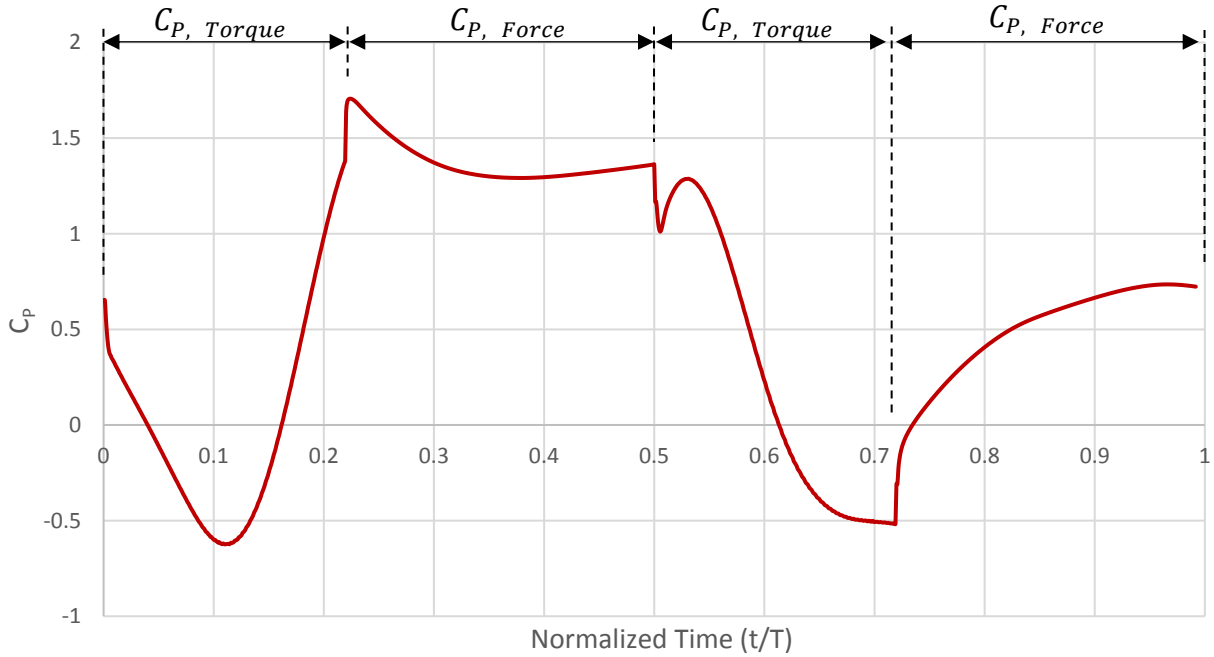


Figure 2.4: Instantaneous Coefficient of Power Curve Based on the Combination of both the Force and Torque Based Methods

2.5.3 Solidity

The solidity is a relation between the total blade areas to the projected turbine area.

$$\sigma = \frac{N_b C}{R + \frac{L}{2}} \quad (2.40)$$

Where N_b is the number of blades.

2.5.4 Axis Eccentricity Factor

The newly defined parameter for D-VAWTs is the Axis Eccentricity Factor (AEF), which dictates the distance between the two axes. It is defined as the ratio of the axes spacing to the radius.

$$\varepsilon = AEF = \frac{L}{R} \quad (2.41)$$

This parameter will greatly influence the behavior and performance of the turbine and will need further investigation. A value of zero would mean that the two axes overlap and the resultant is a circular shape, which is that of a conventional VAWT.

2.6 Theoretical Power Coefficient in Upstream Translational Region

Before performing any flow simulations, an approximate calculation is done to have a baseline of comparison with the flow simulations in 2D. This estimation is done only for the upstream translational region since it is the part of most interest for this turbine.

The equations used to calculate the theoretical C_P are presented in sequence below, while the results are summarized in Table 2.2. The first step in deciding the operating conditions of the D-VAWT is to choose an angle of attack, where the NACA 0018 would produce a high lift to drag ratio. The values of lift and drag for the NACA 0018 are taken from [60]. Based on eq. (2.42), the angle of attack also dictates the TSR of the turbine. For the selected angle of attack at Reynolds number of 500,000, the blade would have a TSR of 4.5. The calculations are performed for an incoming wind speed of 4 m/s, which is a typical value for urban applications.

$$\alpha = \tan^{-1}\left(\frac{1}{\lambda}\right) \quad (2.42)$$

Where α is the angle of attack of the blade and λ is the tip speed ratio. This equation relates the angle of attack and the TSR and it only applies when the blade is normal to the wind direction.

$$\lambda = \frac{V_{blade}}{U_\infty} = \frac{\omega R}{U_\infty} \rightarrow V_{blade} = \lambda U_\infty \quad (2.43)$$

Where V_{blade} is the airfoil velocity, also equal to ωR , and U_∞ is the free stream velocity.

$$V = \sqrt{V_{blade}^2 + U_\infty^2} \quad (2.44)$$

Where V is the velocity seen by the blade.

$$F_t = L \sin(\alpha) - D \cos(\alpha) = \frac{1}{2} C_L \rho V^2 A_{AF} \sin(\alpha) - \frac{1}{2} C_D \rho V^2 A_{AF} \cos(\alpha) \quad (2.45)$$

Where F_t is the tangential force, along the chord of the blade, that will be producing power, L and D are the lift and drag forces, C_L and C_D are the coefficients of lift and drag for the respective angle of attack, and $A_{AF} = C h$, is the airfoil planform area.

$$P = F_t V_{blade} \quad (2.46)$$

Where P is the power produced. To calculate the C_P , Eq. (1.2) is used, where the density of air is 1.225 Kg/m³.

Table 2.2: Summary of Theoretical Results

Theoretical Results	
Angle of attack in Translational Region, α [deg]	12.53
Tip Speed Ratio, λ	4.5
Chosen Incoming Wind Speed, U_∞ [m/s]	4
Blade Velocity, V_{blade} [m/s]	18
Velocity seen by blade, V [m/s]	18.44
Coefficient of Lift, C_L at α [60]	0.961
Coefficient of Drag, C_D at α [60]	0.0323
Tangential Force, F_t [N]	14.74
Power Produced, P [W]	265.3
Coefficient of Power, $C_{P, \text{Force}}$	1.41

As seen from Table 2.2, the expected C_P to be produced in the upstream translational region is 1.41, which is very high for a wind turbine considering that the highest average C_P per cycle that conventional VAWTs can draw is between 0.2 and 0.4. For this reason, extending the translational region should help increase the overall aerodynamic efficiency of Darrieus type VAWTs. It should be noted that the predicted value should only be compared with that of the 2D simulations, since the values for the coefficient of lift and drag are that of an “infinitely” long airfoil.

2.7 Analysis Milestones

Figure 2.5 summarizes the approach taken in this thesis to validate the methodology and analyze the D-VAWT.

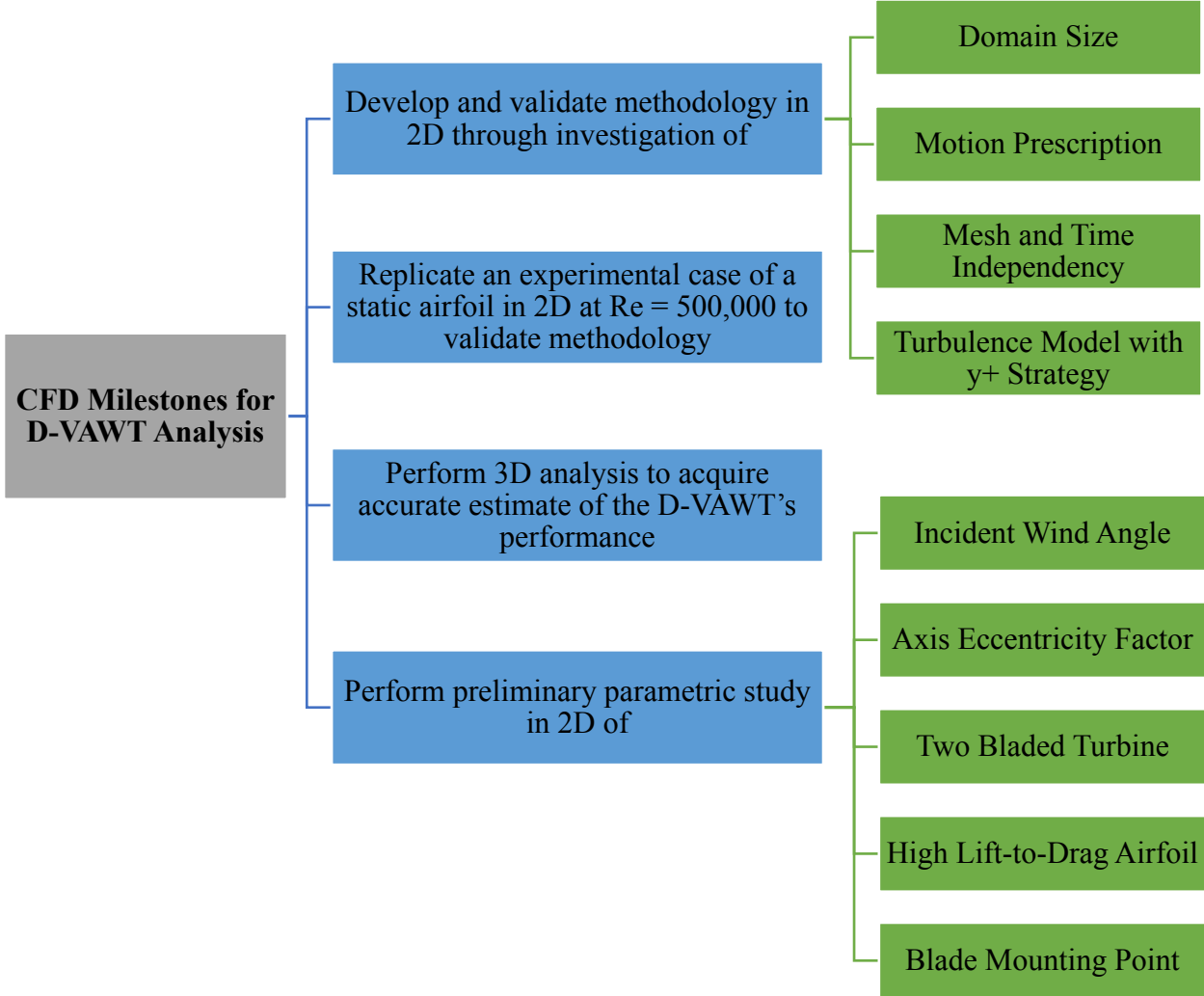


Figure 2.5: Milestones for the CFD Analysis of the D-VAWT

CHAPTER 3: METHODOLOGY VALIDATION IN 2D

Our first simulations performed on the D-VAWT [61] served as the initial proof of concept. Those said results will not be presented here as they were obtained with an initial methodology, which was not yet validated at the time. However, it served as the initial proof of concept of the D-VAWT design.

Because of the large number of existing methodologies used for VAWT analysis, the lack of consistency, and the fact that the D-VAWT is a new turbine that has not never been analyzed with CFD, the methodologies found in the literature review are used only as an initial guideline. This chapter focuses on the validation of the chosen methodology through CFD validation techniques (domain size, different motion prescription techniques, mesh and time convergence, turbulence model study) as well as validation through replication of an experimental case study.

3.1 Numerical Setup

The analysis of the D-VAWT is performed through CFD means using the finite-volume commercial code ANSYS Fluent 14.5 [17] to solve the URANS equations. Pressure based transient simulation is used to solve the flow. The turbulence model constants are left as default for all turbulence models used. The value for the density of air, ρ , is set to $1.225 \frac{kg}{m^3}$ and the dynamic viscosity, μ , is $1.7894 \times 10^{-5} \frac{kg}{m.s}$.

The SIMPLE (Semi-Implicit Method for the Pressure Linked Equations) algorithm is employed for the pressure-velocity coupling. The SIMPLE algorithm uses a relationship between velocity and pressure corrections to enforce mass conservation and to obtain the pressure field. The SIMPLE algorithm is much more commonly used for VAWT analysis as seen in the literature review when compared to the Pressure Implicit with Splitting of Operators (PISO) algorithm. The PISO algorithm is typically used for transient simulations or for meshes with higher than average element skewness; however, the SIMPLE algorithm is more robust in nature.

For the spatial discretization, the pressure is calculated using a second order scheme, while the momentum and all turbulent properties formulations are calculated using second order upwind schemes. Gradients of solution variables are required in order to evaluate diffusive fluxes, velocity

derivatives, and for higher-order discretization schemes. The gradients of solution variables at cell centers are determined using the Least-Squares Cell-Based method. The gradients of solution variables at faces are computed using multi-dimensional Taylor series expansion. As for the transient formulation, a first order implicit scheme is required due to the limitations imposed by Fluent while the dynamic mesh capabilities are active. The dynamic mesh is needed to simulate the unconventional blade path of the D-VAWT. Fluent's default values for the under-relaxation factors are used.

All simulations are performed with an absolute convergence criterion of 10^{-3} for the continuity, velocity components and all turbulent properties. Though a convergence criterion of 10^{-5} was tested, the results were near identical with the advantage of having lower computational time. The size of the time step is $\Delta t = 0.5585\text{ms}$ or about one thousandth of a period ($T/1136$), where T is the period. The steps taken to select the time step are outlined next.

First, it was decided to have 500 time steps if the blade was to do one full rotation in a circular path, or equivalently, the blade moves about $360^\circ/(500 \text{ time steps}) = 0.72^\circ$ per time step. Based on the angular velocity of 22.5 rad/s (obtained from $\text{TSR} = 4.5$ and $U_\infty = 4 \text{ m/s}$), the time step is $\Delta t = \frac{2\pi}{22.5 \times 500} = 0.5585\text{ms}$. With this value, the number of time steps it takes to complete one side of the translational region equals to $\frac{L}{v_{blade} \times \Delta t} = 318$ time steps and the total number of time steps to complete a full cycle of a D-VAWT is $500 + 318 \times 2 = 1136$.

For the boundary conditions, shown in Figure 3.1, uniform and constant velocity inlets are defined for the left, top and bottom boundaries with incoming wind speeds of 4m/s , which is a typical wind speed value for urban applications. The right boundary is defined with a pressure outlet condition. The incoming turbulent boundary conditions parameters are defined with a turbulent intensity of 5% and a turbulent viscosity ratio $\frac{\nu_t}{\nu} = 5$, where the kinematic viscosity, ν , of air is $1.4607 \times 10^{-5} \frac{\text{m}^2}{\text{s}}$. As for the blade boundary condition, a no-slip condition is applied. All cases use the standard initialization method based on the inlet condition values.

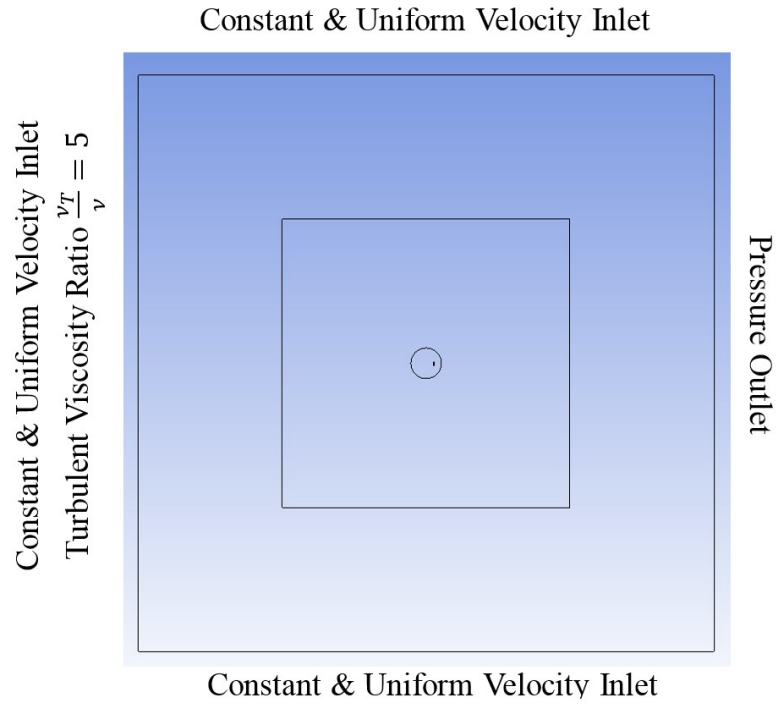


Figure 3.1: Initial Domain with Boundary Conditions

3.2 Initial Domain

The domain, based on the initial simulation of the D-VAWT in [61], is shown in Figure 3.1 with a closer view of the rotating domain and refinement region around the blade shown in Figure 3.2. The rotating domain diameter is twice the diameter of the D-VAWT and the outer domain is a square with sides equal to 100 times the blade chord.

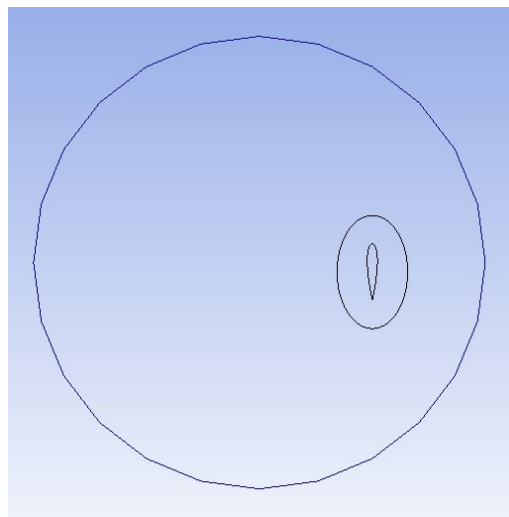


Figure 3.2: View of the Rotating Domain and Blade Refinement Region

3.3 Investigation of Domain size

The domain size and motion prescription study were performed using the one-equation SA Strain/Vorticity turbulence model with a $y^+ \sim 30$ as it was seen from literature that for high TSR values, the choice of model should have little effect on the results. The purpose of this test was to determine the smallest possible domain size that would not affect the results. The mesh used in this study was finer than needed, which was only realized after the mesh convergence study. The domain contained 135,000 elements, mainly focused around the airfoil. The summary of the results and domain sizes tested are shown in Table 3.1, where it can be seen that changing the domain from 150C to 250C resulted in a change of less than 2%. Figure 3.3 shows the C_P in the last cycle for all three cases, where the difference in C_P can be mainly seen the translational part of the blade path. It was then decided to use a domain of 150C for the rest of the simulations as it provided enough accuracy for the current objectives. For all 2D simulations presented in this thesis, all elements across any interface are matched in size to reduce interpolation errors.

Table 3.1: Results Summary for Domain Size Study

Static Deforming Domain Size	Translating Domain Size	Average C_P in last 3 cycles	C_P % Difference to Previous Case
100 C	75 C	0.523	-
150 C	75 C	0.504	3.77
250 C	100 C	0.494	2

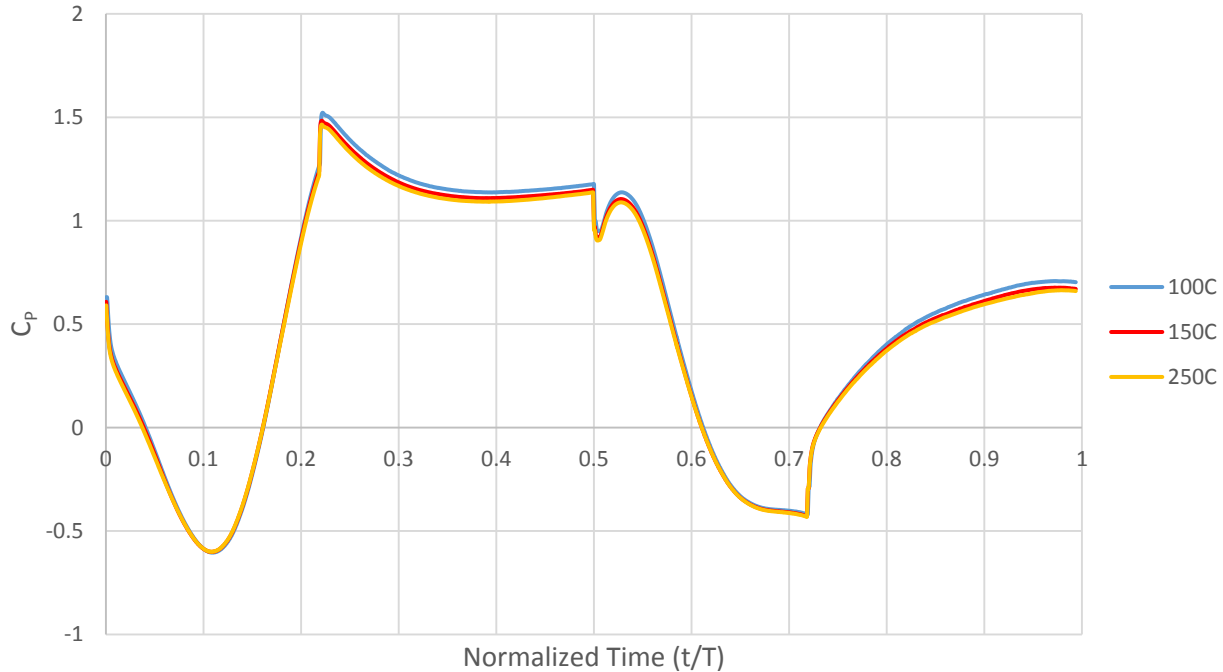


Figure 3.3: Instantaneous C_p vs. Normalized Time of the 10th Cycle for Different Domain Sizes

3.4 Different Motion Methodology

In this section, three possible methods to specify the motion of the blades are presented. The following section presents the description of each of those methods with the comparison of the results presented at the end. For all motion types of the D-VAWT blade, the motion is prescribed in Fluent through the use of UDFs. A domain size of 150 C is used for all three cases based on the domain size investigation.

3.4.1 Motion Type 1

For this motion type, the domain is composed of three sub-domains: a rotating domain, a translating domain, and a static deforming domain. In Figure 3.4, the three domains, their interfaces, and the motion of each are presented. A sliding mesh approach is employed for the motion of the rotational domain to allow the blade to rotate at both ends of the path. The translating domain is needed to simulate the translational motion by moving up and down perpendicularly to the flow. The outer static deforming domain acts as a buffer region where the elements would deform during the time where the translating domain is moving. The mesh used for this simulation can be seen in Figure 3.5 and Figure 3.6, where higher refinement is seen around and behind the tail of the blade. It is the same mesh used for the domain size study.

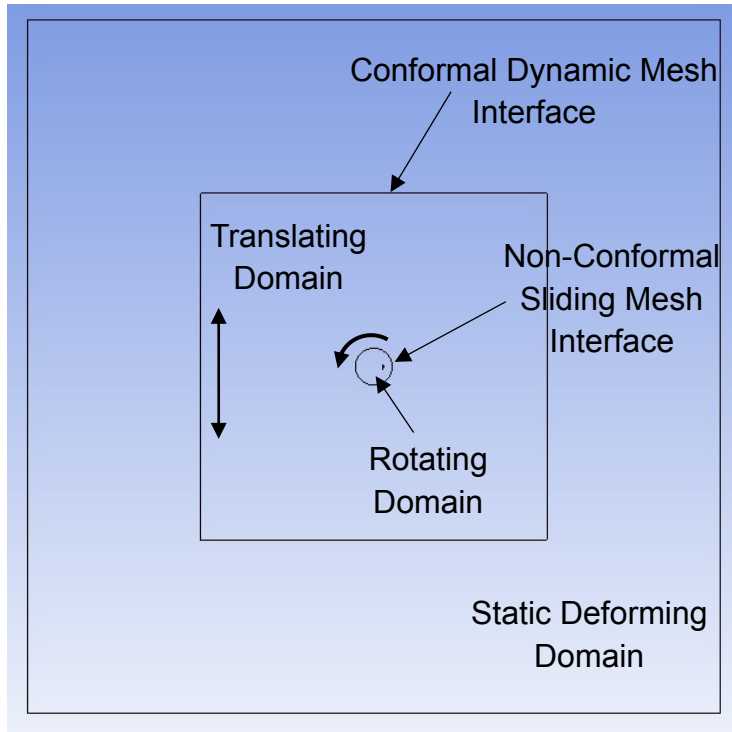


Figure 3.4: Type 1 Motion Illustration

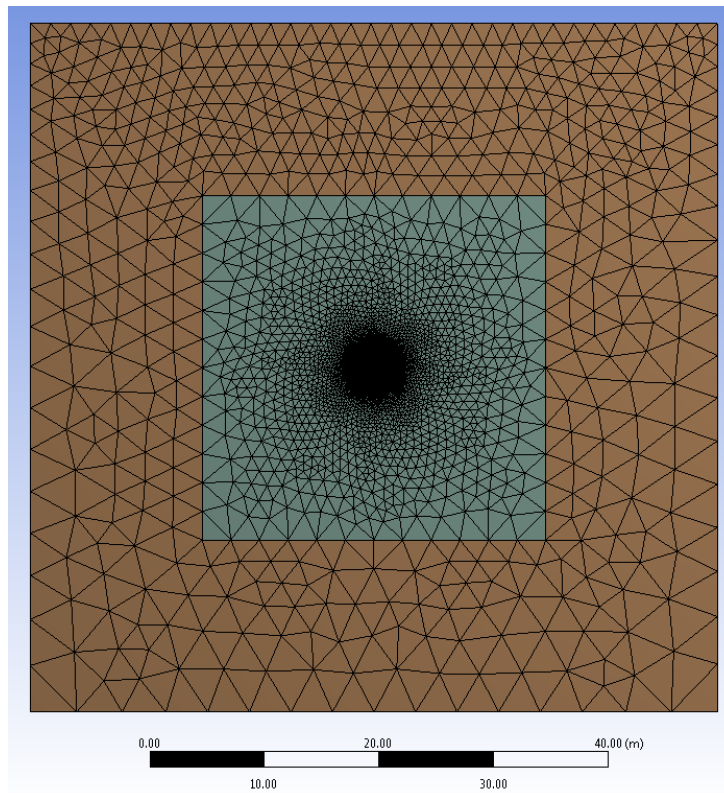


Figure 3.5: Mesh Used for Type 1 and 2 Motions

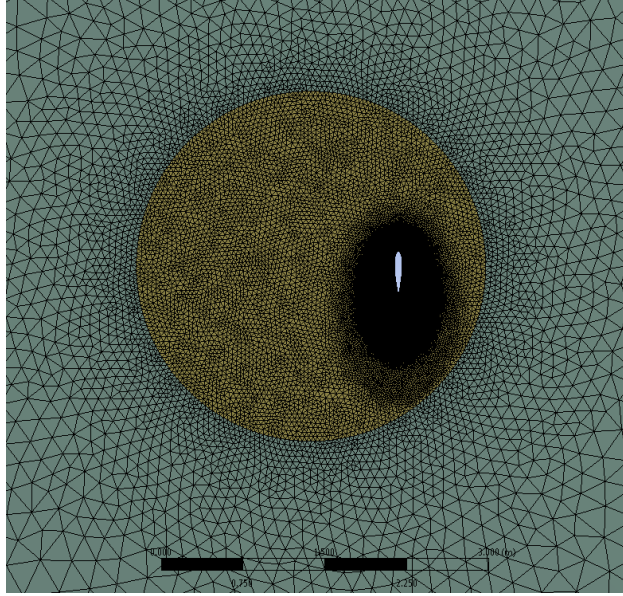


Figure 3.6: Rotating Domain Mesh for Type 1 and 2 Motions

3.4.2 Motion Type 2

The second type of motion is very similar to type 1, except the previously named static deforming domain moves along with the translating domain as one domain with no relative motion in between them. In this type of motion, there is no element deformation. The representation of the motion is shown in Figure 3.7. The same domain and mesh as for type 1 motion are used as to only have the type of motion different between the two cases and directly compare them. Special care is required when applying the boundary condition for the inlets and outlet, where they had to be specified to be independent of the mesh motion.

3.4.1 Motion Type 3

The last type of motion is presented here, and is significantly different from the previous two. The domain is composed of three sub-domains: a dynamic domain, a deforming domain, and a static domain. The representation of the domain motion is shown in Figure 3.8. In this case, the dynamic domain is the smallest of the domains and contains inside it the blade that moves in the D-VAWT trajectory, both rotating and translating accordingly. As the dynamic mesh moves, the deforming domain will have its elements both deformed and re-meshed during the motion of the blade. The static domain remains unchanged during the simulation in this case. The starting mesh used for this simulation can be seen in Figure 3.9, Figure 3.10, and Figure 3.11.

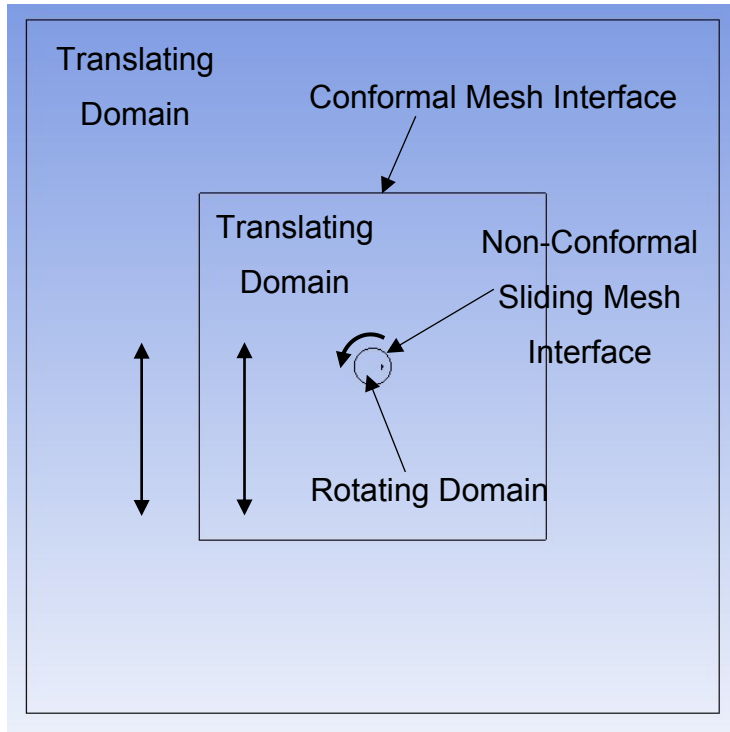


Figure 3.7: Type 2 Motion Illustration

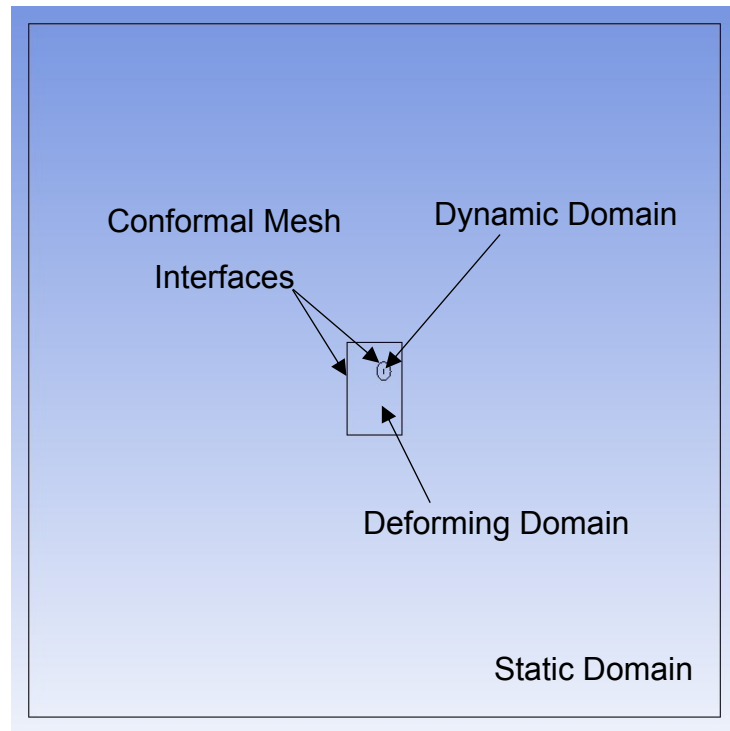


Figure 3.8: Type 3 Motion Illustration

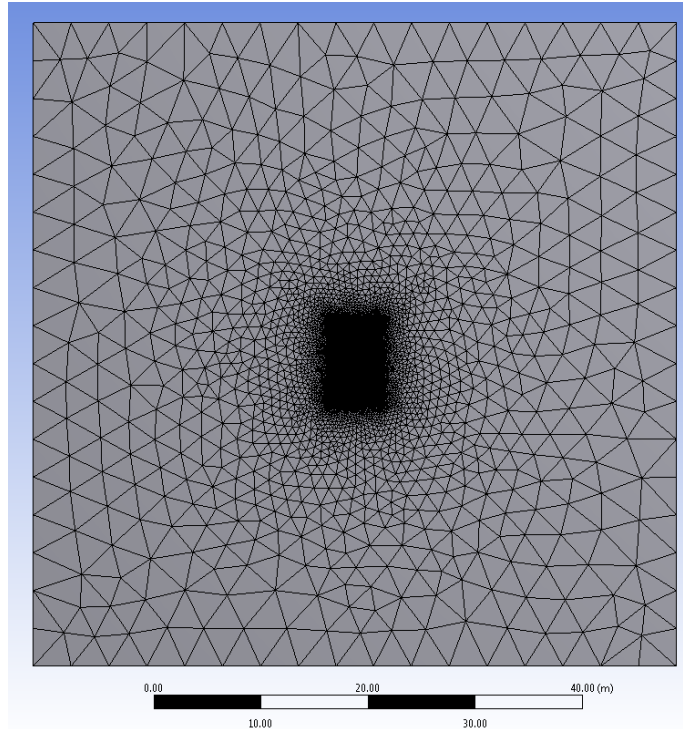


Figure 3.9: Overview of Mesh Used for Type 3 Motion

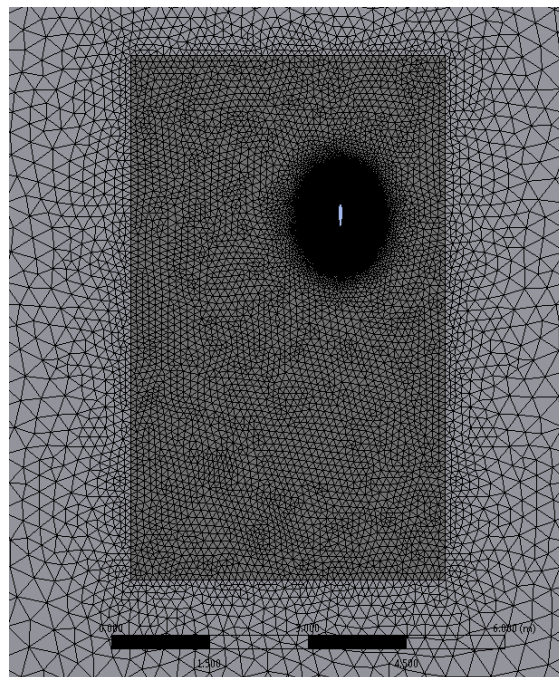


Figure 3.10: Deforming Domain Mesh View for Type 3 Motion

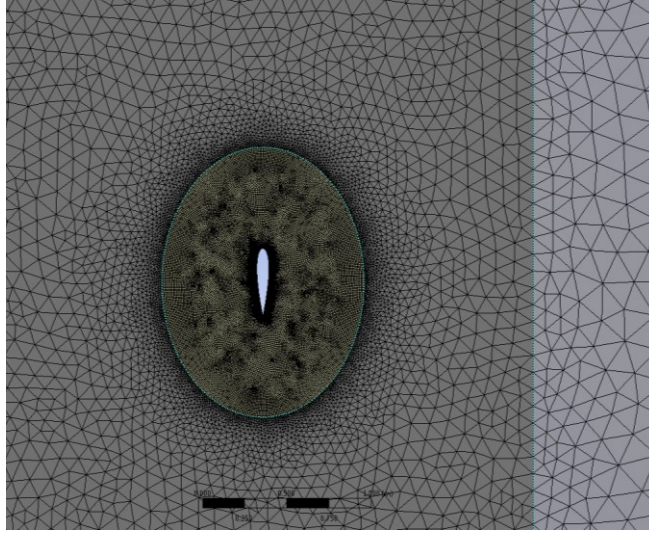


Figure 3.11: Dynamic Domain Mesh View for Type 3 Motion

3.4.2 Results and Discussion

The results for the average C_P are shown in Table 3.2 and the instantaneous C_P over the last cycle is shown in Figure 3.12. Type 3 predicts a slightly lower value in the translational and a slight deviation is noticed at the normalized time of 0.07. These differences could be due to the fact that the starting mesh was not identical to the type 1 and 2 meshes. Another reason for the possible difference is that during the simulation, there is constant re-meshing occurring, so the final mesh would be different than the one shown at the beginning of the simulation.

Table 3.2: Comparison of Results for Different Motion Types

Motion Type	Average C_P in Last 3 Cycles	C_P % Difference to Type 1	Application
1	0.504	-	Single Blade in 2D
2	0.506	0.4	Single Blade in 3D
3	0.499	1	Multi-Blade in 2D & 3D

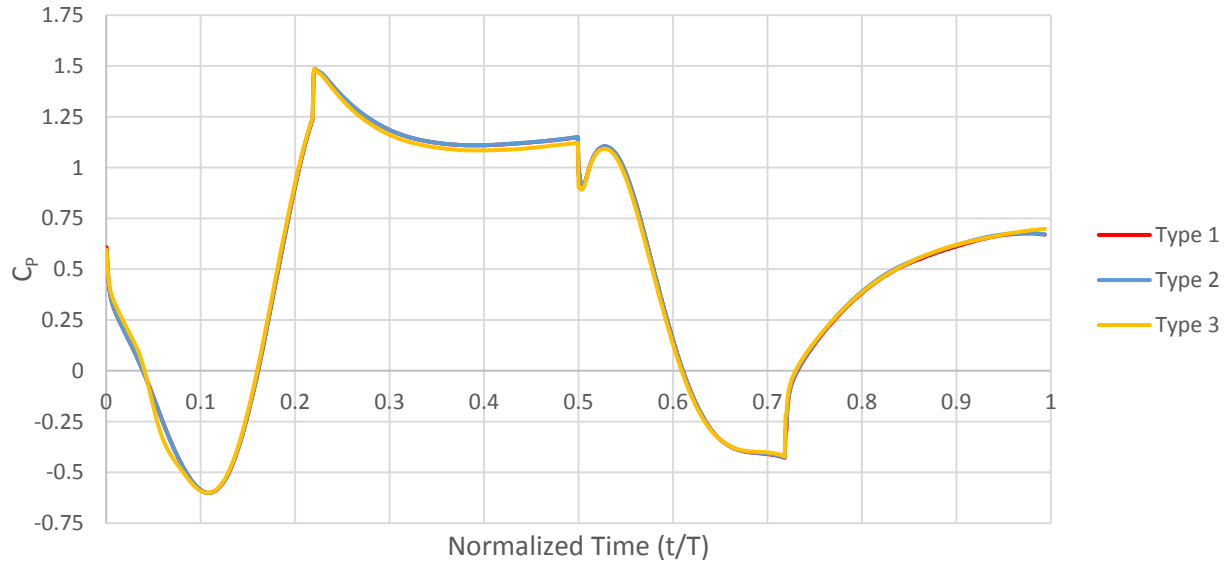


Figure 3.12: Instantaneous C_P versus Normalized Time of the 10th Cycle for Motion Types

Based on the C_P , the results for the three motion types still came to be very close to each other. The advantage of type 1 and 2 motions are shorter simulation time when compared to type 3 since no re-meshing occurs during the simulation; however, both type 1 and type 2 are limited to only having a single blade in the simulation. With type 3 motion, it is possible to have as many blades as needed in the simulation. However, the simulation time is longer and due to the fact that the mesh deforms and re-meshes throughout the simulation, additional interpolation errors are introduced. For the remainder of the 2D investigation, type 1 is used, where possible, for a single blade analysis as it is among the simplest and avoids any potential problems or errors from having the domain boundaries move. Type 2 will be used for 3D simulations to maintain the speed of the calculation but more importantly is to avoid certain complication with Fluent in 3D when using Type 1 motion. Type 3 will only be used for the parametric study of a multi-blade turbine.

3.5 Mesh Convergence Study using SST $k-\omega$ Model with $y^+ \sim 1$

Previously, a mesh of 135,000 elements was used for the initial testing of the turbine concept. This mesh was based on the finest mesh of other's simulations with the same Reynolds number of 500,000 [21]. However, at this point, it was necessary to perform a grid convergence study to determine the necessity of using either a coarser more efficient mesh or perhaps a more refined mesh to more accurately estimate the D-VAWT performance. In this section, a mesh independency study is performed to determine the most efficient mesh. Since it is necessary to perform 3D

simulations, having the coarsest mesh possible in 2D will significantly reduce the element count in 3D and improve computational time. For this study, the SST $k-\omega$ turbulence model with low Reynolds number correction is used with a $y^+ \sim 1$ as it known to have higher accuracy, especially since the entire boundary layer is resolved instead of being approximated with a wall function. In section 3.6, a turbulence model comparison is done with the selected mesh from this study to determine the effect of turbulence model choice on the results.

3.5.1 Meshes

Based on the previous investigation, type 1 motion is used with the domain sizes of 150C, 75C and 2D for the static, translating and rotating domains, respectively. Three meshes are employed for this study. An initial mesh of 45,000 elements, named Mesh 1, is used for the coarsest case. Instead of doing two levels of mesh refinement with a factor of 1.35, as recommend by Roache [62] based on the Grid Convergence Index (GCI) method developed from the theory of the generalized Richardson Extrapolation, the intermediate mesh was skipped. The finest mesh is refined with a factor of 2 or $\sim 1.4^2$. However, two meshes are tested (Mesh 2 and 3) at this refinement factor of 2 relative to the starting mesh (Mesh 1), with the difference being Mesh 2 excludes the refinement of the boundary layer elements. This approach makes it possible to determine the refinement effect from the mesh outside the boundary layer and then the effect of the boundary layer refinement separately. The mesh details are summarized in Table 3.3 and the meshes used can be seen in Figure 3.13 to Figure 3.18. The elements inside the rotating domain are now quadrilateral elements instead of triangular for two reasons. The first and most important reason is that in case the boundary layer flow does go beyond the boundary layer elements, quad elements are much better at capturing it. Also, for the same sized elements, quad elements fill the mesh with a smaller number of total elements when compared to triangular ones. One interesting technique used for the generation of the inflation layer can be seen in the trailing edge view of Figure 3.15, where one can see that the trailing edge is rounded and not included in the inflation layer. Typically, the inflation layer encapsulates the entire airfoil profile, however, this technique allows for much higher overall element quality for the boundary layer elements as it avoids stretching the boundary layer elements to have them meet at the tailing edge.

Table 3.3: Details of Each Mesh Used for Mesh Study

	Mesh 1	Mesh 2	Mesh 3
Element Size in Rotating Domain	0.02C	0.01C	0.01C
Element Size in Refinement Region	0.2C	0.1C	0.1C
Number of Nodes on Airfoil	500	500	1000
y^+	~ 1	~ 1	~ 1
First Layer Height in Boundary Layer	7.5×10^{-5} C	7.5×10^{-5} C	7.5×10^{-5} C
Number of Boundary Layer Elements	50	50	85
Boundary Layer Growth Rate	1.1	1.1	1.05
Total Number of Elements	45K	72K	133K

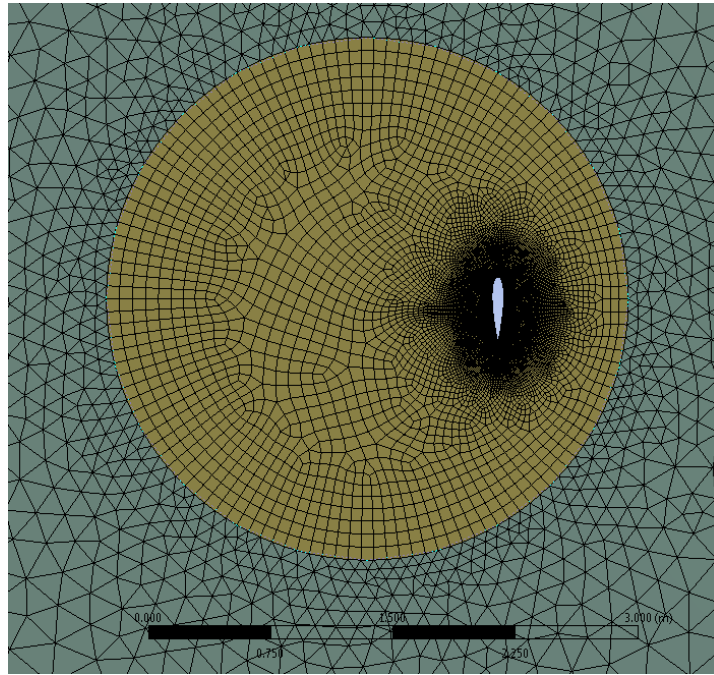


Figure 3.13: Rotating Domain Mesh View for Mesh 1

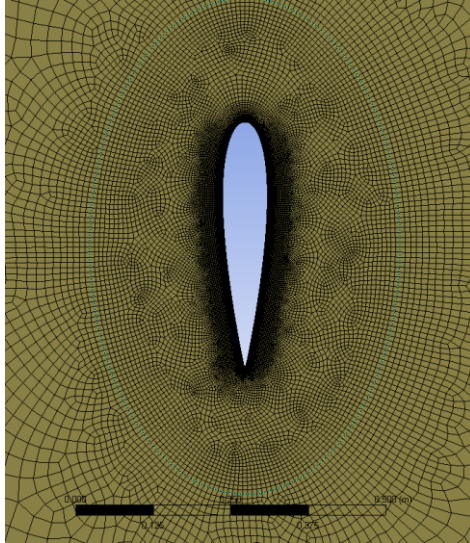


Figure 3.14: Refinement Region Mesh Around Blade for Mesh 1

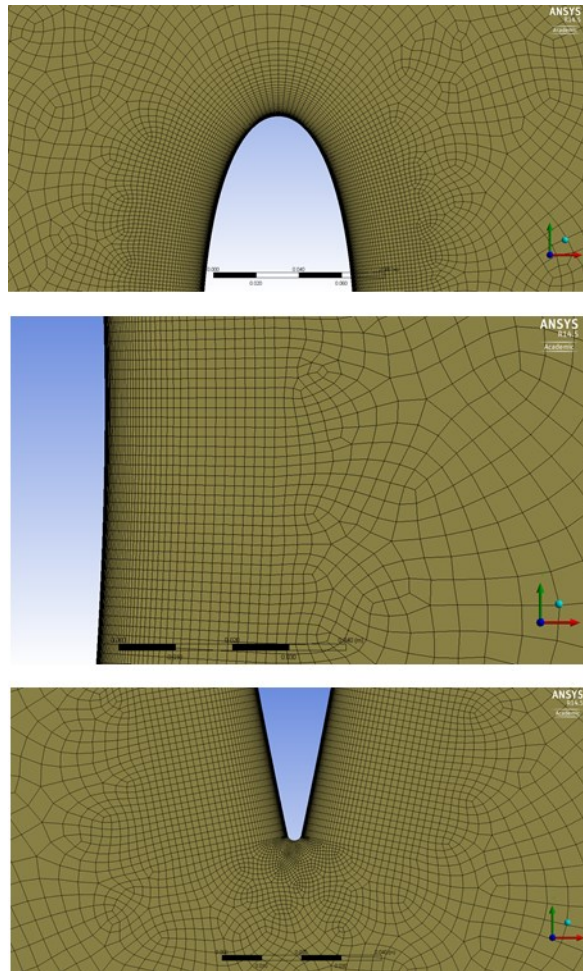


Figure 3.15: Boundary Layer Views for Mesh 1 at Leading Edge (Top), Mid-Chord (Middle), and Trailing Edge (Bottom)

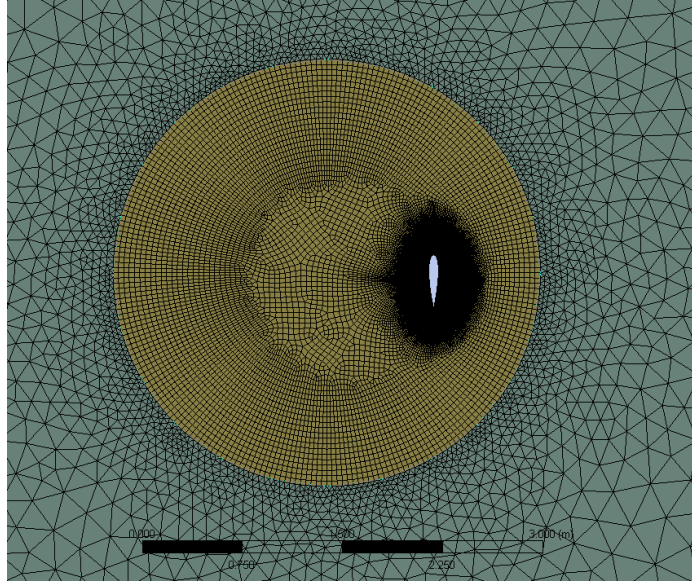


Figure 3.16: Rotating Domain Mesh View for Mesh 2

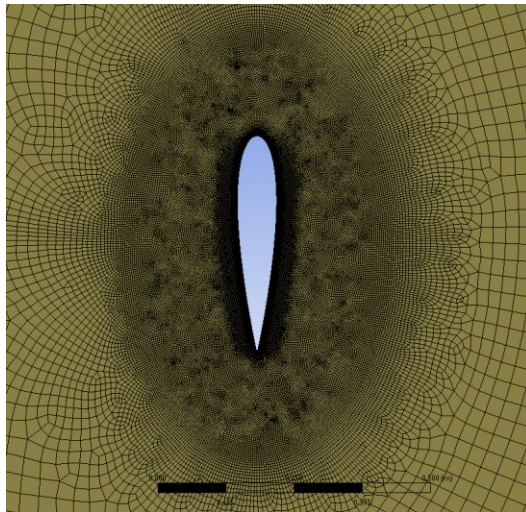


Figure 3.17: Refinement Region Mesh Around Blade for Mesh 2

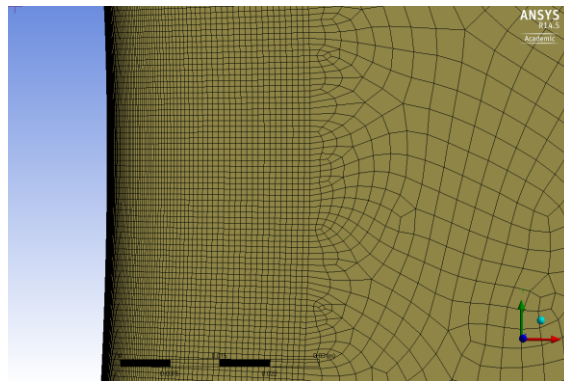


Figure 3.18: Boundary Layer View for Mesh 3

3.5.2 Results and Discussion

All simulations performed in 2D are now run for 15 cycles. Even though at the 10th cycle the cycle to cycle convergence was only less than 1%, the C_P was still dropping. However, after the 15th cycle, the C_P only changed by about 0.01%, thus reaching satisfactory convergence. The convergence of the average C_P per cycle for Mesh 1 can be seen in Figure 3.19. The same trend is noticed for all the other cases. Therefore for 2D simulations, 15 cycles is sufficient and the last three cycles are averaged to be used as point of comparison.

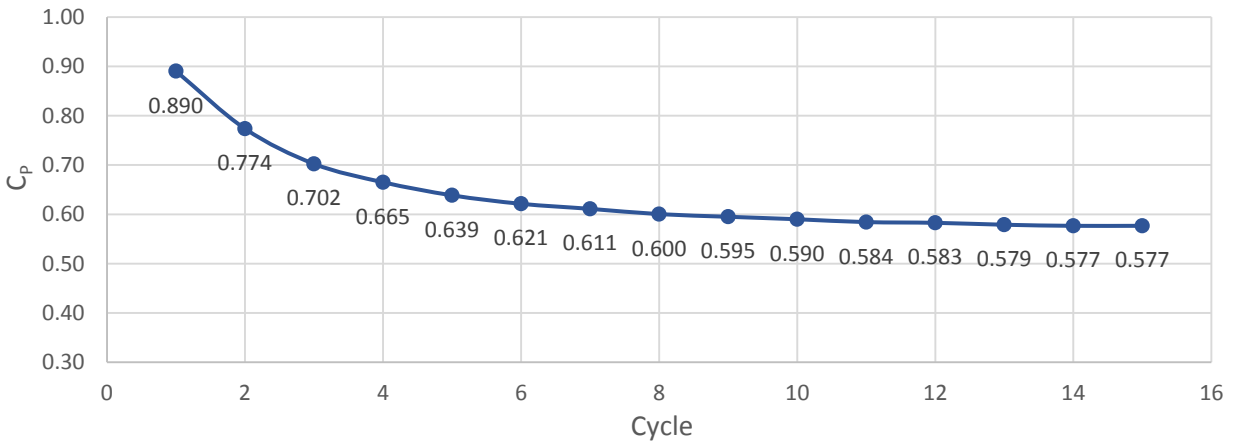


Figure 3.19: Average Cycle C_P Convergence Plot for Mesh 1

Table 3.4 shows the results from the mesh convergence study, where the percent difference from the original mesh (Mesh 1) is presented. Even comparing the coarsest mesh (Mesh 1) with the finest (Mesh 3) with the finer time step, the difference between them is less than 1%. In Figure 3.20, it can be seen that the only small differences that do appear are all near peak power positions, but the same exact behavior is noticed for all of them. Based on this result, the coarsest mesh and time step size are determined to be adequate for further investigation in 2D as well as 3D since the cheapest mesh possible is needed for 3D purposes to reduce its high computational cost.

Table 3.4: Mesh and Time Convergence Study Results

Mesh	Time step per period	Average C_P	C_P % Difference to Mesh 1
1	1136	0.577	-
2	1136	0.580	0.50
3	1136	0.581	0.69
3	2274	0.582	0.86

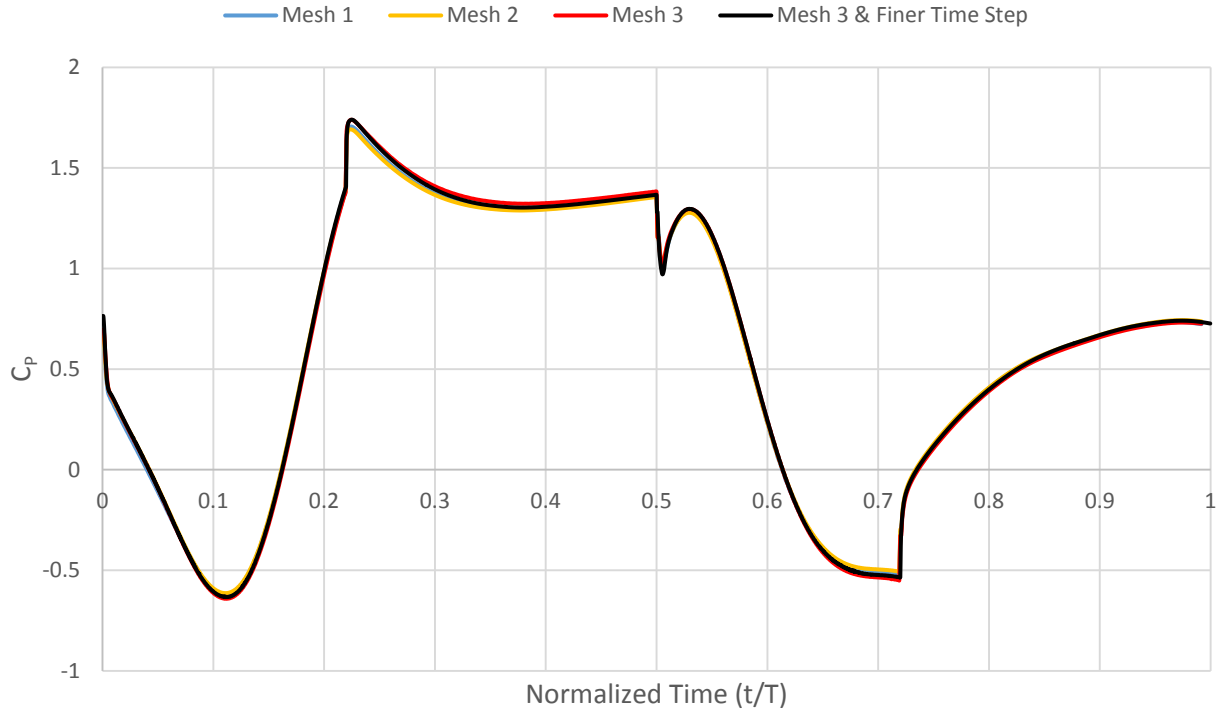


Figure 3.20: Instantaneous C_p versus Normalized Time at 15th Cycle for Mesh and Time Convergence Study Cases

3.6 Turbulence Model Study

In this section, the D-VAWT is simulated using different turbulence models to investigate the accuracy of the results and justify the selection of the turbulence model. Three turbulence models are considered in four cases: the one-equation SA Strain/Vorticity model with $y^+ \sim 1$ and ~ 30 , the two-equation SST $k-\omega$ model with $y^+ \sim 1$, and the four-equation transition SST model with $y^+ \sim 1$. The fastest would be the SA Strain/Vorticity model $y^+ \sim 30$ because it is a lower equation model and the mesh needed for $y^+ \sim 30$ is cheaper. The most expensive would be the transition SST model since it is the highest equation model with a more refined mesh to achieve a $y^+ \sim 1$. The domain and mesh used in this study is the coarsest mesh (Mesh 1) with $\Delta t = T/1136$.

The results for the average C_p for the different cases are shown in Table 3.5 and Figure 3.21. The Transition SST model predicts the highest C_p value, while the SA Strain/Vorticity for $y^+ \sim 30$ predicts the lowest. The biggest difference is noticed between the cases using the mesh of $y^+ \sim 1$ and $y^+ \sim 30$. Though the trends shown in Figure 3.21 for all cases are similar, the SA Strain/Vorticity with $y^+ \sim 30$ under predicts the upstream translational region and the following rotating region or at the normalized times between 0.22 and 0.72. It can be seen that the SA

Strain/Vorticity model at $y^+ \sim 30$ consistently under predicts the C_P value in that region, while for the other models at $y^+ \sim 1$ show better consistency in value throughout the cycle. The results obtained here are also supported by [31], in which they showed at high TSR, the choice of turbulence model with the same y^+ has little effect on the results.

Table 3.5: Results for the Turbulence Model Study Using Mesh 1 at TSR = 4.5

Turbulence Model	y^+	Average C_P	C_P % Difference to Case 1
SST k- ω	1	0.577	-
Transition SST	1	0.580	0.45
SA Strain	1	0.553	4.32
SA Strain	30	0.491	17.50

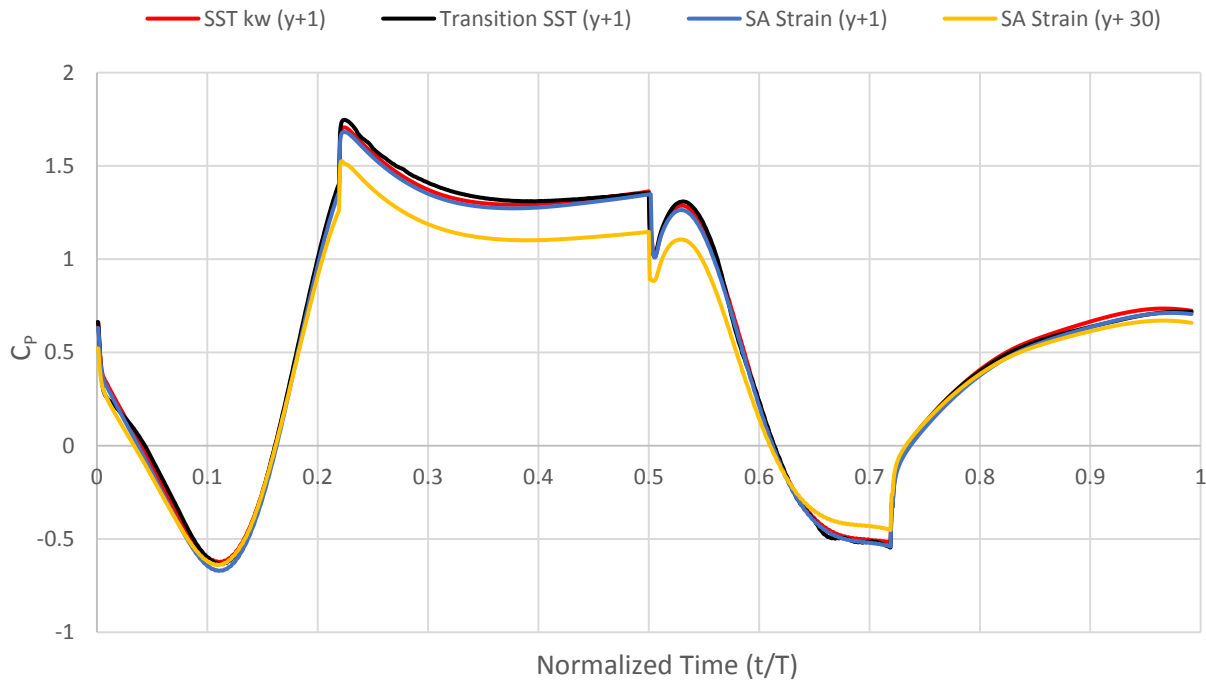


Figure 3.21: Instantaneous C_P Plots of the 15th cycle for the Turbulence Model Study Using Mesh 1 at TSR=4.5

3.7 Airfoil Validation with Experimental Results

Using the presented methodology, an experimental case is simulated and the results are compared with their respective experimental values. The case is that of a 2D simulation of a static airfoil. This case was specifically chosen as it closely matched the flow regime of the D-VAWT while no data was available for a Darrieus type turbine that even remotely resembled the D-VAWT's flow conditions and blade profile (NACA 0018).

Using the same methodology to generate the mesh, a NACA 0018 airfoil is simulated with an identical numerical setup as the D-VAWT. The only difference from the D-VAWT case is the inlet boundary condition values for the turbulent intensity, which were matched with the experimental setup to ensure a proper comparison. The Reynolds number is 500,000, which is in the same range as what the D-VAWT's blade experiences in the upstream translational region. The results are validated with the experimental case performed by Timmer [63].

The purpose of these simulations is to validate the choice of turbulence model and accuracy of the CFD setup with existing experimental results. The same four cases from the turbulence model study are repeated here, which are the SA Strain/Vorticity model using $y^+ \sim 30$ and $y^+ \sim 1$, the SST $k-\omega$ and transition SST models with $y^+ \sim 1$.

3.7.1 Domain and Mesh

Figure 3.22 shows the overview of the domain and mesh used to replicate the experimental case. The domain is a C-mesh type, which is commonly used for the simulation of static airfoils. Figure 3.23 shows a close view of the mesh near the blade for the cases of $y^+ \sim 30$ and $y^+ \sim 1$. The meshes were generated with the same element sizes as for the case of the D-VAWT.

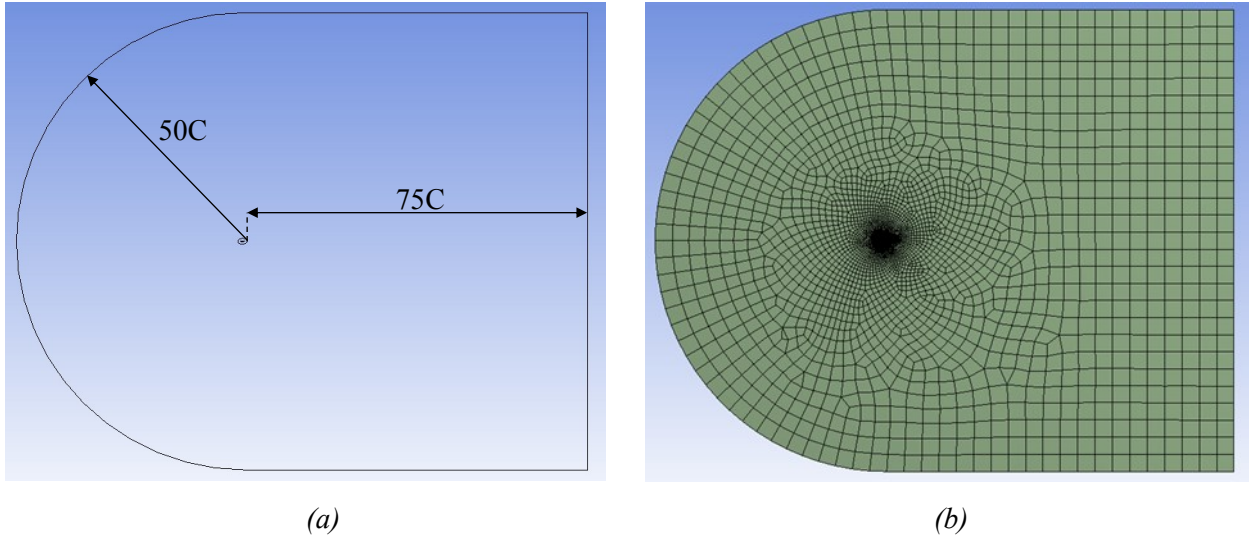


Figure 3.22: Overview of (a) Domain (b) Mesh, for the Experimental Case Simulation

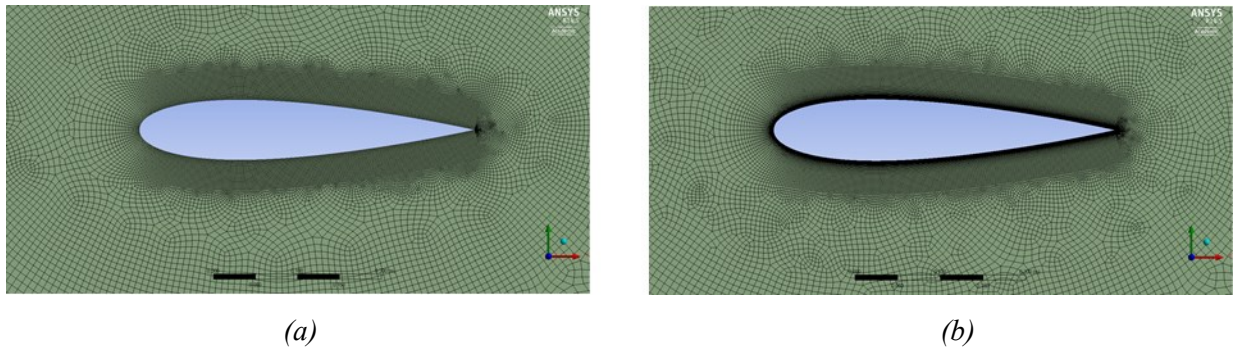


Figure 3.23: Mesh Near Blade for (a) $y^+ \sim 30$ (b) $y^+ \sim 1$

3.7.2 Results and Discussion

Figure 3.24 to Figure 3.27 show the results for the Coefficient of Lift (C_L) and Coefficient of Drag (C_D) for all simulations cases as well as the experimental values. Figure 3.24 shows that the transition SST model predicts the most accurate results as it captures the experimental curve the closest. The SST $k-\omega$ model is the second most accurate model tested, with the advantage of being computational cheaper than the Transition SST. The SA Strain/Vorticity model with $y^+ \sim 1$ over predicts drag, as seen in Figure 3.25, while the SA Strain/Vorticity model with $y^+ \sim 30$ greatly over predicts drag and shows premature stall behavior that is not seen with any of the other models at $y^+ \sim 1$. This further explains the under prediction of the SA Strain/Vorticity model with $y^+ \sim 30$ in the results of Figure 3.21, where the blade experienced higher drag and lower lift than it should have. This finding further supports the results of the turbulence model study.

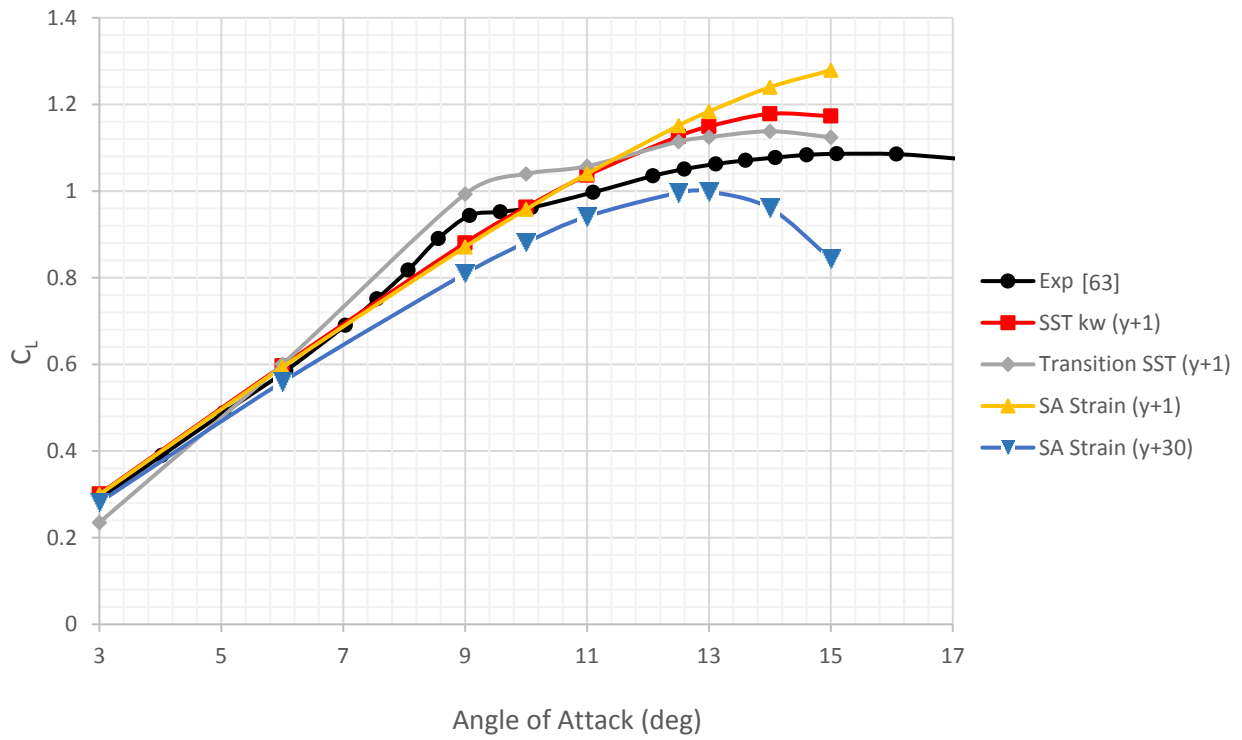


Figure 3.24: Coefficient of Lift vs Angle of Attack

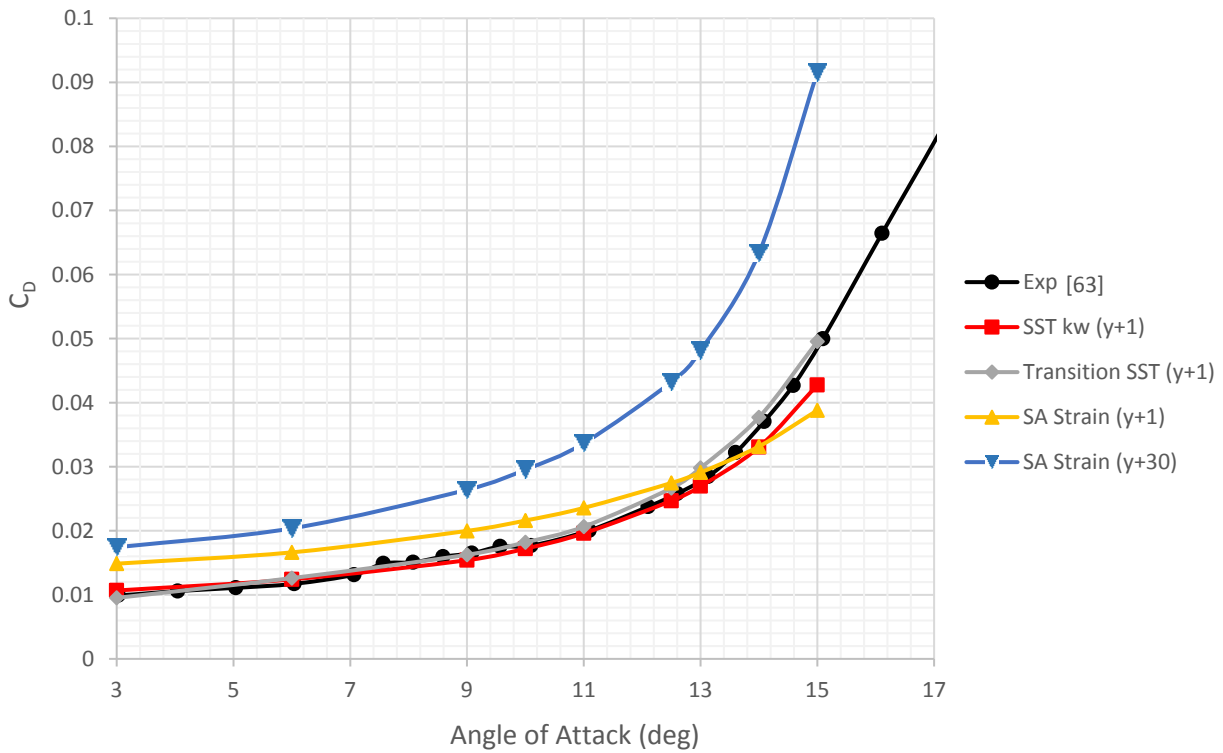


Figure 3.25: Coefficient of Drag vs Angle of Attack

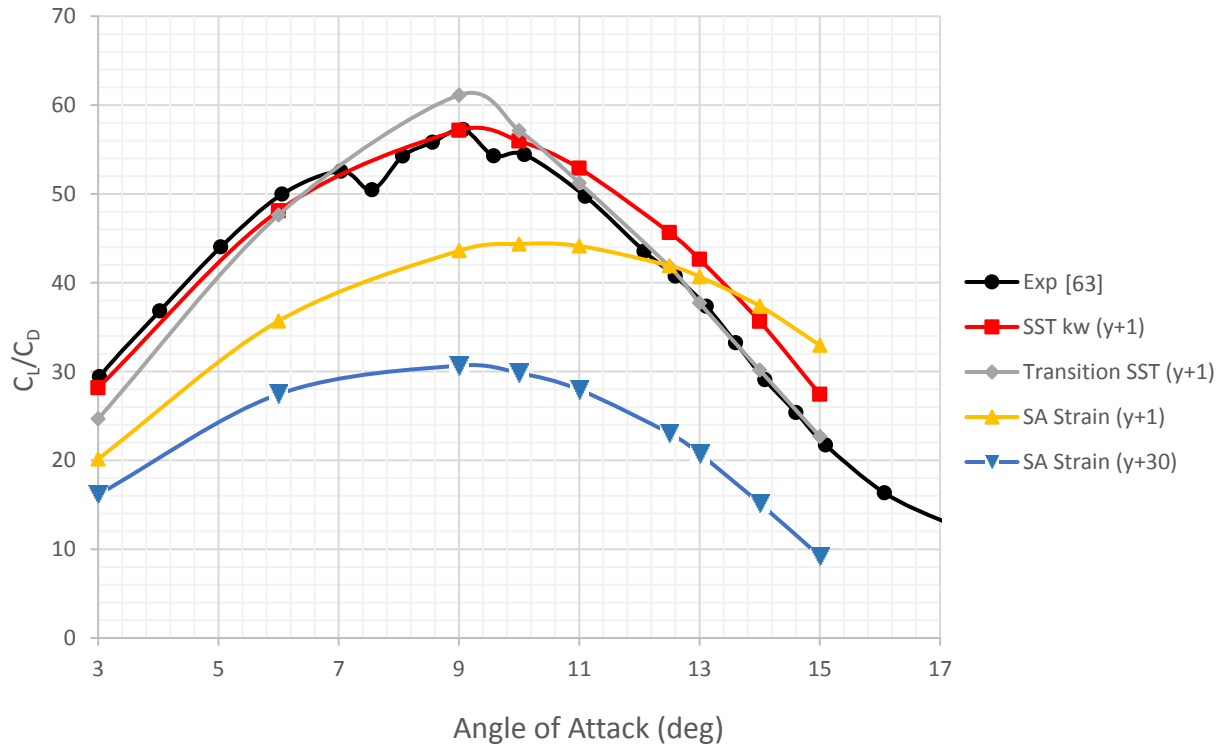


Figure 3.26: Ratio of Coefficient of Lift to Coefficient of Drag vs Angle of Attack

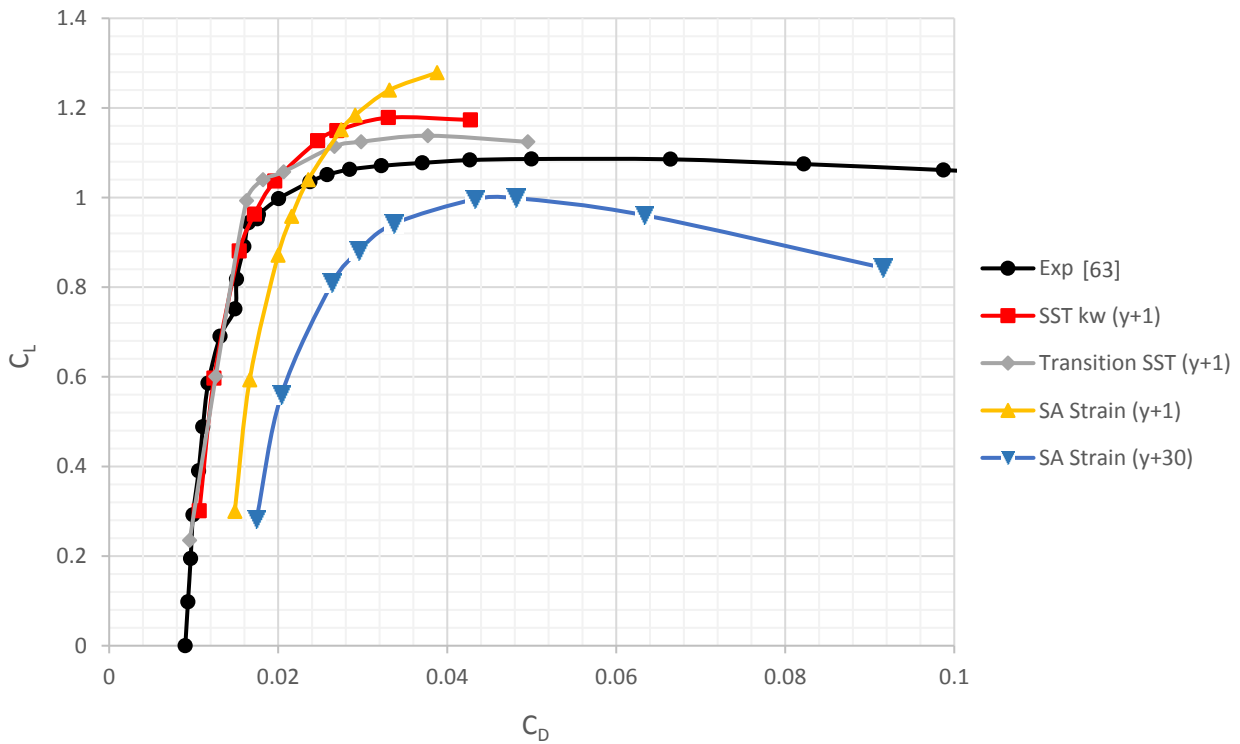


Figure 3.27: Coefficient of Lift vs Coefficient of Drag

Table 3.6 shows the percent error for all data points simulated for all turbulence models with the values obtained from the experimental data. The interesting part to note is the average error for the ratio of C_L to C_D for the range of angle of attacks that the D-VAWT experiences (from 0° to 12.5°) at $TSR = 4.5$ for the cases of SA Strain/Vorticity model using a $y^+ \sim 30$ and $y^+ \sim 1$, the SST k- ω and transition SST models with a $y^+ \sim 1$ are 44.9%, 18.6%, 2% and 0.6%, respectively. These values confirm that the transition SST model provides the most accurate solution, closely followed by the SST k- ω model, while the SA Strain/Vorticity model provides the least accurate results for both y^+ cases. The ratio of C_L to C_D is directly related to the predicted output power of the turbine. Seeing that the SA Strain/Vorticity with $y^+ \sim 30$ consistently under predicts that said ratio, this explains the under prediction in power for the case of the D-VAWT.

Table 3.6: Percent Error for Airfoil Case Study (Positive is Over Prediction and Negative is Under Prediction)

Angle of Attack	% Error with Experimental Results											
	SST kw ($y^+ \sim 1$)			Transition SST ($y^+ \sim 1$)			SA Strain ($y^+ \sim 1$)			SA Strain ($y^+ \sim 30$)		
	C_D	C_L	C_L/C_D	C_D	C_L	C_L/C_D	C_D	C_L	C_L/C_D	C_D	C_L	C_L/C_D
3	7.68	3.85	-3.55	-3.96	-18.9	-15.5	49.91	3.44	-31.00	75.78	-2.83	-44.72
6	6.12	2.93	-3.01	7.84	3.58	-3.95	42.21	2.34	-28.04	74.24	-3.55	-44.65
9	-6.06	-5.93	0.13	-0.90	6.11	7.07	21.84	-6.92	-23.61	60.98	-13.51	-46.27
10	-2.49	0.28	2.84	3.11	8.27	5.01	22.35	-0.24	-18.46	67.42	-8.22	-45.18
11	-1.15	4.30	5.51	4.08	6.41	2.24	18.84	4.65	-11.94	69.80	-5.28	-44.22
12.5	-2.82	7.50	10.62	4.98	6.34	1.29	8.15	9.86	1.57	70.29	-4.92	-44.17
13	-3.05	8.42	11.83	7.24	6.08	-1.08	4.67	11.67	6.69	73.08	-5.78	-45.57
14	-8.63	9.49	19.82	4.24	5.74	1.44	-8.31	15.21	25.66	75.09	-10.75	-49.03
15	-12.0	8.07	22.83	1.93	3.57	1.61	-20.17	17.80	47.57	88.41	-22.33	-58.78
Avg.	-2.49	4.32	7.45	3.17	3.02	-0.21	15.50	6.42	-3.51	72.79	-8.57	-46.95
Avg. (up to 12.5°)	0.21	2.15	2.09	2.53	1.97	-0.65	27.22	2.19	-18.58	69.75	-6.38	-44.87

3.8 Summary and Conclusions

The validation for the D-VAWT included the investigation of the domain size, motion prescription methods, mesh and time convergence, and turbulence model study. The setup was also validated with an airfoil case study with experimental data. The validation allowed us to find the smallest domain, mesh and time step needed to make this setup the most conservative and cheapest while still retaining satisfactory accuracy. Having the cheapest possible setup will greatly help in reducing the cost of 3D simulations as they tend to be quite expensive.

The theoretical calculation of the C_P , shown in section 2.6, for the upstream translational region predicted a value of 1.41. This calculation was done for an airfoil with an angle of attack of 12.5° and a blade Reynolds number of 500,000, which are the conditions the D-VAWT blade during the translational section. The average value of C_P in the upstream translational region using the SST $k-\omega$ model is 1.38. Comparing the theoretical and predicted CFD values, there is only a difference of about 2%, which further supports the analysis and the selected methodology.

Based on the turbulence model study and the validation with experimental results, the SST $k-\omega$ model at $y^+ \sim 1$ and the SA Strain/Vorticity model at $y^+ \sim 30$ provide an upper and lower bound estimate for the C_P , where the lower bound will represent a more conservative estimate for the D-VAWT's performance. The upper and lower bounds can be clearly seen in Figure 3.26. The reason the SST $k-\omega$ model was chosen over the other two models at $y^+ \sim 1$ is that it is faster than the Transition SST model and it is more accurate at resolving the boundary layer flow in the near-wall region than the SA Strain/Vorticity model. The value predicted from the SST $k-\omega$ model is expected to represent actuality more closely than from the lower bound estimate because it is a higher equation model capable of accurately resolving the flow in the near-wall region. For airfoil and turbine simulations where there is no shedding of vortices, accurately capturing the boundary layer flow is of the utmost importance, which is exactly what the SST $k-\omega$ model is good at resolving.

CHAPTER 4: 3D INVESTIGATION

In this chapter, 3D simulation of the D-VAWT at $TSR = 4.5$ with the same geometrical parameters as presented earlier will be performed based on the methodology developed in the previous chapter. The Aspect Ratio (AR) of 5 and 15 will be investigated using the SA Strain ($y^+ \sim 30$) and SST $k-\omega$ ($y^+ \sim 1$) turbulence models to provide us with an upper and lower bound estimate of the C_p .

4.1 Domain

The domain used for the simulation with $AR = 5$ is shown in Figure 4.1. Further details are included in Table 4.1 for both domains of $AR = 5$ and 15. It should be noted that only half of the blade is simulated by making use of a symmetry plane boundary condition. This essentially allows the domain to be cut by half, which significantly reduces the computational cost.

Type 2 motion is used for all 3D simulations since Fluent encountered many problems with the deforming mesh of type 1 motion. Based on the comparison of motion types, the results should be identical for both motions. The coordinate system is shown in Figure 4.1, where the incoming wind is coming in the positive X-direction.

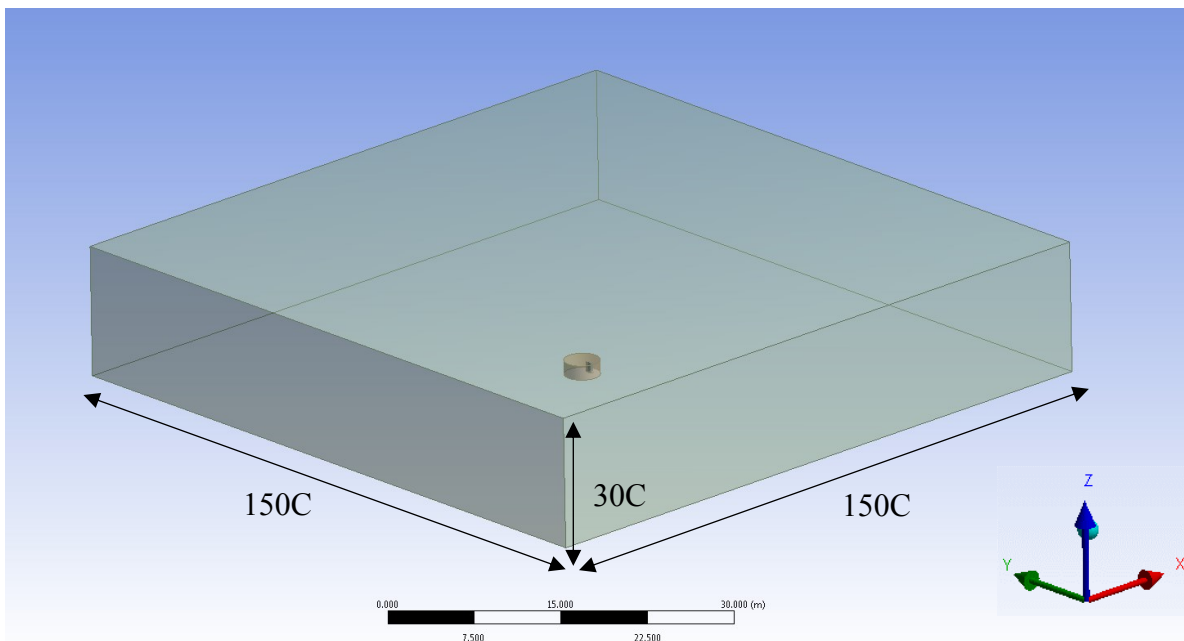


Figure 4.1: 3D Domain for D-VAWT with $AR=5$

Table 4.1: 3D Domain Characteristics

3D Domain Characteristics		
	Aspect Ratio = 5	Aspect Ratio =15
Outer Domain Size	150C × 150C × 30C	150C × 150C × 45C
Simulated Blade Height, h/2	2.5C	7.5C
Rotating Domain Diameter	2D	2D
Rotating Domain Depth	3.25C	8.25C

4.2 Mesh

Two turbulence models are tested, the SA Strain/Vorticity and SST $k-\omega$, with different y^+ strategies for each. There are a total of four cases performed, comprising of two aspect ratios with two turbulence models. The details of the mesh used are shown Table 4.2, which are based on the 2D mesh study. The mesh for the AR = 5 with the SA Strain/Vorticity model is shown in Figure 4.2 to Figure 4.5, while the one used for AR = 5 with the SST $k-\omega$ model is shown in Figure 4.6 to Figure 4.8. The meshes used for each turbulence model are nearly identical; the only difference is the number of elements in the span wise direction for the different aspect ratios used. Elements across the rotating interface are matched in size to reduce interpolation errors across the interface. The elements in the refinement region around the blade are hexahedron elements formed from quadrilateral elements that have been swept in the span-wise direction. It should be noted that the elements swept have a bias towards the blade tip, meaning the elements near the blade tip are smaller than the ones near the blade center (at the symmetry plane). The purpose of the bias is to better capture the flow and pressure drop near the blade end from the tip vortex. All the elements outside of the refinement regions are tetrahedrons.

Table 4.2: 3D Meshes Details

Case	Aspect Ratio = 5		Aspect Ratio =15	
	SA Strain	SST k- ω	SA Strain	SST k- ω
Element size in rotating domain	0.2C	0.2C	0.2C	0.2C
Element size in refinement region	0.02C	0.02C	0.02C	0.02C
Number of nodes on airfoil	250	500	250	500
Number of span wise elements	80	80	200	200
y^+	~ 30	~ 1	~ 30	~ 1
First layer height in boundary layer	$2.5 \times 10^{-3} C$	$7.5 \times 10^{-5} C$	$2.5 \times 10^{-3} C$	$7.5 \times 10^{-5} C$
Number of boundary layer elements	15	50	15	50
Boundary layer growth rate	1.1	1.1	1.1	1.1
Total number of elements	2.9 Million	4 Million	7.5 Million	10 Million

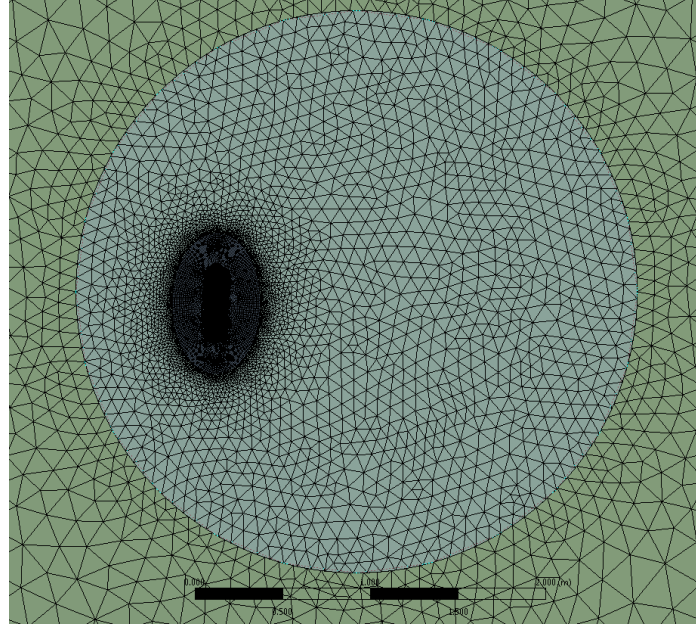


Figure 4.2: Rotating Domain Mesh at Symmetry Plane for AR=5 and $y^+ \sim 30$

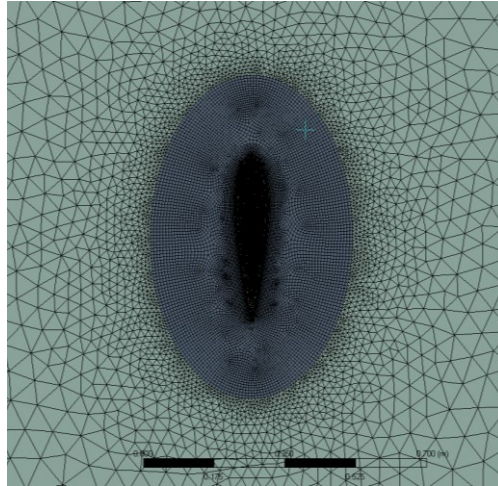


Figure 4.3: Refinement Region Mesh at Symmetry Plane for $AR=5$ and $y^+ \sim 30$

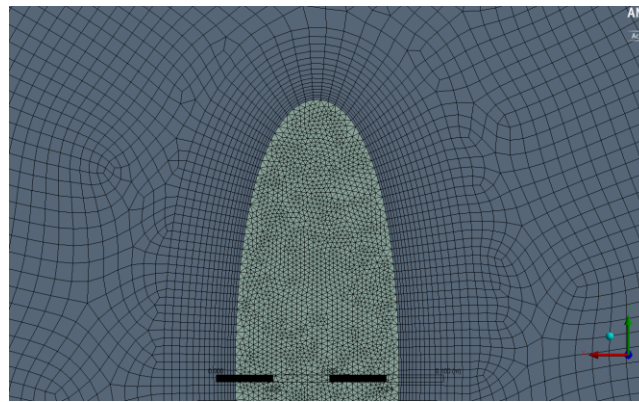


Figure 4.4: Boundary Layer Mesh View at Symmetry Plane for $AR=5$ and $y^+ \sim 30$

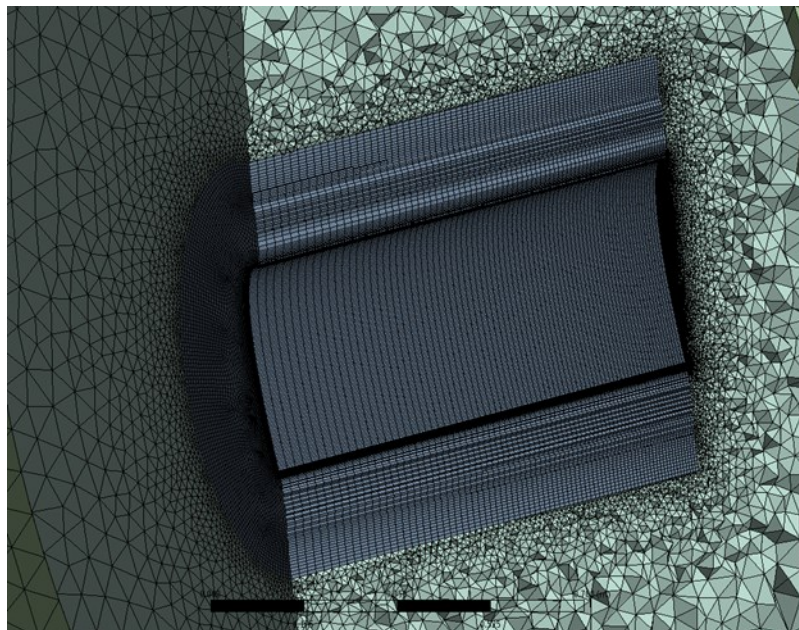


Figure 4.5: Cross Section of Mesh Around the Blade $AR=5$ and $y^+ \sim 30$

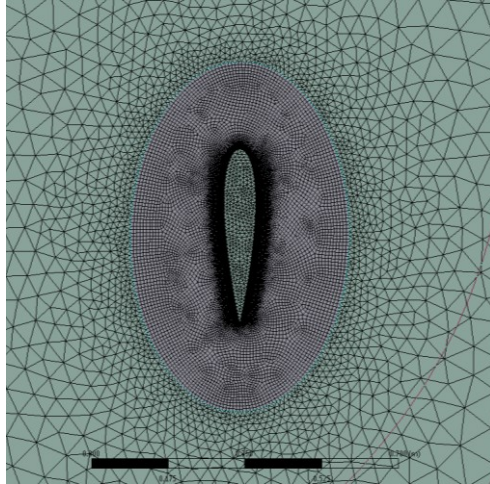


Figure 4.6: Refinement Region Mesh at Symmetry Plane for $AR=5$ and $y^+ \sim 1$

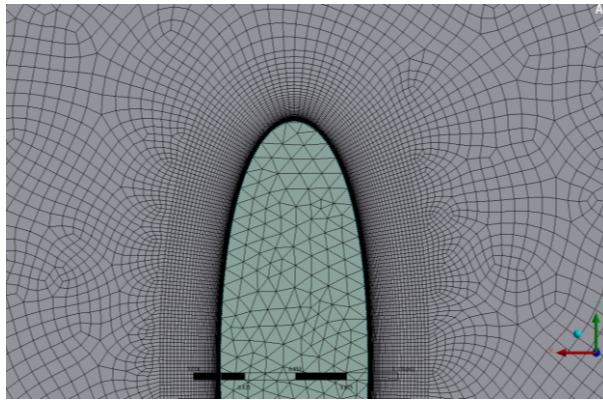


Figure 4.7: Boundary Layer Mesh View at Symmetry Plane for $AR=5$ and $y^+ \sim 1$

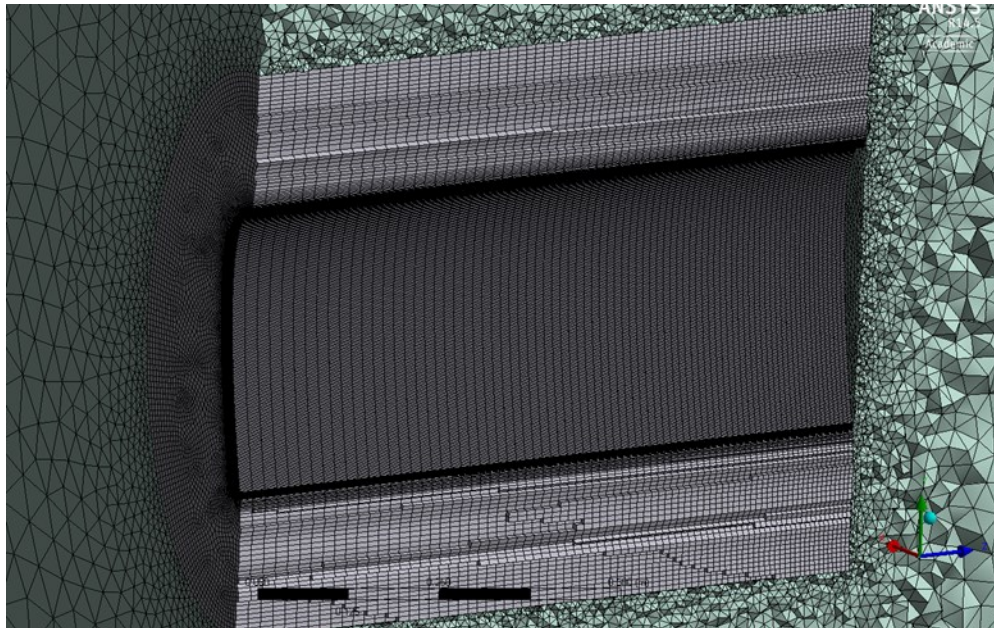


Figure 4.8: Cross Section of Mesh Around the Blade for $AR=5$ and $y^+ \sim 1$

4.3 Numerical Setup

The SIMPLE algorithm is selected for the pressure-velocity coupling. For the spatial discretization, second order schemes are used for the pressure, momentum and turbulent viscosity calculation. First order implicit is still used for the transient formulation due to the use of the dynamic mesh capabilities. All simulations are performed with an absolute convergence criterion of 10^{-3} for the continuity, velocity components and all turbulent properties. The time step size is $\Delta t = 0.5585\text{ms}$ or about one thousandth of a period ($T/1136$). The SA Strain/Vorticity based production model and the SST $k-\omega$ model with low Reynolds number correction are used for turbulence modelling.

The boundary conditions are shown in Figure 4.9, where constant and uniform velocity inlets are defined everywhere, except for the bottom plane which has a symmetry condition and the right most boundary is defined as a pressure outlet. The velocity of incoming wind is 4 m/s with a turbulent intensity of 1% and a turbulent viscosity ratio of $\frac{\nu_t}{\nu} = 5$. The turbulent intensity is reduced from 5% to 1% from the 2D to 3D simulations to speed up the convergence of the simulation. This change would have marginal effect on the results as both turbulence intensities were tested and compared in 2D. As for the blade boundary condition, a no-slip condition is applied.

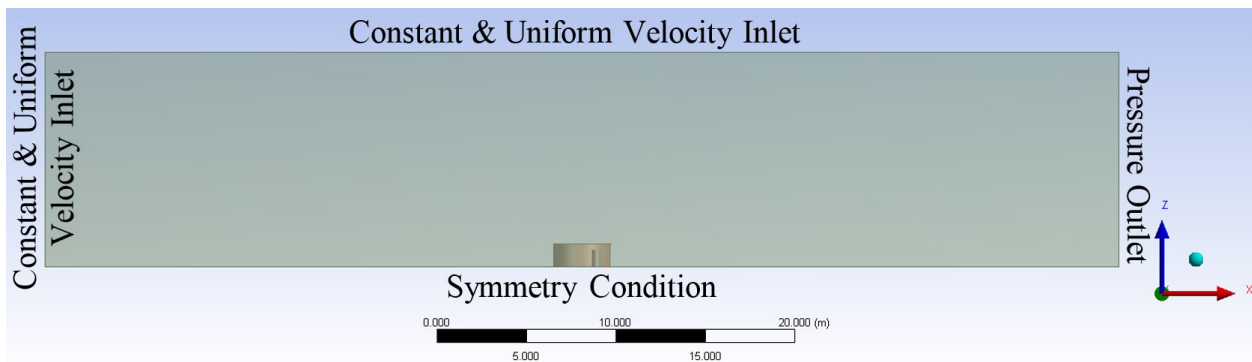


Figure 4.9: Boundary Conditions for 3D Domains

4.4 Results and Discussion

All 3D simulations of the D-VAWT at $\text{TSR} = 4.5$ were run for 10 and 12 cycles for the aspect ratio of 5 and for 15, respectively. The C_p cycle convergence can be seen in Figure 4.10, where it can be noticed that the simulations with $\text{AR} = 5$ converge faster than the ones with $\text{AR} = 15$. The cycle

to cycle convergence criterion used for all 3D simulations is 0.2%, since matching that of 2D's of 0.01% was difficult to reach in 3D. Table 4.3 presents the summary of the averaged C_P in the last 3 cycles and the ratio of 3D to 2D C_P values for each case respectively. It can be seen that for the AR of 5, only about 40-44% of the power in 2D is captured, while for an AR of 15, this increases to about 70%. The 3D to 2D ratio value for the AR =15 case is also supported by [31], where a ratio of 69% is obtained for the same AR. It is well known that as the AR of airfoil blades is increased, the 3D performance approaches that of 2D. For a short AR, the 3D losses, especially because of the formation of a wing tip vortex, dominate and a larger portion of the blade sees a large decrease in performance. The formation of the wing tip vortex leads to a decrease in performance as a result of the pressure drop on the blade surface when approaching the blade tip. The wing tip vortex allows the flow to “leak” over the blade tip and reduces the built up pressure from the airfoil profile, which in turn reduces the lift of the blade portion affected by it.

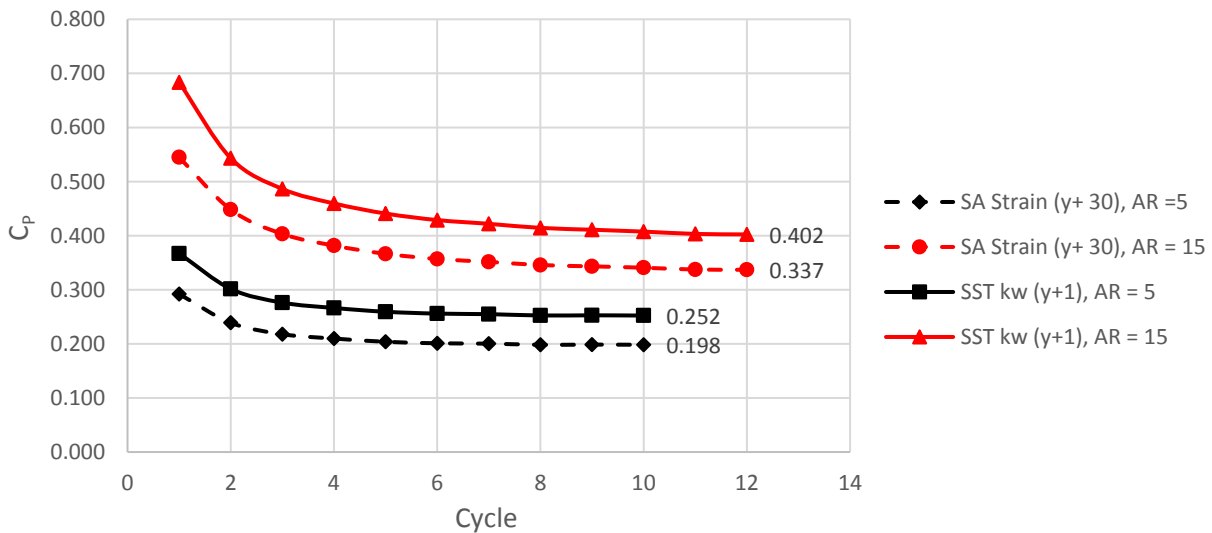


Figure 4.10: Average C_P per Cycle Convergence for 3D Simulations

Table 4.3: C_P Results Summary for 3D Simulations

Aspect Ratio	Turbulence Model	Average C_P	3D/2D % Ratio
5	SA Strain ($y^+ \sim 30$)	0.198	40.37
	SST k- ω ($y^+ \sim 1$)	0.253	43.73
15	SA Strain ($y^+ \sim 30$)	0.338	68.86
	SST k- ω ($y^+ \sim 1$)	0.404	70.03

The instantaneous C_P curves are shown in Figure 4.11 for all 3D cases. For the same AR, there is a gap in performance between the SA Strain/Vorticity model and SST $k-\omega$ model, where the SA Strain/Vorticity model with $y^+ \sim 30$ still under predicts the C_P values, most noticeably in the upstream translational region and the following rotational region. The C_P trend between the blade of AR of 5 and 15 are similar throughout most of the cycle, except for the fact that the blade of AR of 15 produces more power as expected. An interesting behavior between the two is noticed in the downstream portion of the blade path, especially in the translational region. For the AR of 15, C_P behavior is very similar to that of the 2D one, but for the AR of 5, looking at the normalized time from 0.72, the C_P is initially slightly higher than for the AR of 15, but after $t/T=0.88$, a dip in power occurs that is not seen in either the 2D or 3D with AR=15 cases.

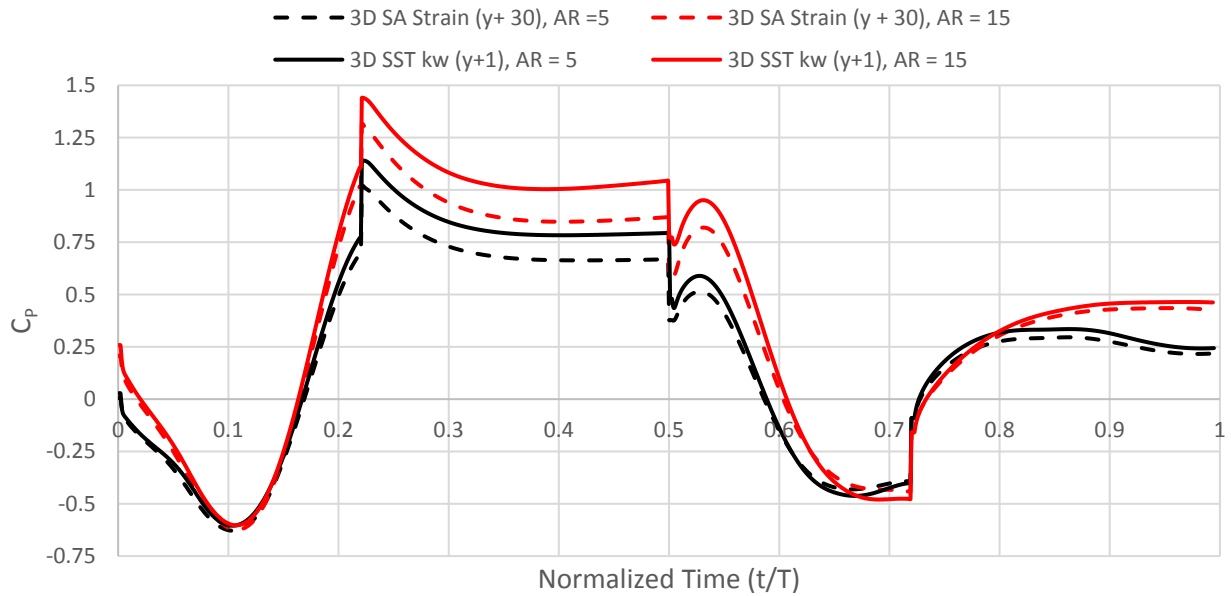


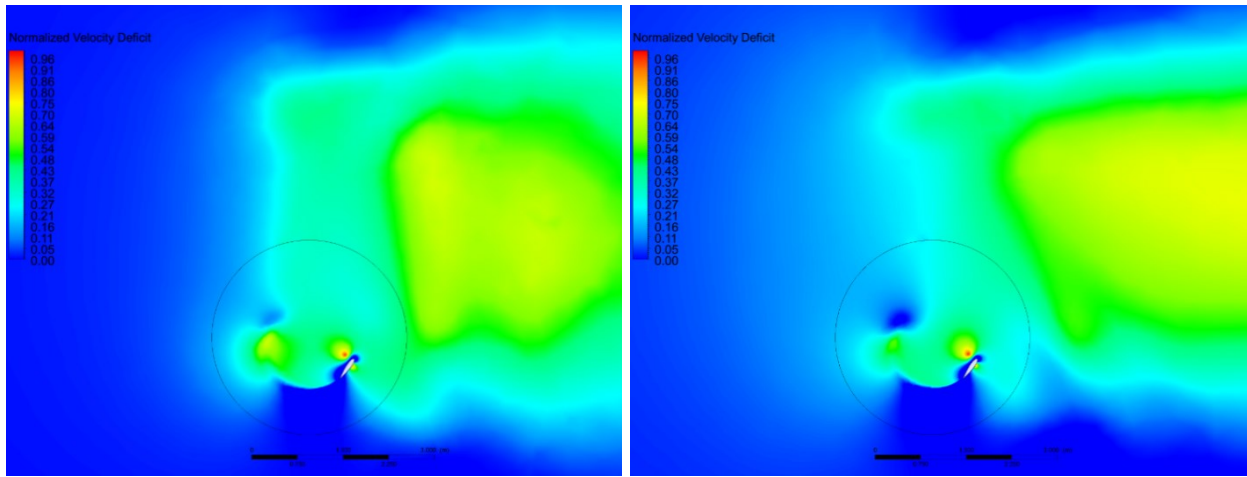
Figure 4.11: Instantaneous C_P Plots of the Last Cycle for 3D Simulations

In Figure 4.12, the normalized velocity deficit ($\frac{U_\infty - U}{U_\infty}$) is shown at a cross sectional plane that is half a chord away from the symmetry plane as it is preferable not to visualize the flow on the symmetry plane. The normalized velocity deficit shows how much velocity is either reduced from losses or extracted by the turbine. Figure 4.12 (a) and (b) are for the SA Strain/Vorticity model of AR = 5 and 15, respectively. It should be noted that the blade tip effect is stronger for the case of AR = 5 at this plane because this plane is only two chords away from the tip while for the AR = 15, it is 7 chords away. A plane that is two chords away from the blade tip was visualized for the

case of $AR = 15$, it was then noticed that the behavior of the flow highly resembled that of the $AR = 5$ shown here. This means that at a distance of two chords from the blade tip for either $AR = 5$ or 15 cases, the performance of the blade is highly affected and reduced by the presence of the wing tip vortex, while at 7 chords away for $AR = 15$, this effect dissipates and the performance approaches that of 2D. To better grasp the effect of AR on the blade performance, Figure 4.13 shows the static pressure contour on the blade surface during the upstream translational region for the SST $k-\omega$ model for both $AR = 5$ and 15 . One can see the pressure drop starting from around one chord's length from the blade tip and because about the same length of the blade is affected for both AR s, it means that the blade with $AR = 5$ has a larger portion affected.

As shown in Figure 4.12, after the upstream pass of the blade, about 35-40% of the free stream velocity is extracted or lost, while after the downstream pass, the free stream velocity drops to 75-80% of its initial value. This means that with a single turbine, it is possible to extract about 75% of the incoming wind's energy from the two passes of the blade in the translational region. This can also be supported from the C_P values seen in those regions. However, with such a strong velocity deficit, the wake of this turbine will be very strong and will take some time to recover and return to its original free stream velocity. This means that if another turbine were to be placed downstream of it, it would have to be significantly far away from the first.

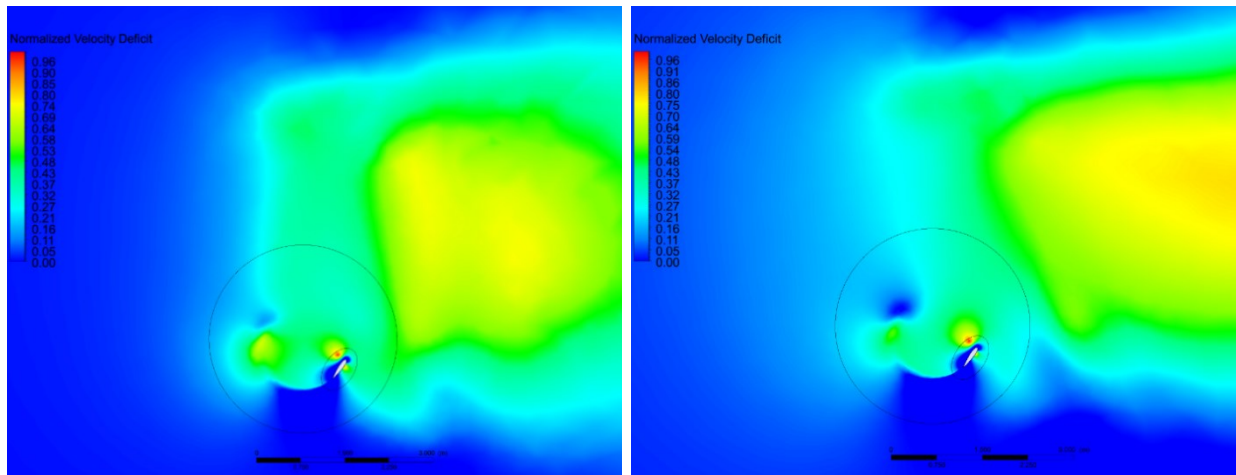
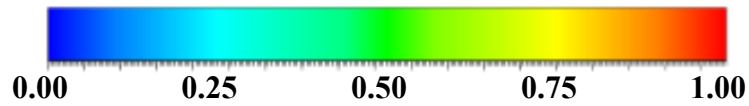
Another detail to note from Figure 4.12 is that for the same AR in Figure 4.12 (a) and (c), the flow for the SA Strain/Vorticity and the SST $k-\omega$ models have similar wake structure, but for the SST $k-\omega$ model, the velocity deficit in the wake is higher, which can be explained by the higher power extraction seen in the C_P Curve. This can also be seen again in Figure 4.12 (b) and (d). The difference between the models can be seen in the size of the boundary layer in Figure 4.14, where the turbulent viscosity ratio ($\frac{\nu_t}{\nu}$) is shown at the same cross sectional plane as before, but at the normalized time $t/T = 0.33$, which is approximately midway in the translational region. In Figure 4.14, the AR does not seem to affect the size of the boundary layer, but the choice of y^+ between the two models does indeed affect it, resulting in a boundary layer for the $y^+ \sim 30$ to be almost twice as thick as the one for $y^+ \sim 1$. The recirculation zone on the suction side to the airfoil (right side of blades in Figure 4.14) is also much larger for the cases with $y^+ \sim 30$, leading to lower lift and higher drag as seen before in the results of the experimental validation case of a static airfoil, which explains the lower extracted power in this region.



(a)

(b)

Normalized Velocity Deficit, $\frac{U_\infty - U}{U_\infty}$



(c)

(d)

Figure 4.12: Normalized Velocity Deficit ($\frac{U_\infty - U}{U_\infty}$) Plots on a Plane of Half a Chord Away in the Span-Wise Direction from the Symmetry Plane at $t/T=0.68$ for Cases (a) SA Strain/Vorticity ($y^+ \sim 30$) with $AR = 5$, (b) SA Strain/Vorticity ($y^+ \sim 30$) with $AR = 15$, (c) SST $k-\omega$ ($y^+ \sim 1$) with $AR = 5$, and (d) SST $k-\omega$ ($y^+ \sim 1$) with $AR = 15$

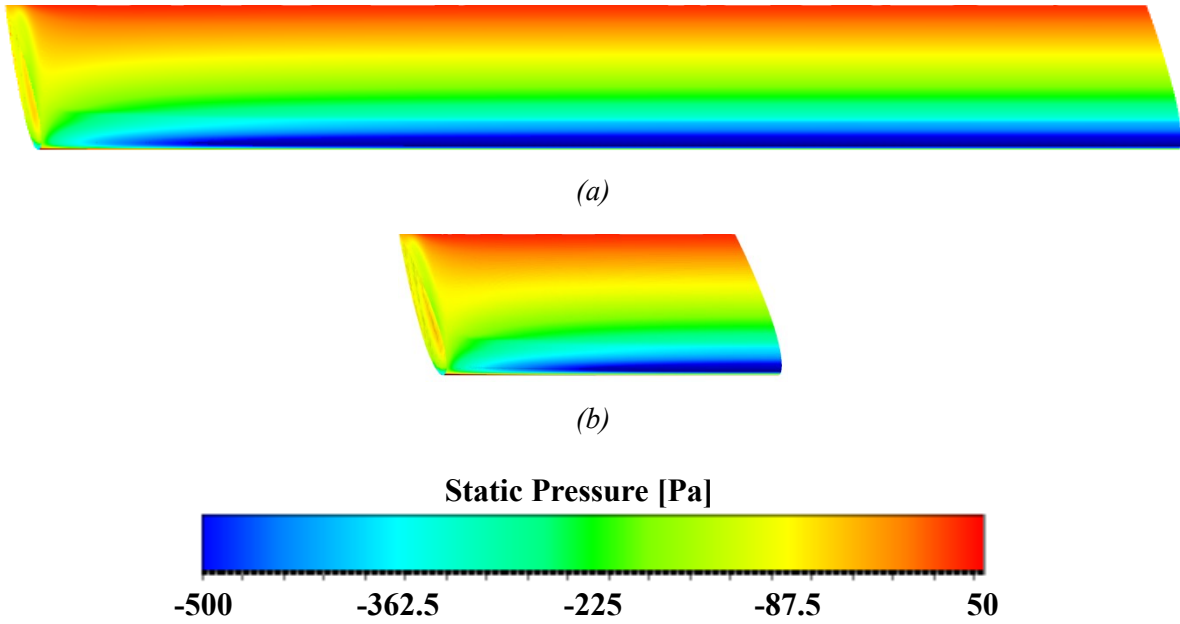


Figure 4.13: Static Pressure Contour on Half of the Blade Surface for SST $k-\omega$ ($y^+ \sim 1$) Model at $t/T=0.33$ for (a) $AR = 15$ (b) $AR = 5$

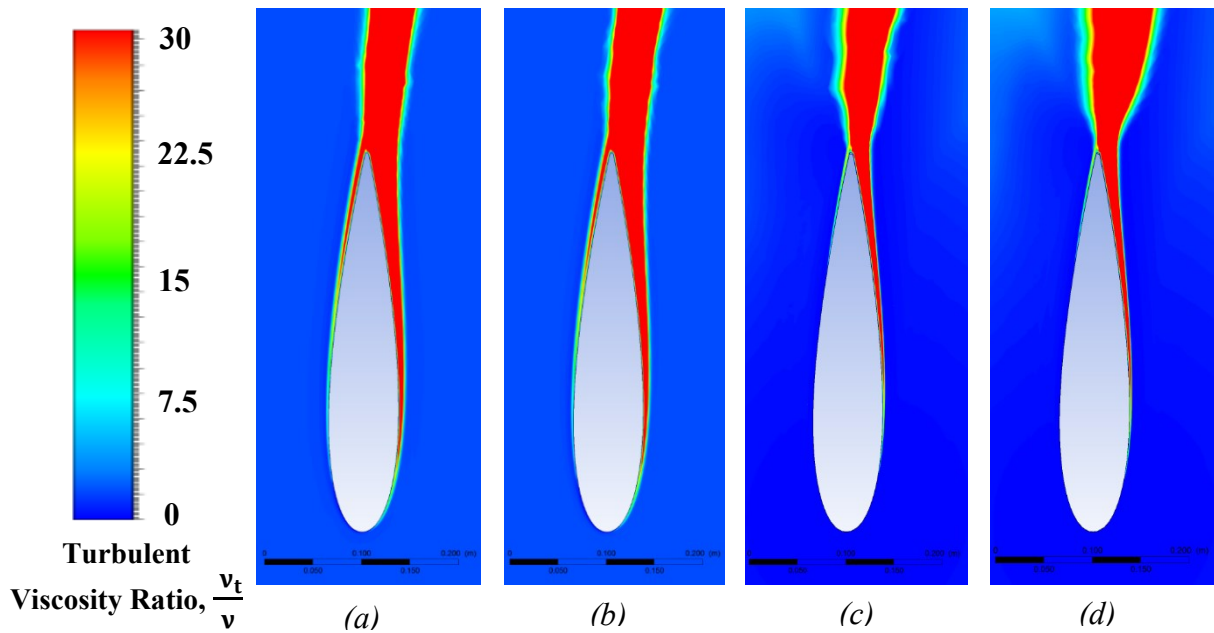


Figure 4.14: Turbulent Viscosity Ratio ($\frac{v_t}{v}$) Plots on a Plane of Half a Chord Away in the Span-Wise Direction from the Symmetry Plane at $t/T=0.33$ for Cases (a) SA Strain/Vorticity ($y^+ \sim 30$) with $AR = 5$, (b) SA Strain/Vorticity ($y^+ \sim 30$) with $AR = 15$ and (c) SST $k-\omega$ ($y^+ \sim 1$) with $AR = 5$, and (d) SST $k-\omega$ ($y^+ \sim 1$) with $AR = 15$

4.5 Comparison of 2D and 3D Results

Figure 4.15 compares the 2D and 3D results for all cases simulated with the SST $k-\omega$ models. It can be seen that as the AR increases, the power curve approaches the 2D results in value and behavior, which is the expected behavior since 2D is considered to be a blade that is infinitely long. This further supports the analysis and the methodology transition from 2D to 3D.

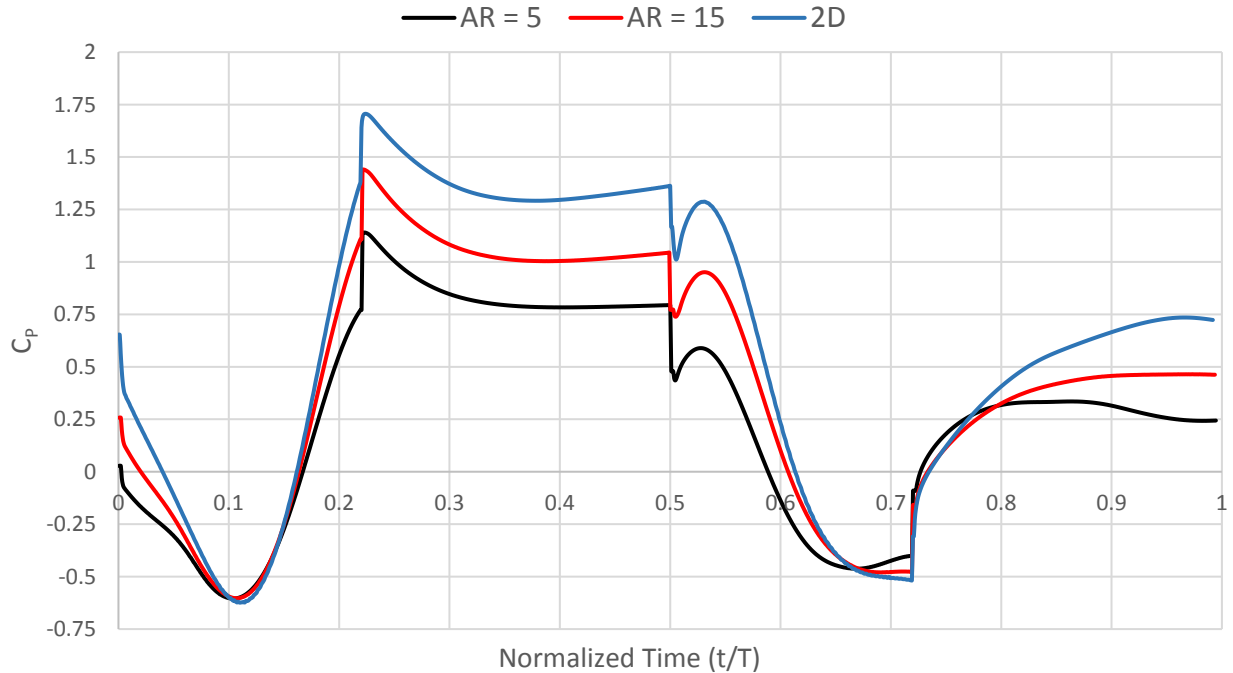


Figure 4.15: Comparing Instantaneous C_P for 2D and 3D with $AR = 5$ and 15 Using the SST $k-\omega$ Model ($y^+ \sim 1$)

The following work will continue the investigation of the D-VAWT to further understand the flow and turbine behavior for different geometrical parameters and operating conditions. The next simulations of the D-VAWT will be performed in 2D only as the trends and behaviors predicted will still be valid for future designs, while the results can be obtained in a matter of days instead of months. To put in perspective, the longest 3D simulation was performed on a cluster of 24 cores with 2.67 GHz processing frequency, which took over eight weeks to complete, while 2D simulations were performed on 12 cores and finished in a matter of hours instead.

4.6 Discussion of D-VAWT Performance

Considering the D-VAWT performance for an AR of 15, the lower and upper bound of the C_P are 0.34 and 0.404, respectively. The actual value would be closer to the upper bound as the simulations with $y^+ \sim 30$ (the lower bound) do not capture the boundary layer flow as accurately as the ones with $y^+ \sim 1$. This finding is supported from the results of the turbulence model and the experimental airfoil case study. Although 3D simulations are much more accurate than 2D simulations, they will still have some level of over prediction of the turbine performance. One should remember that this study is based on a numerical approach, which represents an idealized system where a number of losses are not taken into account. The unconsidered losses include the generator and mechanical losses as well as aerodynamic losses from the lack of simulating the structural components of the turbine. Nonetheless, the predicted C_P values for a straight blade Darrieus type turbine is high, considering this range of C_P is usually seen for the more aerodynamically efficient rotor Darrieus turbines and HAWTs. However, the D-VAWT is still far from being fully optimized. A simple improvement would be to use endplates for the blade, which would reduce the 3D aerodynamic losses and the C_P would further approach the 2D approximation. Based on the results of this study, the D-VAWT concept of extending the region of maximum power production did improve the overall turbine performance. Most performance improvement studies on VAWTS are conducted on optimizing blade profile or other geometric parameters, while the D-VAWT concept is among the few studies that investigated a new and unconventional blade path for a turbine. The following chapter continues with the parametric study to further understand and optimize the D-VAWT.

As mentioned earlier, the C_P for the D-VAWT is high; one should note that it is even more impressive that it is this high for small scale applications. Typically, this range of C_P is difficult to achieve on small scale, even for the HAWTs as they too lose a large portion of their efficiency for small scale application. However, this high performance turbine does come with some drawbacks. The D-VAWT requires the wind to be normal to its longitudinal side for optimal performance, meaning if the wind changes direction, the performance of the turbine will deteriorate depending on how deviated the incoming flow angle is. This is a new weakness that typical other VAWTs do not suffer from. It should be noted that there are solutions to account for different incoming wind directions. The simplest would be to design a shroud to align the flow and provide the D-VAWT with a wider range of operating of incident wind angles. The more complex solution would be a

mechanical one, where one of the two axes' will be allowed pivot in order to always have the turbine longitudinal side to be normal to the incoming wind. The other drawback for the D-VAWT is the higher mechanism complexity compared to the typical VAWT, which are generally quite simple from a mechanical point of view.

CHAPTER 5: 2D PARAMETRIC STUDY

Having completed the validation in 2D and obtained a more realistic performance from the 3D simulations, this chapter presents 2D simulations to further understand and optimize the D-VAWT's performance. Though the results in 2D will over predict the C_P values, the trends obtained in 2D will still be valid and can be incorporated into future 3D designs. The parametric study will include the investigation of the sensitivity to change in wind direction, two bladed turbine, AEF study, high lift airfoil, and blade mounting location. The goal of this chapter is not to perform a detailed parametric study, but it is to serve as the first steps in understanding the D-VAWT's behavior to help guide future studies.

5.1 Introduction to Parametric Study

In this chapter, all simulations are performed using the SST $k-\omega$ ($y^+ \sim 1$) setup since it is capable of capturing the boundary layer more accurately than the SA Strain/Vorticity model setup. For each parameter investigated, a range of TSRs is performed to find the point of peak performance. The goal is not to capture the entire C_P curve (C_P vs. TSR), but to find the effect on the location and value of the peak C_P . One should note that the C_P curve should follow a quadratic curve. For each range of TSRs performed, a quadratic curve will also be fitted from the data for comparison and support of the analysis.

Eq. (5.1) provides the instantaneous angle of attack for different azimuthal angle and TSR values. Figure 5.1 plots the change of angle of attack during the blade rotation of a VAWT for different TSR values. One can see the drop of the maximum angle of attack as the TSR is increased. Below a certain TSR, typically lower than $TSR = 3$, the blade could start to go through dynamic stall and shedding of vortices will occur from flow separation. Since the D-VAWT operates at high TSRs, there are almost no cases where the blade dynamically stalls.

$$\alpha = \tan^{-1} \left(\frac{\sin \theta}{\cos \theta + \lambda} \right) \quad (5.1)$$

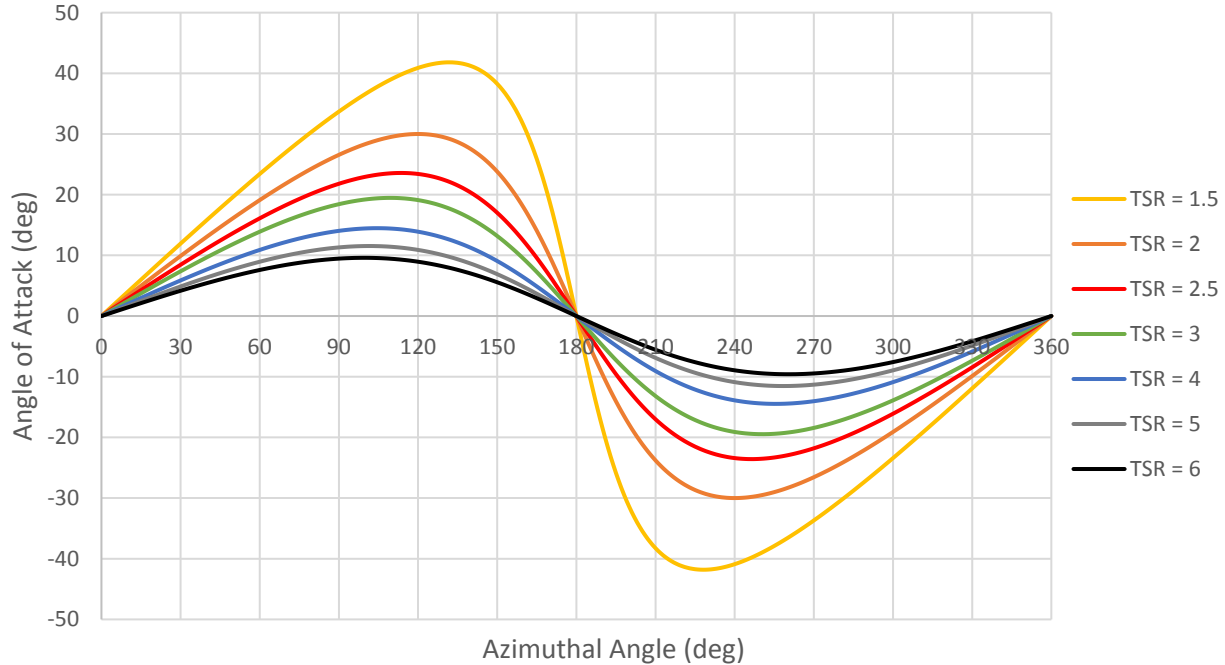


Figure 5.1: Instantaneous Blade Angle of Attack for Darrieus Type VAWT vs Azimuthal Angle for Different TSRs

5.2 TSR Study of Original Turbine

The first step of the parametric study is to find the C_P curve for the original turbine to have a base for comparison when changing the turbine parameters as well as find out at which TSR the turbine has maximum performance. This turbine is still simulated with a single blade at $AEF = 4$.

The results of the simulation are shown in Figure 5.2, Figure 5.3, and Figure 5.4. It should be noted that the case for the $TSR = 4.5$ is repeated again here and one can see the C_P value changed from 0.577 to 0.587. The marginal difference is due to some corrections made in the UDF code, which controls the motion switching criterion between translating to rotating motions. The UDF was only modified now as to have consistent methodology between chapter 3 and 4 and allow for direct comparison between them.

Figure 5.2 shows the cycle to cycle convergence of C_P , where it can be seen that the higher the TSR, the more cycles are required to reach the same convergence as the lower TSR cases. This trend is noticed for all cases simulated in this chapter, where the high TSR cases required a higher number of cycles for convergence. From $TSR 3.5$ to 5, there is less than 6% drop in performance from the peak point, which makes this curve quite “flat” (insensitive to change in TSR) compared to other wind turbines as seen in the C_P curve shown in Figure 5.3. In other words, the insensitivity

to the TSR can also mean that the performance is insensitive to the change in incoming wind speeds if the turbine rotational speed was kept constant. Also from Figure 5.3, the graph confirms that the peak C_P is at $TSR = 4.5$, thus supporting the choice of TSR for the 3D analysis. One can also see the points closely follow the quadratic curve fitted over the points, which also support the methodology and analysis of this turbine.

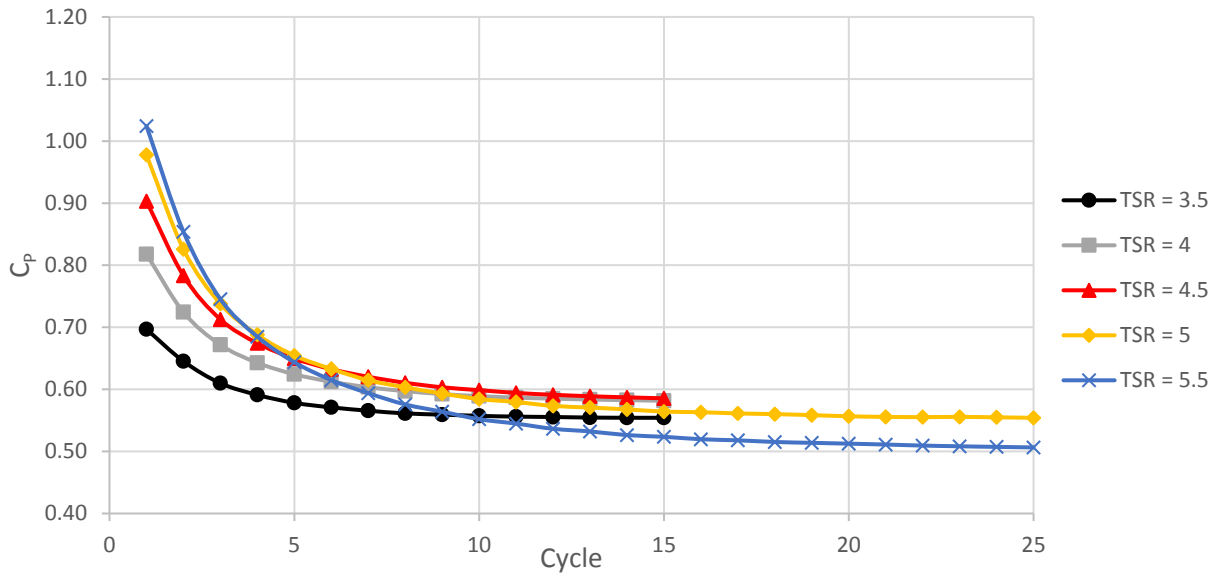


Figure 5.2: Average Power Coefficient Convergence per Cycle for Different TSR values for $AEF=4$

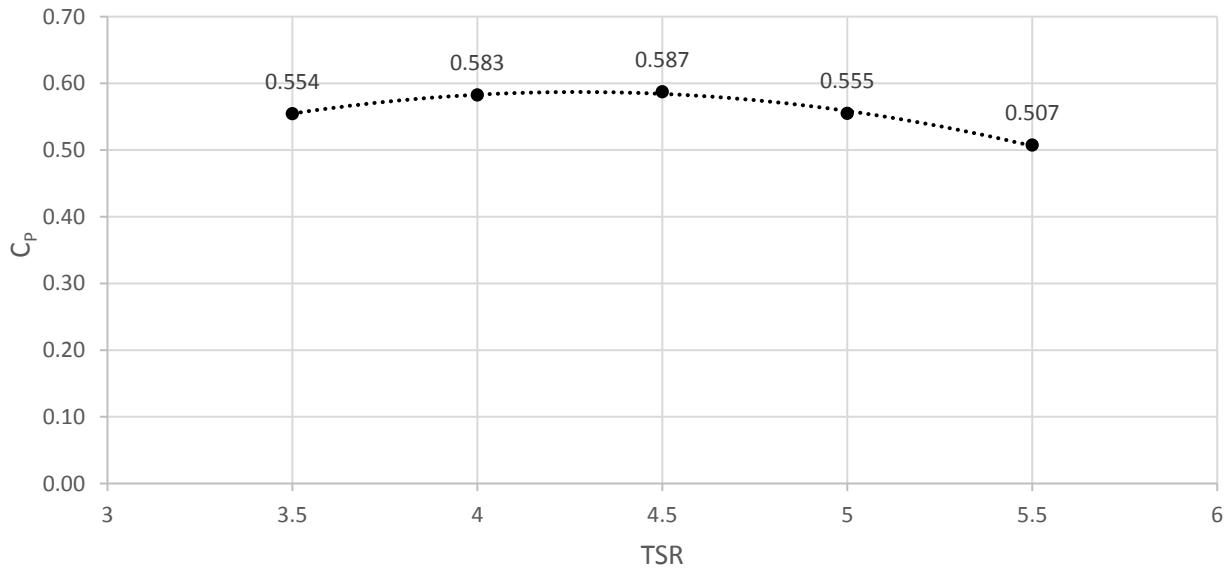


Figure 5.3: Average C_P per Cycle vs TSR for $AEF= 4$ with Quadratic Curve Fitting

To further understand the behavior of the turbine at each TSR, Figure 5.4 shows the plots for the instantaneous C_P for all TSR cases. It can be seen that a higher TSR results in larger positive and negative peaks throughout, except for the downstream translational region, where all TSR cases converge to the same C_P . One can also understand why most H-Darrieus turbines do not operate at such high TSRs is because of the large negative C_P peaks experienced in both rotating regions, which is the entire H-Darrieus' cycle of rotation.

One trend that can be extrapolated from the instantaneous C_P curve is that by increasing the AEF values, the higher TSRs will become more efficient as more time is spent where the highest positive peaks are seen. This means the higher the AEF, the more the peak C_P should move to higher TSR values.

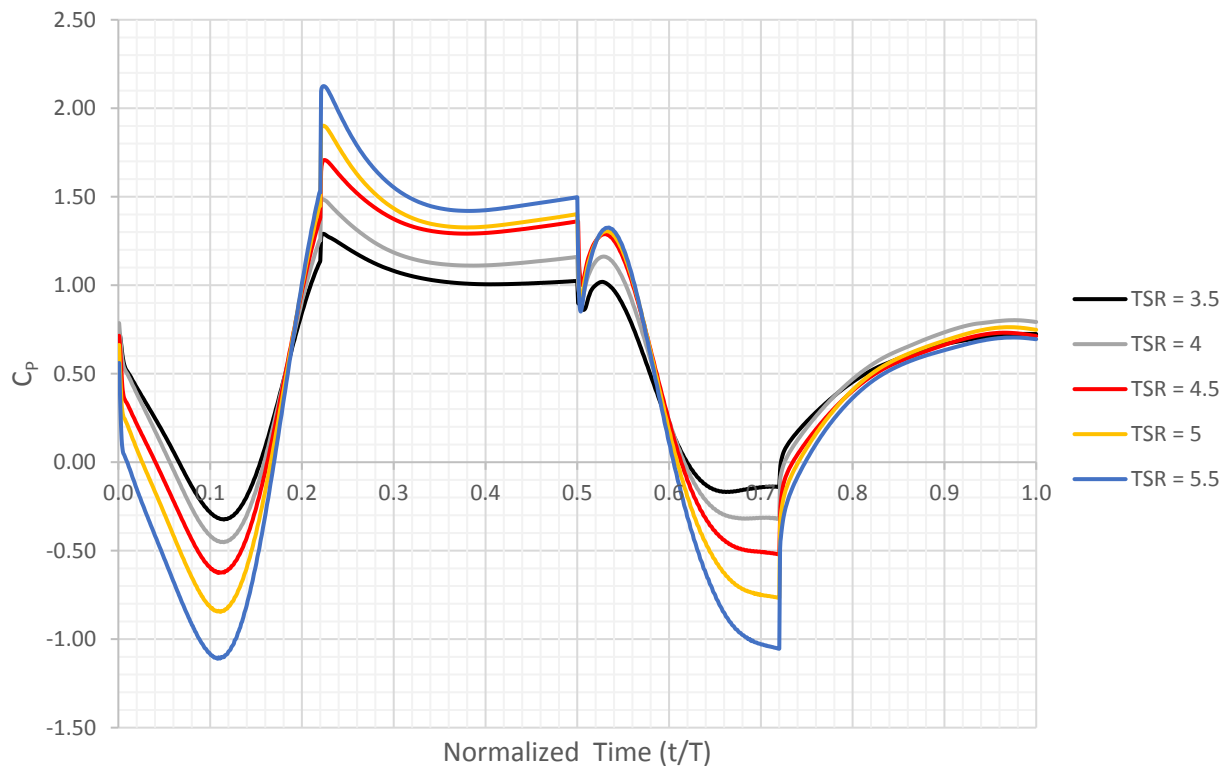


Figure 5.4: Instantaneous C_P for Different TSR Values at $AEF = 4$

5.3 Incident Wind Angle

Since the D-VAWT is not circular in shape, its performance will change if the incoming wind is not normal to its longitudinal side. This section attempts to determine the turbine sensitivity to the incoming wind by simulating six cases and comparing their performances with the zero incident angle presented in the previous section. The six incident wind angles are $\varphi = \pm 20^\circ, \pm 40^\circ, \pm 60^\circ$. The convention for the incident wind angle is shown in Figure 5.5. One should remember that the turbine swept area is reduced with increasing incident wind angle based on Eq. 2.38.

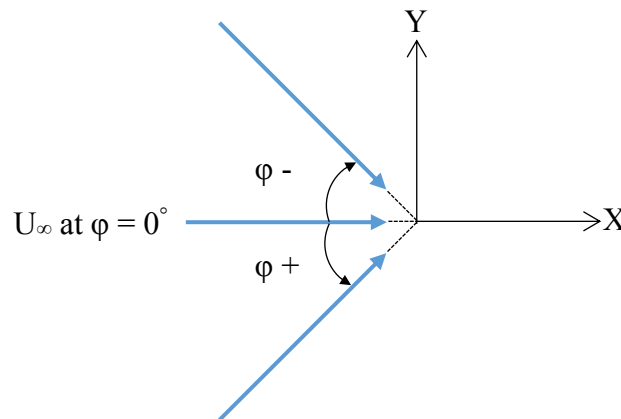


Figure 5.5: Incident Wind Angle Convention

The summary of the C_P curves for all six cases and the original zero incident angle are shown in Figure 5.6. As expected, the best performance is obtained with zero incident angle. All positive incident angles perform better than their equivalent negative ones due to the negative angles increasing the effective angle of attack on the blade in the upstream translational region, leading to a reduced overall performance. At $\varphi = +20^\circ$, the C_P curve highly resembles that of the zero incident angle from a performance and trend point of view as well as even slightly surpassing its performance at $TSR = 5.5$. This is an unexpected behavior and its explanation will be presented at the end of this section. From the same figure, one can see that as the incident angle is increased, both negative and positive angles, the performance worsens and the C_P curve shifts to lower TSR for its peak performance. Though a bit difficult to notice, the higher the incident angle, the more sensitive the performance becomes to the change in TSR, which can be seen as the curve becoming steeper compared to the flatter curve of zero incident angle. One can also see that all curves nicely follow the quadratic curve fitting.

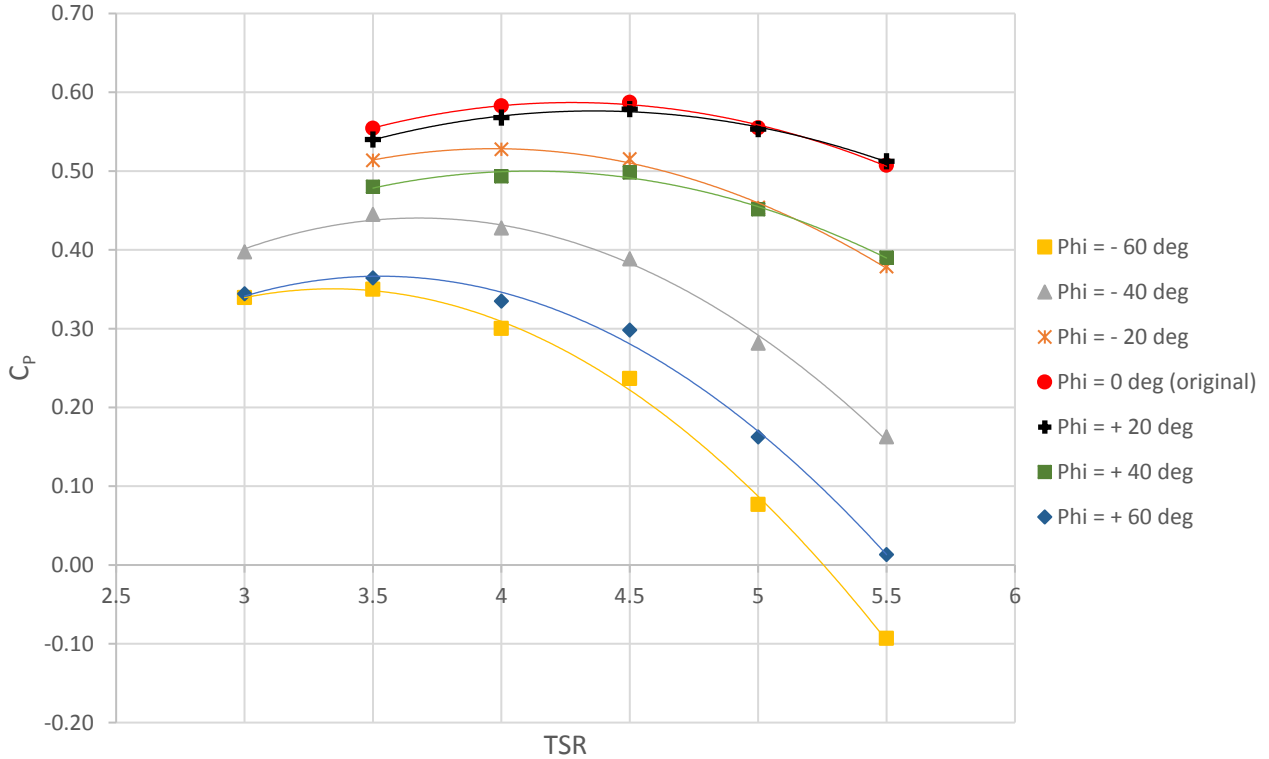


Figure 5.6: Average C_p for Different TSRs with Different Incoming Incident Wind Angles with Quadratic Curve Fitting

Figure 5.7 and Table 5.1 summarize the peak C_p performance of each case. From the graph, one can notice the sharper and more linear drop in power from the negative incident angles. In Table 5.1, the peak C_p for all cases are shown and compared as a percentage to the peak C_p at zero incident angle. At positive and negative incident angle of 20° , the turbine performs at 98.5% and 89.9% of the peak C_p , respectively. This means for an AEF = 4, the turbine loses a maximum of ~10% power for a 40° incident angle range. This result is quite satisfactory as it means that the D-VAWT still performs efficiently for a wide range of incident angles without critically losing its original high efficiency.

Figure 5.8 to Figure 5.13 show the instantaneous C_p curves for all performed TSRs for the incident angles of -20° , -40° , -60° , $+20^\circ$, $+40^\circ$ and $+60^\circ$, respectively. From the figures, one can see as the incident angle increase, the performance of both upstream and downstream translating regions further deteriorates. For the cases of $\pm 60^\circ$, little to negative power is observed in the translating regions. One can also notice that the rotating regions are also affected by the change in incident angle, which was not expected as it was believed the performance in those sections should have

been independent of the incident angle. This effect is due to the wake originating from the translating region traveling towards the rotating regions. For the negative incident angles, the wake travels towards rotating region 2, while for the positive angles, the wake travels towards rotating region 1, which are exactly the two regions that were affected respectively. While one of the rotating region's performance drops in power, the other region increases in peak C_P . Recalling Eq. (2.39) for the C_P calculation, one can see that the increase in the C_P peaks of the rotating regions is a result of the reduction of swept area while the torque remains almost constant in those sections. One can also see that the peak point of the rotating regions moves with changing incident angle, since the change in incident angles results in a direct addition or subtraction of the blade's effective angle of attack.

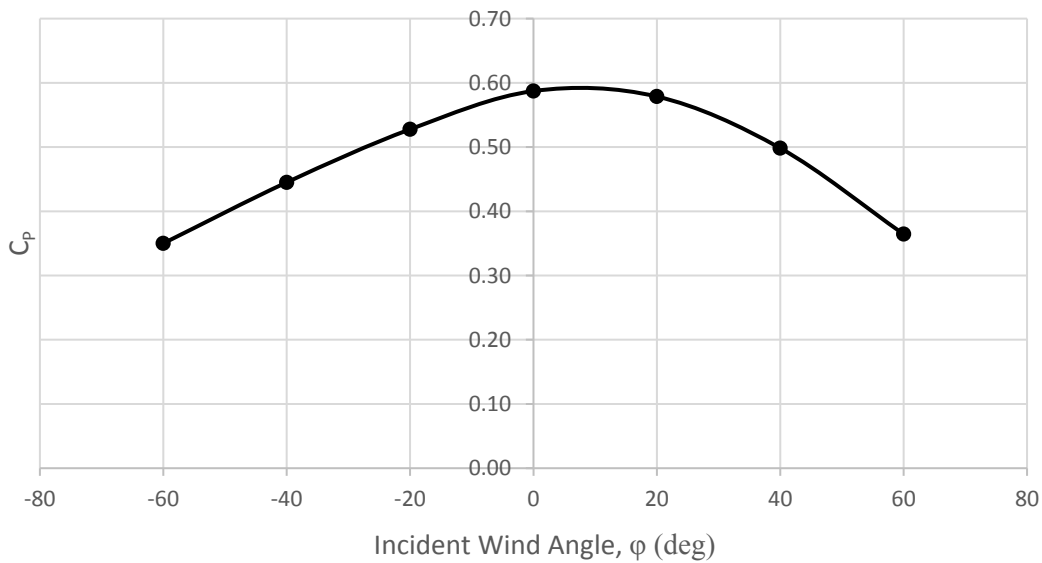


Figure 5.7: Peak C_P for Each Incident Wind Angle

Table 5.1: Summary of Peak C_P for the Incident Wind Angle Study

Incident Wind Angle, ϕ	Peak C_P	Corresponding TSR	% C_P Ratio to $\phi = 0^\circ$
-60°	0.350	3.5	59.6
-40°	0.445	3.5	75.8
-20°	0.528	4	89.9
0°	0.587	4.5	100.0
+20°	0.579	4.5	98.5
+40°	0.498	4.5	84.9
+60°	0.364	3.5	62.0

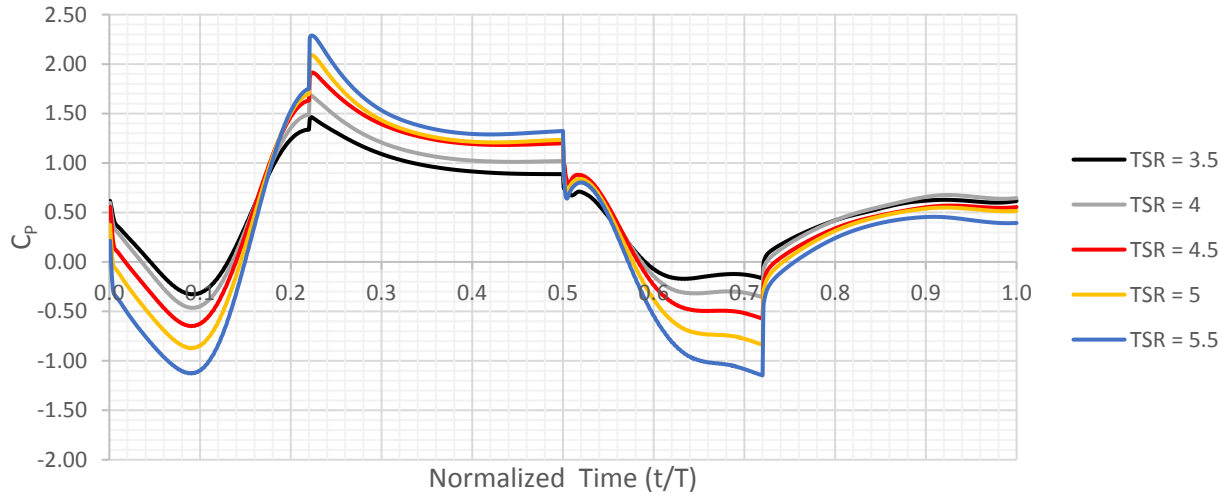


Figure 5.8: Instantaneous C_P for Different TSR Values for $\phi = -20^\circ$

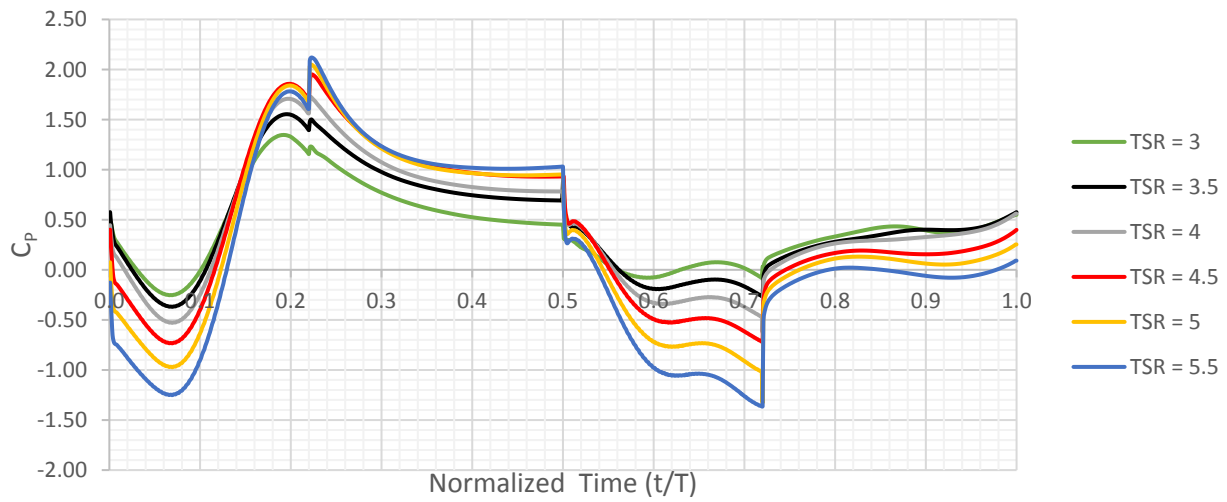


Figure 5.9: Instantaneous C_P for Different TSR Values for $\phi = -40^\circ$

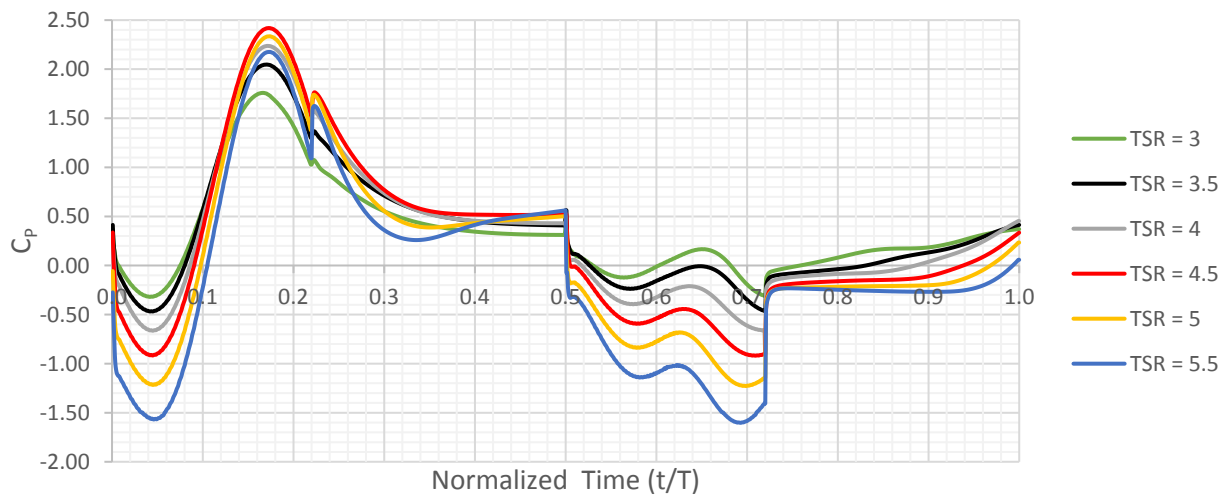


Figure 5.10: Instantaneous C_P for Different TSR Values for $\phi = -60^\circ$

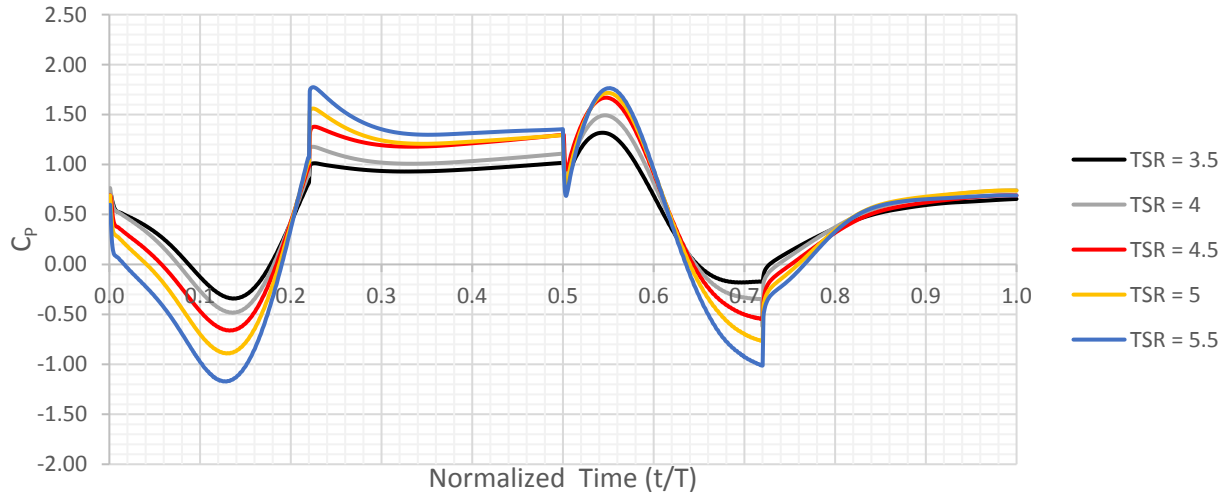


Figure 5.11: Instantaneous C_p for Different TSR Values for $\varphi = +20^\circ$

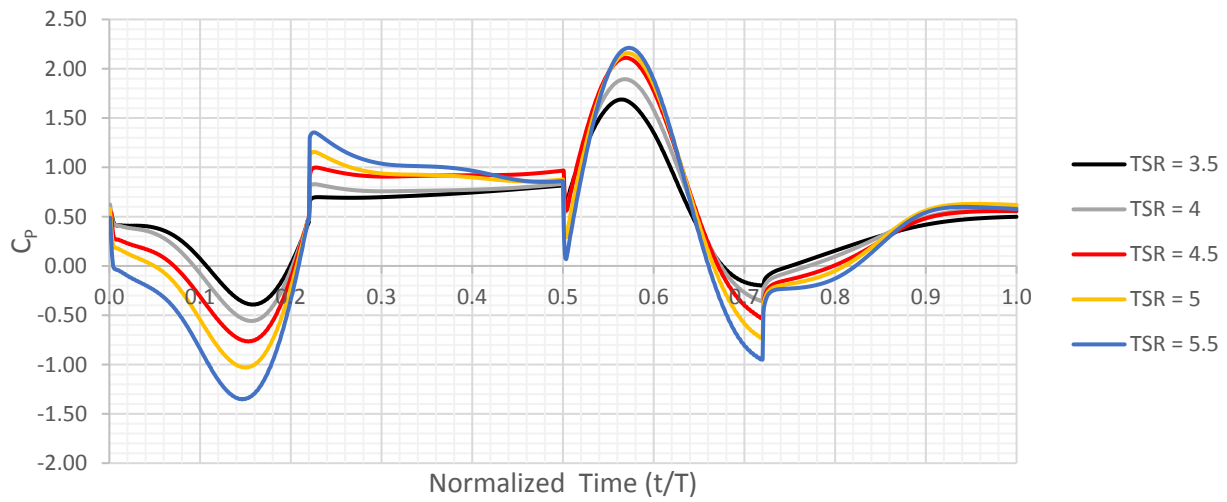


Figure 5.12: Instantaneous C_p for Different TSR Values for $\varphi = +40^\circ$

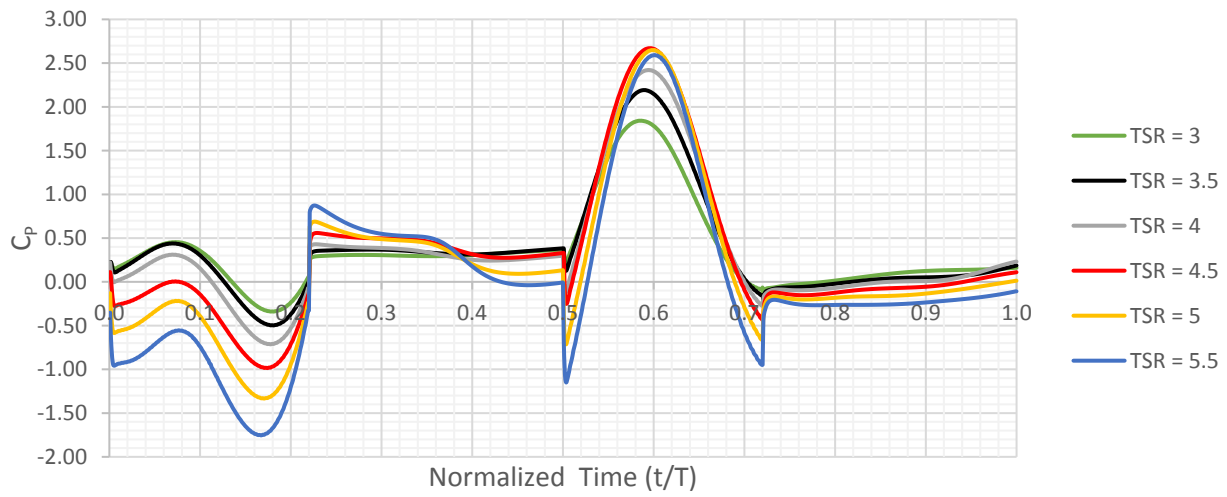


Figure 5.13: Instantaneous C_p for Different TSR Values for $\varphi = +60^\circ$

In order to explain the unexpected behavior at $TSR = 5.5$ where the performance of the $+20^\circ$ incident wind angle surpassed that of the zero incident angle, one should look at the individual average C_P for each region, which have been summarized in Table 5.2. Rotating region 1 is the region adversely affected by the wake crossing it for the cases of positive incident angles, which explains the loss of power in this section. For the upstream translating region, though the blade experiences a smaller tangential force for the positive incident angle, due to the reduced swept area from the incident angle which increases in the C_P , the overall loss in this region is small. The significant difference in C_P can be seen in the rotating region 2, where there is over a 1000% increase in performance for the positive incident angle which is due for two reasons. This region sees cleaner free stream flow for the positive incident angle, increasing its performance, while having its swept area reduced from the incident angle. These two positive effects help create this large difference in performance for the positive incident angle. The downstream translating region behaves similarly to the upstream translating region, resulting in a small loss in performance. Combining all the mentioned behaviors, the resulting total cycle average is slightly higher for the positive incident angle in this case. It should be noted that calculating the cycle average is not the direct average of the four sections, since the weight of the translating regions is larger as more time is spent translating. To summarize, though the $+20^\circ$ incident angle performs worse in three out of the four sections, its performance is so much higher in the rotating region 2, that it compensates and surpasses the zero incident angle's performance.

Table 5.2: Summary of Average C_P per Section at $TSR = 5.5$ for $\varphi = 0^\circ$ and $+20^\circ$

Region	Incident Wind Angle, φ		% Difference
	0°	$+20^\circ$	
	Average C_P		
Rotating Region 1	-0.291	-0.440	- 50.9
Upstream Translating Region	1.558	1.385	- 11.1
Rotating Region 2	0.036	0.460	+ 1181.4
Downstream Translating Region	0.449	0.424	- 5.7
Total Cycle Average	0.507	0.512	+ 1.0

5.4 Axis Eccentricity Factor (AEF)

The AEF is the newly introduced parameter for D-VAWTs which dictates the spacing of the two axes if the radius is already chosen. Previously, an AEF of 4 was used for all analyses performed. In this section, D-VAWTs with an AEF of 8 and 12 are simulated and compared to the original AEF. It is of interest to first know the percentage of time spent translating versus rotating for different AEF Values. Eq. 5.2 presents the equation for the ratio of time spent translating to the cycle period, while Figure 5.14 shows the change of that said percentage of the ratio with AEF. One can see the initial rapid growth of translating time for small AEFs and that above an AEF of 3.1, the blade spends more than 50% of the time translating. For the tested AEFs of 4, 8 and 12, the percent time translating are 56%, 71.8% and 79.3%, respectively. It can be seen for large AEF values, increasing it from 8 to 12, resulted only in an additional 7.5% increase in translating time.

$$\text{Translating Time Ratio} = \frac{2 t_{\text{Translational}}}{2 (t_{\text{Translational}} + t_{\text{Rotational}})} = \frac{\frac{L}{\omega R}}{\frac{L}{\omega R} + \frac{2\pi}{\omega}} = \frac{1}{1 + \frac{\pi}{AEF}} \quad (5.2)$$

Where $t_{\text{Translational}}$ and $t_{\text{Rotational}}$ are the times spent by the blade in each translating and rotating regions, respectively.

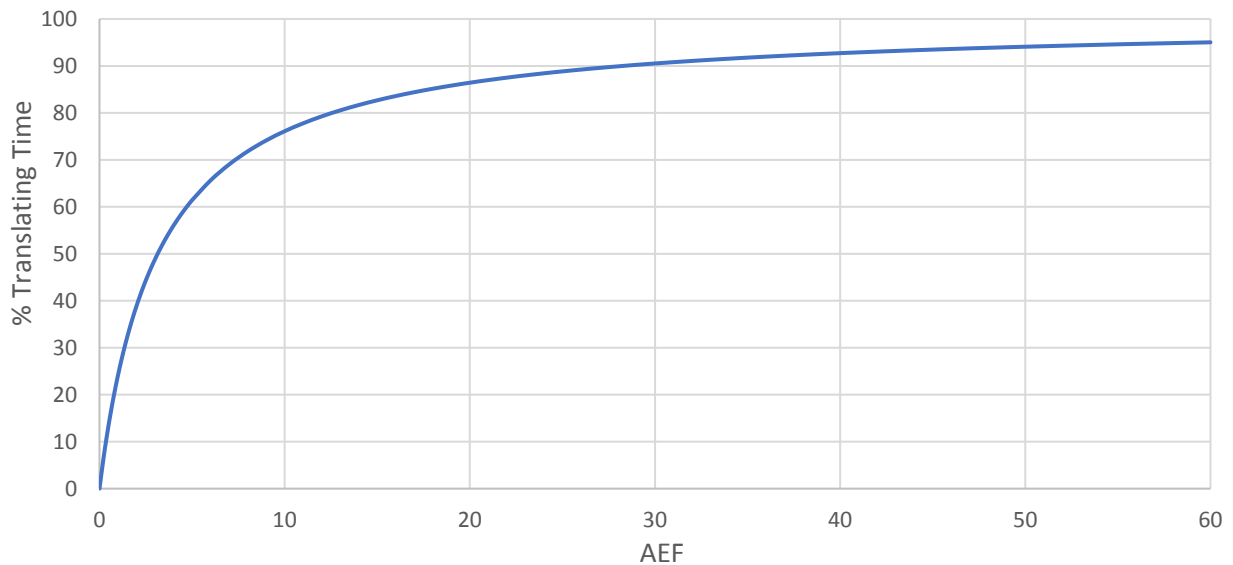


Figure 5.14: Percent Time Translating vs AEF

The C_P curve for all AEFs are shown in Figure 5.15, while Table 5.3 compares the peak C_P and power values. From Figure 5.15, one can see that increasing the AEF lowered the peak C_P and, as

expected, shifted the peak to higher TSRs. Table 5.3 shows that increasing the AEF from 4 to 12 resulted in a ~10% loss in peak C_P value; however, due to the larger turbine area from increasing the AEF, the power produced from the turbine of AEF 12 is over double that of the original turbine's. It should be noted that the power values presented in Table 5.3 are for a 2D area, thus they are powers per unit depth.

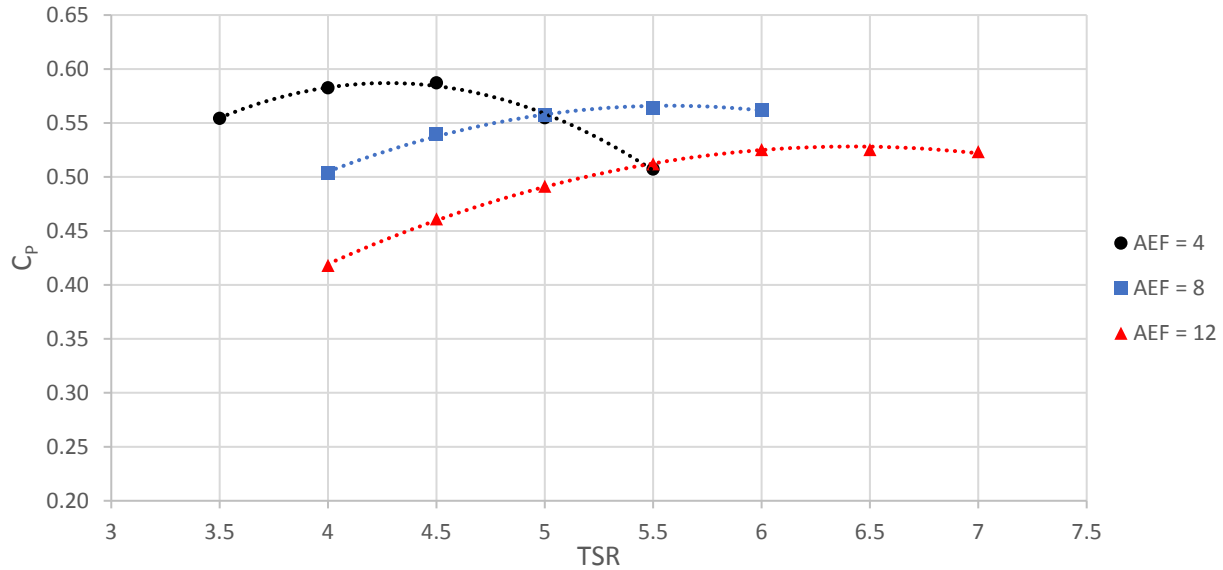


Figure 5.15: Average C_P per Cycle vs TSR for AEF Study with Quadratic Curve Fitting

Table 5.3: Summary of AEF Study for Peak Performance

AEF	Peak C_P	Corresponding TSR	% C_P Ratio to AEF = 4	2D Power (W)	% Power Ratio to AEF = 4
4	0.587	4.5	100.0	110.42	100.0
8	0.564	5.5	96.1	176.99	160.3
12	0.525	6.5	89.5	230.68	208.9

An interesting behavior is noticed where increasing the AEF, resulted in a flatter curve or in other words, a turbine less sensitive to TSR. This can be confirmed by looking at Table 5.4 which presents data obtained using MATLAB's curve fitting function of 2nd order polynomials from the C_P curve data. One can see that the range of TSR values operating at an aerodynamic efficiency higher than 90% of the peak C_P increases with increasing AEFs. Increasing the AEF from 4 to 12

increased that said TSR range by 62.4%. Meaning that although the turbine with AEF of 12 has a lower peak C_P , the turbine has a more efficient operating range as well as higher overall power produced due to the larger turbine area.

Table 5.4: Summary of AEF Study for Peak and 90% of Peak Performances Using Curve Fitted Data

AEF	Curve Fitted Peak C_P	Corresponding TSR	TSRs Operating at \geq 90% Peak C_P	Total TSR Range Operating at \geq 90% Peak C_P	% Ratio of TSR Range to AEF = 4
4	0.5872	4.28	3.24 to 5.32	2.08	100.0
8	0.5659	5.56	4.06 to 7.06	3.00	144.3
12	0.5285	6.43	4.74 to 8.11	3.38	162.4

Figure 5.16 and Figure 5.17 show the instantaneous C_P for AEFs of 8 and 12, respectively. If one were to look at the same TSR for different AEF values, one can see that the average C_P in the translating regions is lower due to the fact that the blade produces the same amount of tangential force while the swept area is larger, thus resulting in a lower C_P value. It should be mentioned that although the average C_P in the translating regions is significantly lower for increasing AEFs, a bigger portion of time is spent translating, allowing it to maintain an overall high cycle C_P . Two interesting behaviors are noticed from the instantaneous C_P figures. First, one can clearly see that in the upstream translating regions, there is an initial jump in power, a fast drop and then a slow increase again in C_P towards the end of that said region. Second, since the translating regions are now much bigger, one can see that the downstream translating regions are now almost reaching the same C_P as the upstream region. This is due to most of the upstream wake crossing by before the blade returns in the downstream portion, where it sees a more free stream like flow with higher wind velocity than for the lower AEF cases.

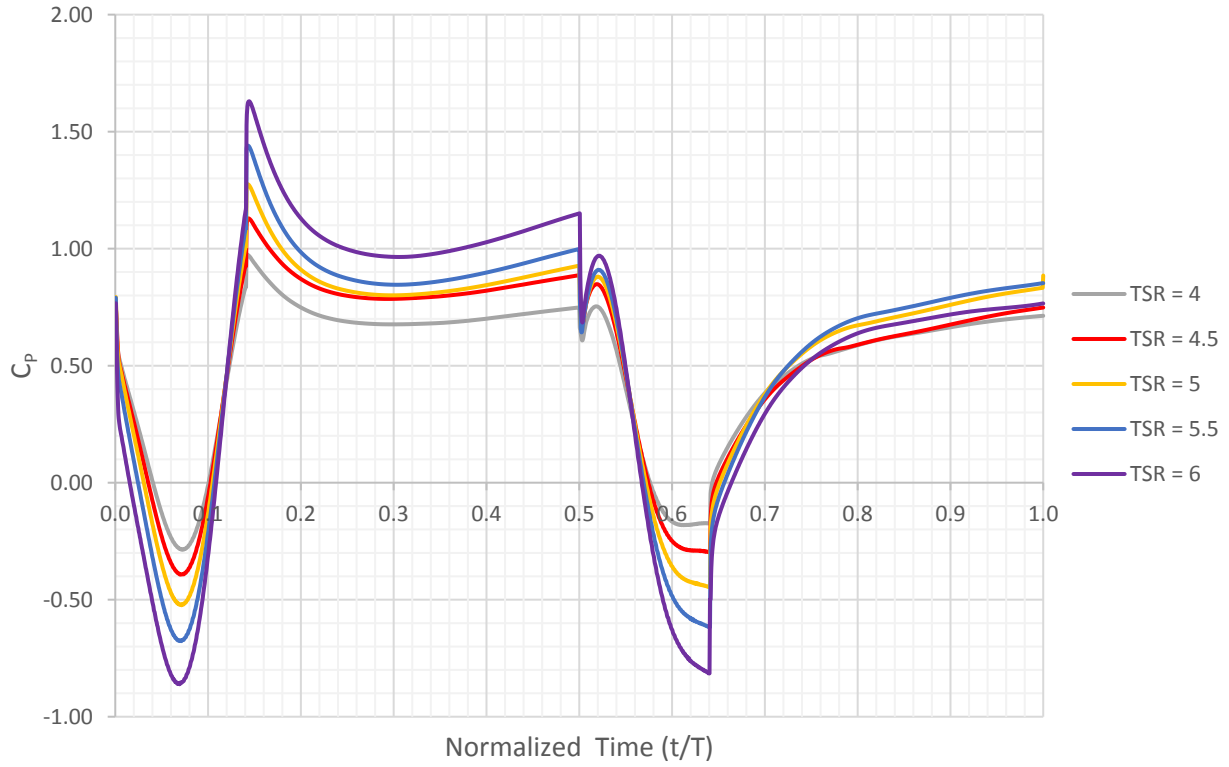


Figure 5.16: Instantaneous CP for Different TSRs with AEF = 8

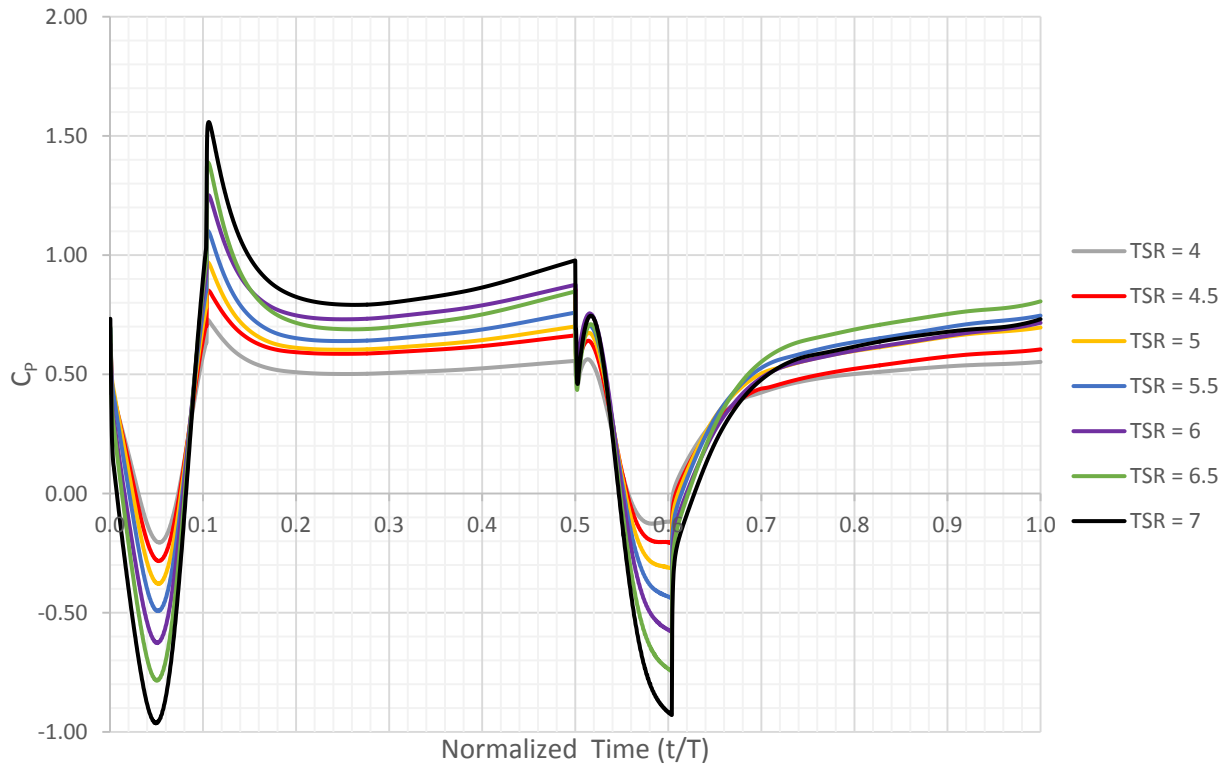


Figure 5.17: Instantaneous CP for Different TSRs with AEF = 12

5.5 Multi-Blade Turbine Analysis

In this section, a turbine with two blades is simulated using type 3 motion, which as mentioned, is the only motion technique that allows the simulation of a turbine with more than a single blade. The blade chord is maintained, meaning the solidity has now doubled in value, changing from 0.167 to 0.333. Typically, wind turbines with low solidity have their peak C_P at high TSR, while for high solidity turbines it is at low TSR. Since the solidity of this D-VAWT is increased, one would expect the peak C_P to shift to a lower TSR.

Figure 5.18 shows the mesh at the starting point of the simulation and at the time where the blades reach mid-way of the translating region. Figure 5.19 shows a closer view of the mesh when the blades are again mid-way in the translating regions. At this location, the blades are closest to each other. One should notice that all elements in the deforming domain are specified to be the same size as to allow better control over the mesh deformation and re-meshing as well as retain higher overall element quality.

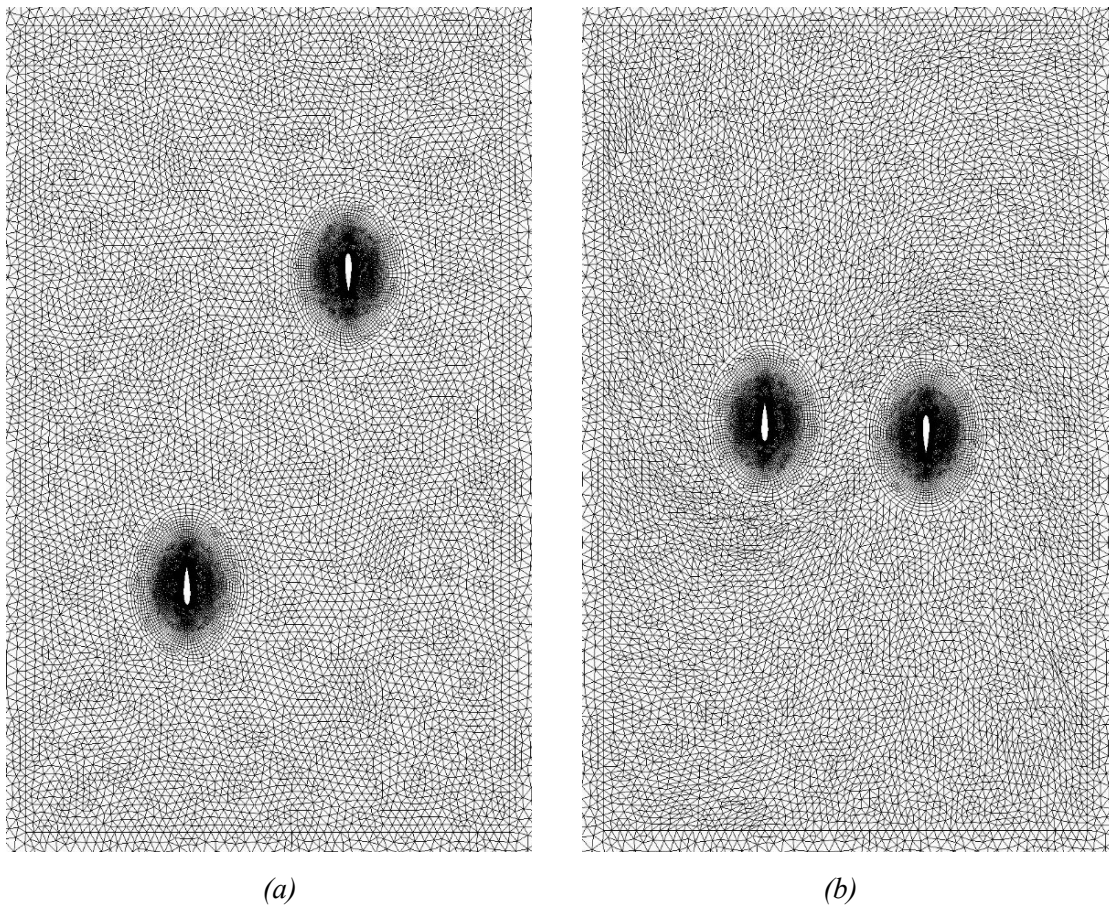


Figure 5.18: View of Deforming Domain at (a) $t/T = 0$ and (b) $t/T = 0.36$

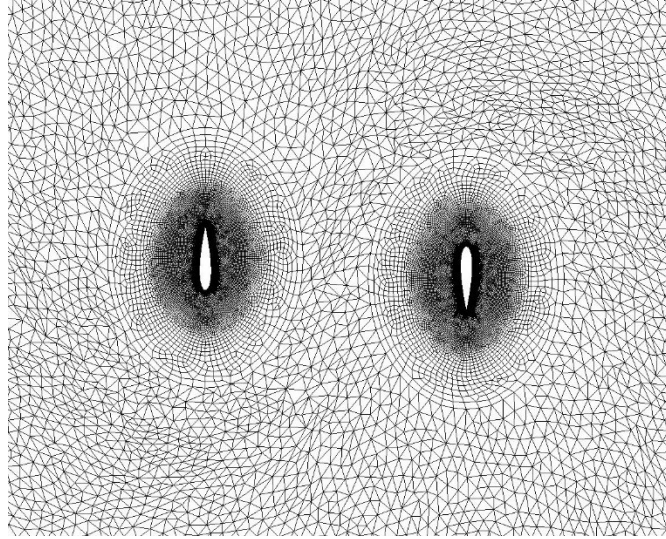


Figure 5.19: Close View of Mesh Around Blades at $t/T = 0.36$

Figure 5.20 shows the cycle C_P convergence where similar to before, higher TSRs required more cycles to reach convergence. However, for a two bladed turbine simulation, more cycles were required for the TSRs of 3.5 to 4.5 to reach convergence. Figure 5.21 compares the C_P curve for the single and two bladed turbine. As expected, the peak C_P is now at TSR 3 instead of 4.5. The peak C_P increases from 0.587 to 0.604 for a single to a two blade turbine. Another thing to notice in the C_P curve is that increasing the solidity also increased the turbine sensitivity to TSR as seen by the curve becoming less flat.

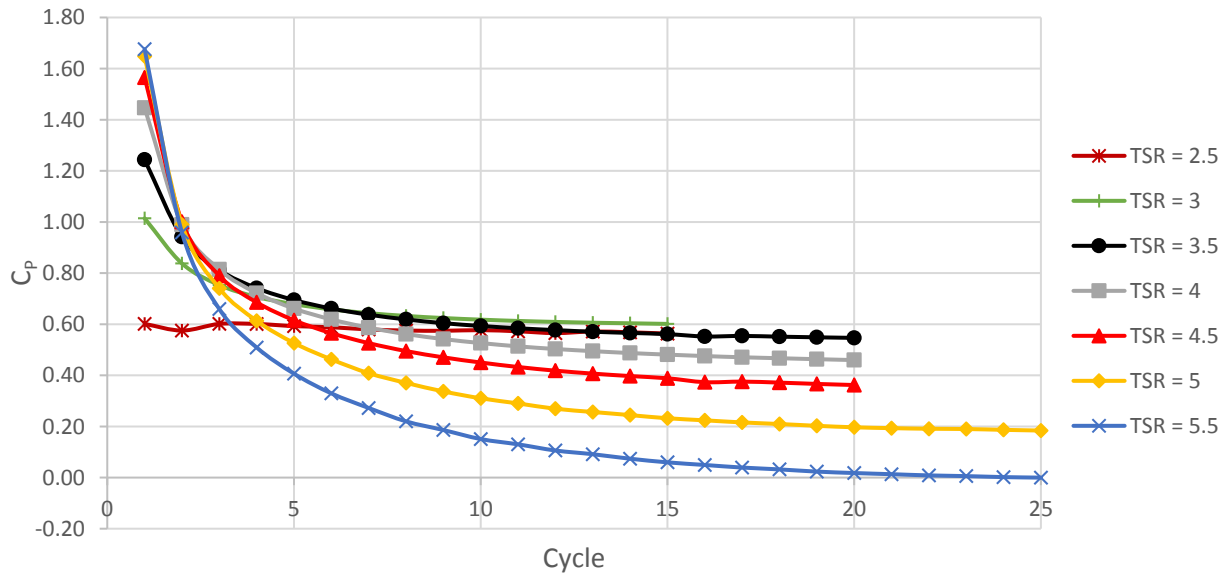


Figure 5.20: Average Power Coefficient Convergence per Cycle for Different TSR values for Two Bladed Turbine

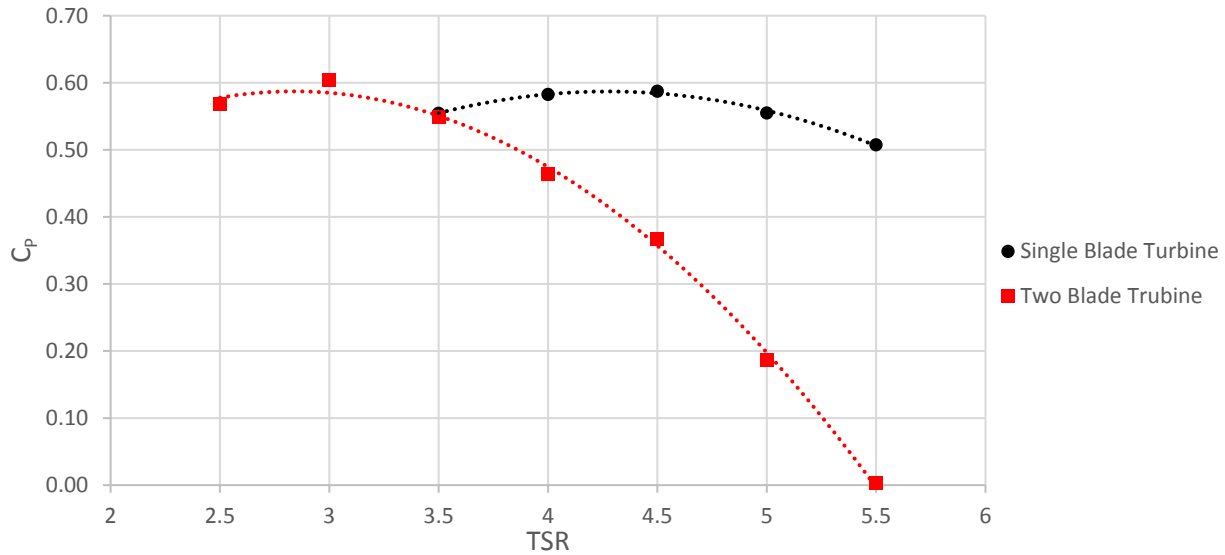


Figure 5.21: Average C_p per Cycle vs TSR for a Single and Two Bladed Turbine

Figure 5.22 and Figure 5.23 show the instantaneous C_p for Blade 1 and the total C_p of the turbine (Blade 1 + Blade 2). As expected for increasing the turbine solidity, each individual blade performs worse than for the single bladed turbine as each of the two bladed turbine sees lower velocity from free stream since the turbine blockage increased. This can be confirmed by looking at Figure 5.24, which compares the C_p for the best performing TSR for the single blade turbine, Blade 1 of the two blade turbine and the total of the two blade turbine. Comparing the performance of the single blade turbine with Blade 1, it is clear how little power Blade 1 produces by itself. Also, one can see the symmetry of the C_p for the total of the two blade turbine between the first and second half of the cycle due to the presence of the second blade and that very small portions of the rotation have negative C_p compared to the single blade turbine, allowing it to slightly surpass the single blade turbine performance.

From Figure 5.22, one can see in the upstream translational region that increasing the TSR increases the C_p , however, a large loss is suffered in the downstream translating region. This results in all TSRs having near the same power drawn in the translating region when looking at the total power produced from the two blades in Figure 5.23. Also, the higher the TSR value, the worse is the performance in the rotating regions, leading to the lower TSRs to perform much better overall in this case.

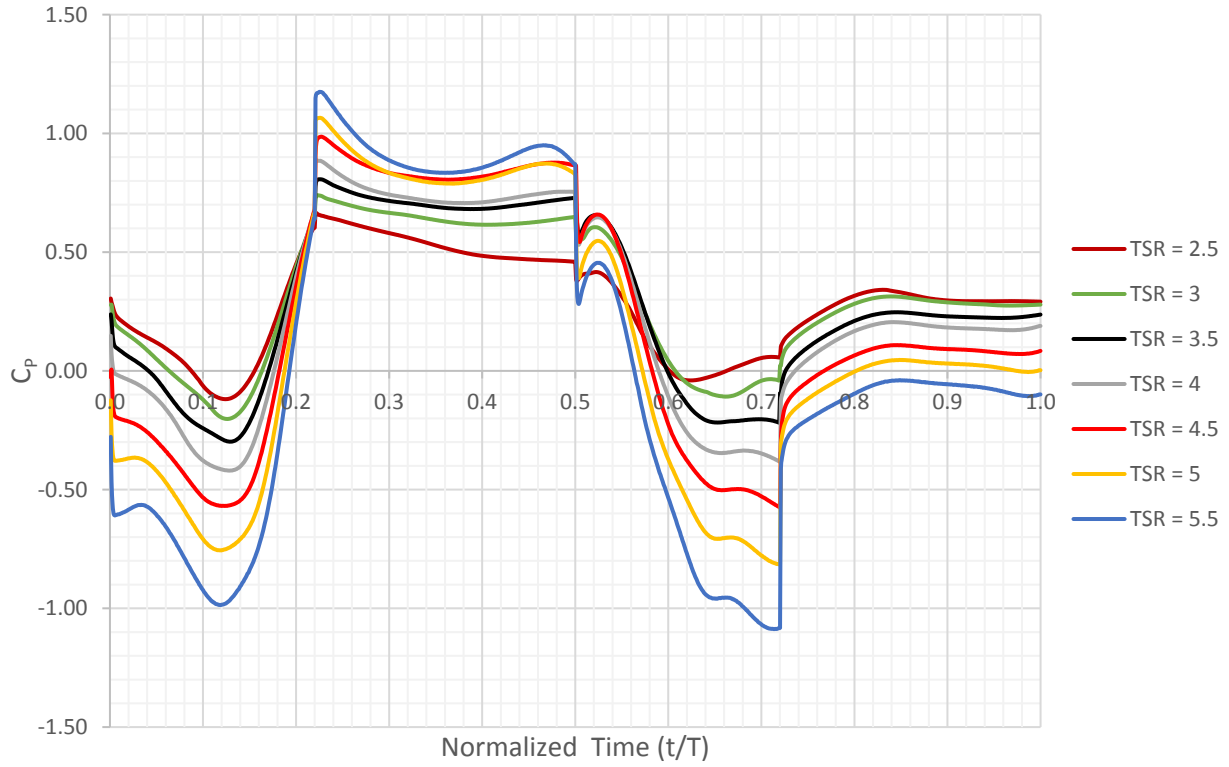


Figure 5.22: Instantaneous C_p of Blade 1 of the Two Bladed Turbine

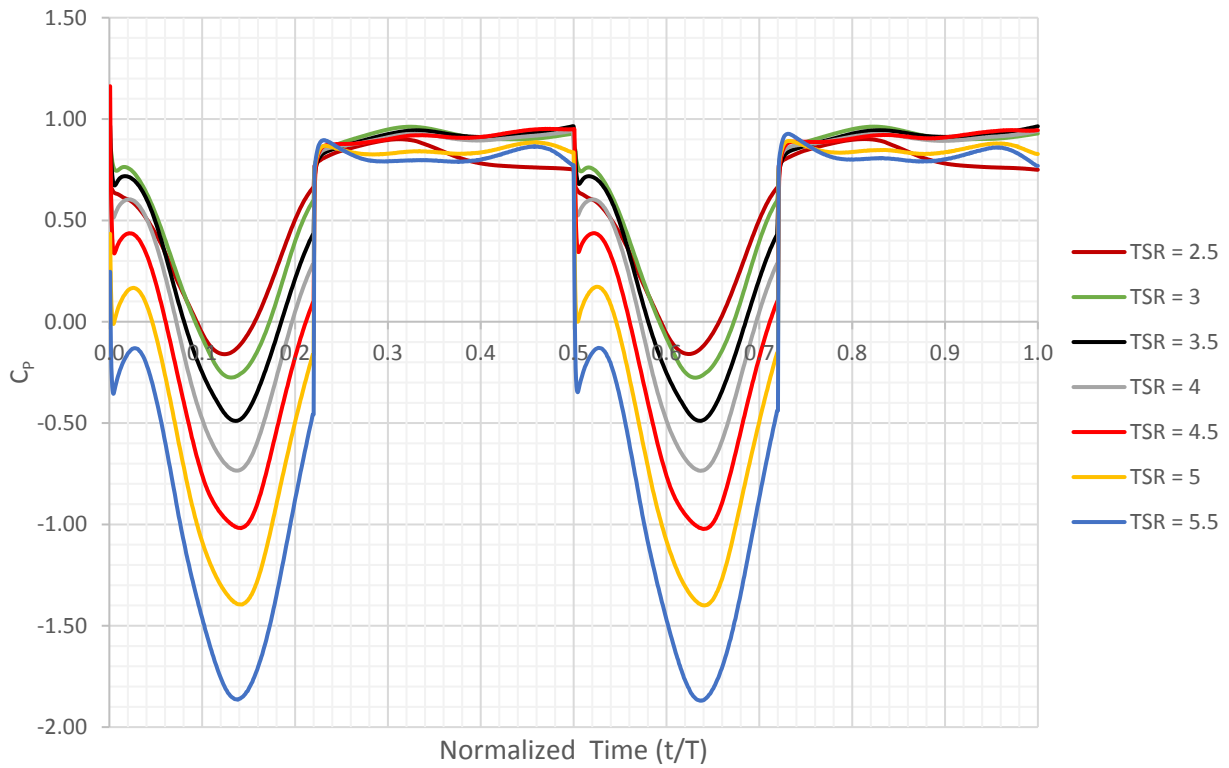


Figure 5.23: Total Instantaneous C_p for Two Bladed Turbine

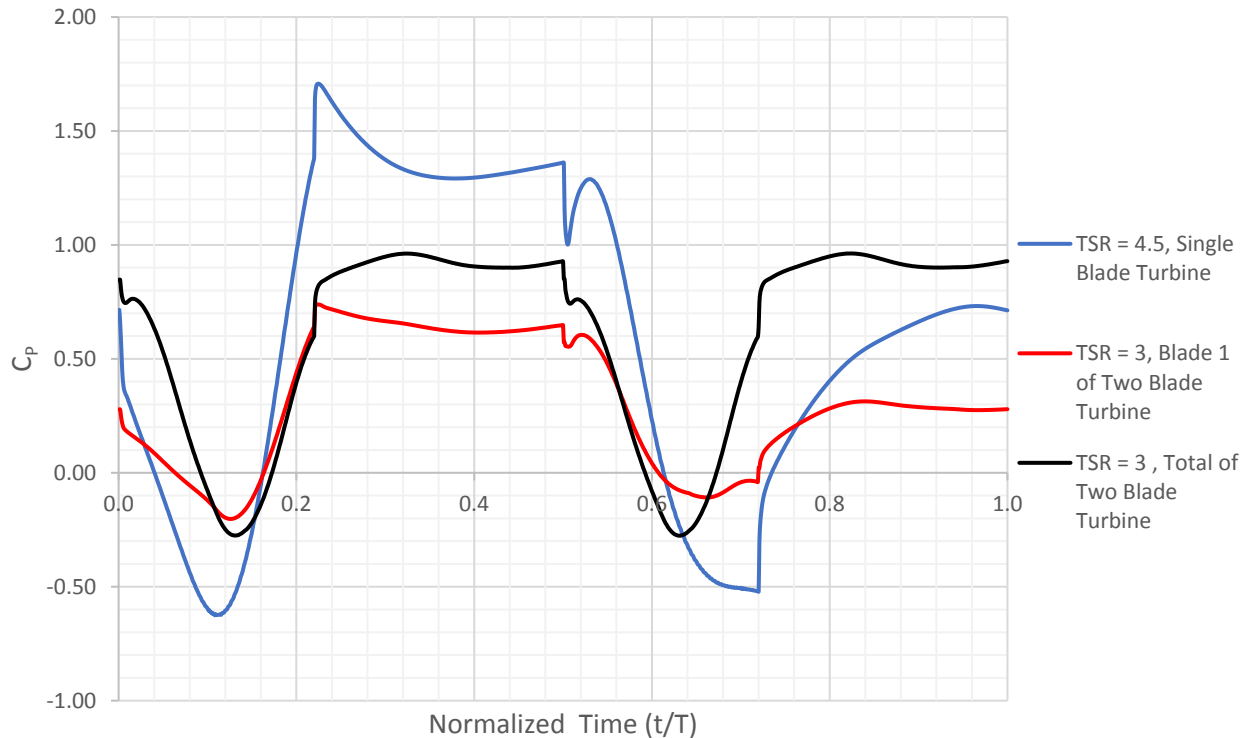


Figure 5.24: Comparison of Instantaneous C_p at Best TSR for the Single and Two Blade Turbines

5.6 High Lift-to-Drag Airfoil

This analysis was inspired by Selig and Guglielmo [64], where they analyzed the S1223 airfoil. The S1223 is a cambered high lift to drag type airfoil. The S1223 and NACA 0018 airfoil profiles are shown in Figure 5.25. The problem with using cambered airfoils for VAWT applications is that the camber will only benefit the turbine during only one half of the rotation, which can either be the upstream or downstream half of the rotation depending on whether the camber is towards or away from the turbine center. For one half of the rotation, the camber will have a positive effect on the performance, while the other half will result in a negative effect as the blade angle of attack is now negative on the camber, most likely resulting in dynamic stall.

The blade camber was placed away from the turbine center for the upstream translating region as to have the positive effect during that said region. The C_p curve of the S1223 is shown in Figure 5.26 and compared to the original airfoil, the NACA 0018. Changing to the S1223 airfoil resulted in a 32% loss of the peak C_p value. This result was expected and Figure 5.27 confirms the reason mentioned earlier in that only half of the rotation will result in a gain while the other half will be at a disadvantage. The average C_p of the upstream translational region for S1223 at $TSR = 4$ (highest

C_p cycle) is 2.112 while the NACA 0018 at $TSR = 4.5$ (highest C_p cycle) produces an average of 1.38. Although this is a 53% increase in performance in the upstream translational region, the rest of the cycle is worse and even the downstream translational region draws power as seen from the negative C_p . The oscillations seen in the instantaneous C_p graph in the downstream translation region are a result of vortices shedding due to flow separation because of the large negative angle of attack experienced by the blade facing the wrong side of the camber.

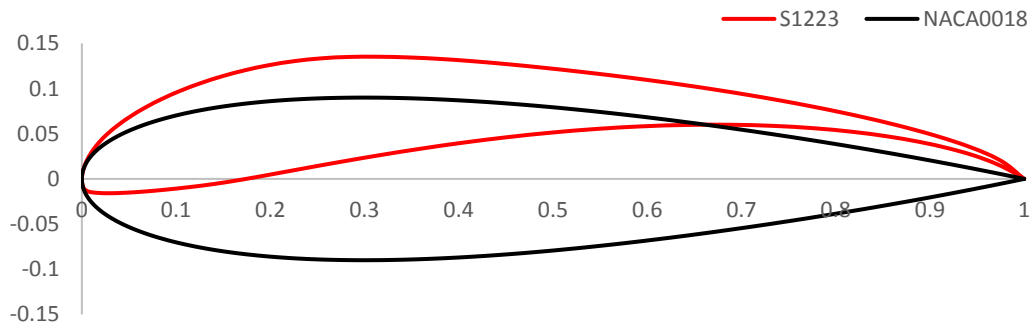


Figure 5.25: S1223 and NACA 0018 Airfoil Profile

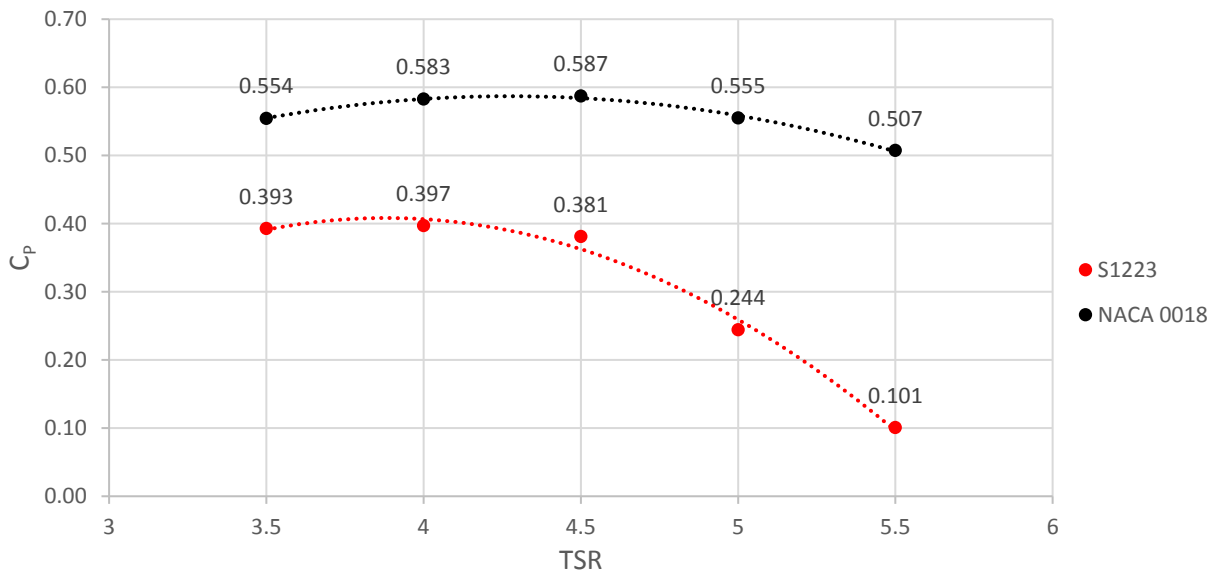


Figure 5.26: Average C_p per Cycle vs TSR for Different Blade Airfoil Profiles

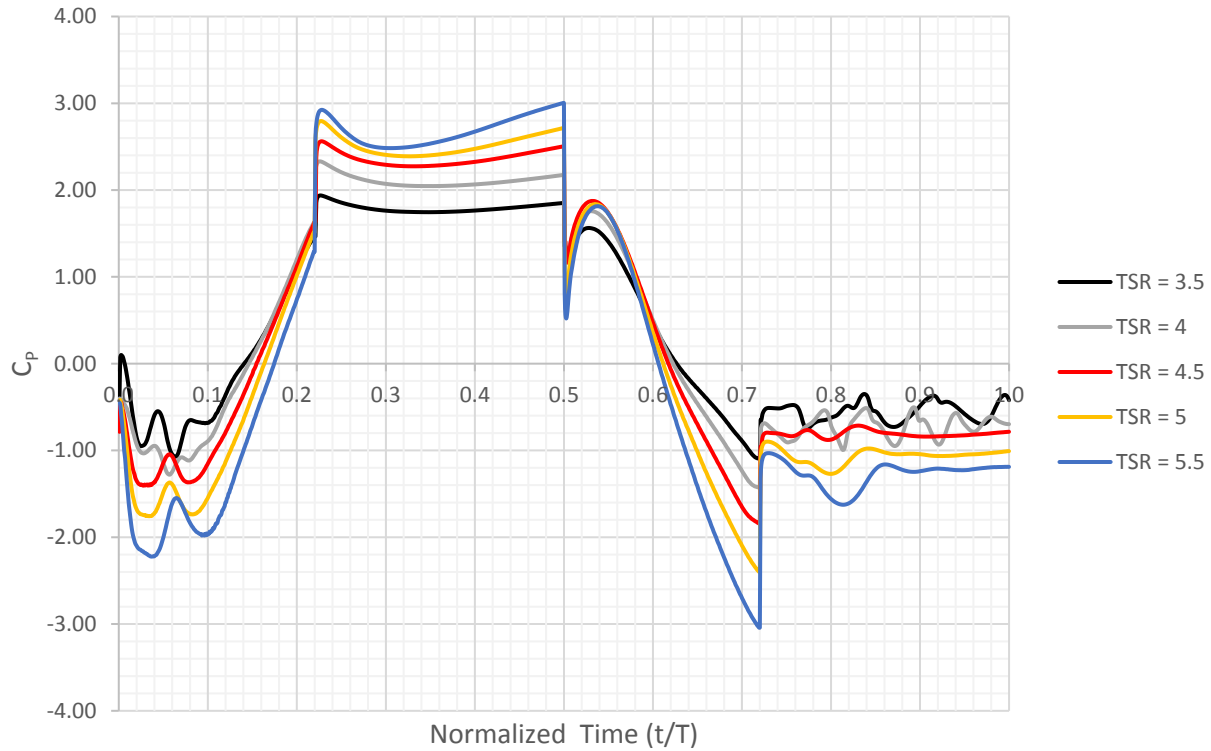


Figure 5.27: Instantaneous C_P for Different TSRs for the S1223 Airfoil

5.7 Blade Mounting Point

The blade mounting point is where the blade is attached to by the support arm. In this section, the mounting point is investigated as a study performed by Fiedler and Tullis [65] showed a significant improvement in the peak C_P curve form changing the mounting from $C/3$ to $C/2$. The $C/3$ mounting location refers to one third of the blade chord from the leading edge. However, their result is unexpected since a change in the blade mounting point should only result in a change of the blade's effective angle of attack, meaning the C_P curve should shift to a higher or lower TSR depending on where the mounting point is changed to. It should be noted that in [65], they did not complete the TSR curve for the $C/3$ mounting point case as to find the actual peak C_P , meaning they could have missed the actual peak value of the curve.

The original mounting point was at $C/3$ while the investigated mounting point is at $C/2$. The results for the average C_P for each TSR is shown in Figure 5.28. As expected, the C_P curve shifts to a higher TSR while still maintaining the same peak C_P value.

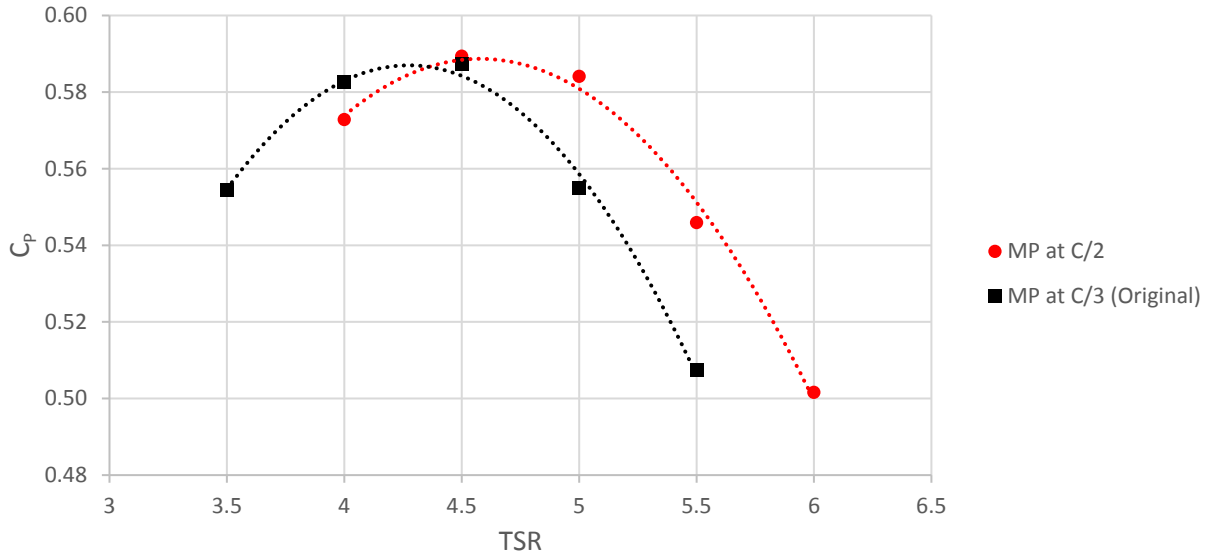


Figure 5.28: Average C_p per Cycle vs TSR for Different Blade Mounting Points (MP)

The instantaneous C_p can be seen in Figure 5.29, where similar trends are observed to the original mounting point. The only difference is noticed in the upstream translational region, where the peak is noticed to occur towards the end of the region instead of happening at start as previously seen.

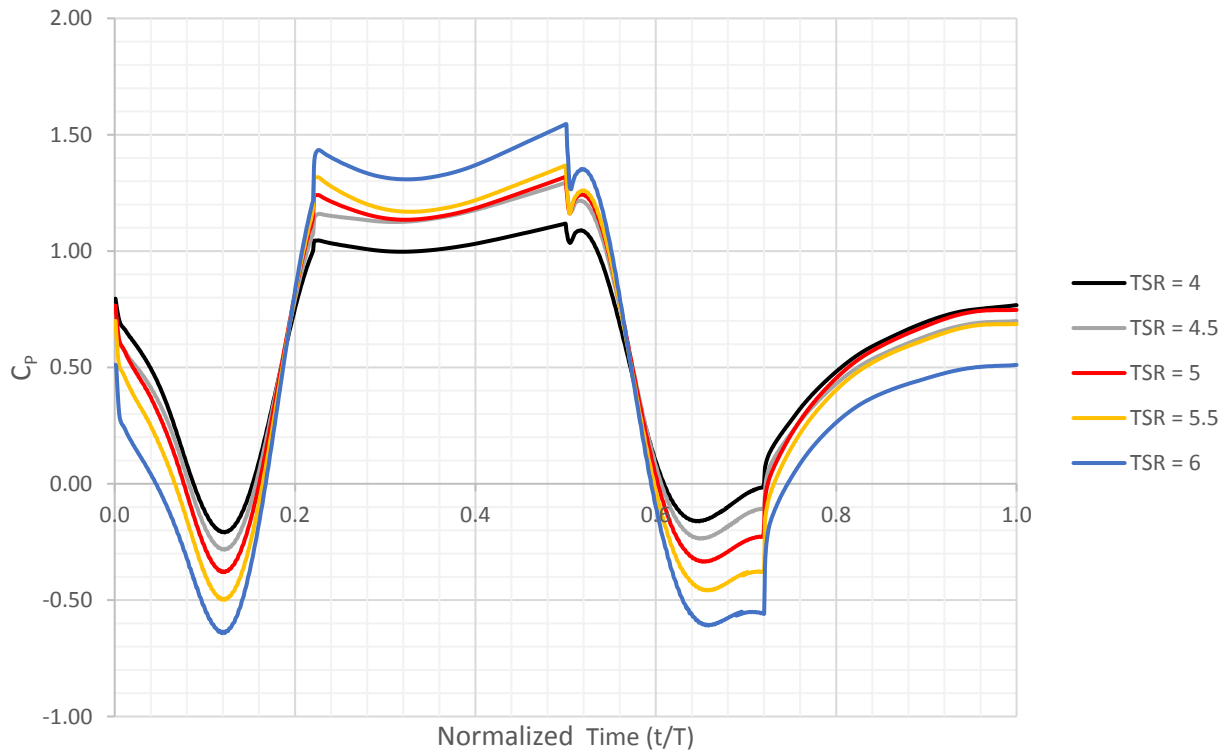


Figure 5.29: Instantaneous C_p for Different TSRs for the Blade Mounting Point at Half Chord

5.8 Summary and Discussion of Parametric Study

In this chapter, the TSR behavior of the original turbine was investigated as well as five other parameters, including the incident wind angle, AEF, number of blades, airfoil profile and blade mounting point. It was noticed that in general, the C_P curve of the D-VAWT is not highly sensitive to the change of TSR compared to most other wind turbines, which is another benefit of the D-VAWT design. Through the incident wind angle study, it was confirmed that though the turbine does indeed lose performance with incident wind angles other than zero, for a 40° range ($\pm 20^\circ$) of incident angles, the turbine loses only a maximum of 10% of its aerodynamic efficiency. From the AEF study, it was found that increasing the AEF lead to a reduction of the peak C_P , an increase in the actual power output, and the C_P curve becoming less sensitive to the change in TSR. By studying a two bladed turbine with double solidity, it was found that the peak C_P slightly increased and the C_P curve shifted to a lower TSR while also becoming more sensitive to the change of TSR. From the study of a high lift cambered airfoil, it was confirmed that for D-VAWT application, the camber will sacrifice the power on half of the cycle, leading to a significant loss in overall aerodynamic efficiency. Finally, the mounting point study showed that it is possible to shift the C_P curve to a higher or lower TSR by modifying the blade mounting point, while still retaining the original performance of the D-VAWT.

Since the analyses performed in this chapter constitute the preliminary analysis of the parametric study, each parameter was investigated separately to help isolate each of their effects on the performance. However, it is not possible to design a turbine based on a single parametric study, but a multi-objective study is needed. For example, the wind sensitivity study showed that 10% loss is sustained in aerodynamic efficiency for a 40° range, but this was done on an AEF of 4. The losses could be greater or lower if one were to change the AEF value or perhaps add another blade. Thus performing such parameter combinations is necessary as it is possible that the trends from parameter combinations to behave differently from the ones predicted in the current analysis. Performing such analyses can be extremely time consuming as there is a very large number of possible cases that could be generated. This is why performing the current preliminary analysis should help guide future designs of the D-VAWT and reduce the number of cases to a manageable amount.

CHAPTER 6: CONCLUSION

6.1 Summary

Using CFD as the design tool, 2D simulations were used for the methodology validation of the D-VAWT, while 3D simulations were used to obtain a more realistic performance prediction. The validation of the methodology was performed for a single blade in 2D, where the mesh convergence, domain size, turbulence model, y^+ strategy, and blade motion prescription were investigated. The methodology was also validated with experimental results of a static airfoil in 2D. The SA Strain/Vorticity turbulence model was shown to be a lower bound estimate of the coefficient of power while the SST $k-\omega$ turbulence model gave a more accurate prediction of the performance.

The novelty of the D-VAWT design is that it is among the few studies that modified a turbine's blade path in an attempt to improve the aerodynamic efficiency. In this thesis, it was shown that the D-VAWT design did indeed succeed at improving the aerodynamic efficiency of small scale turbines which has been a challenge to overcome for many decades. The performed tests have shown the great potential of the D-VAWT by reporting a high C_P performance of 0.4 for $AR = 15$ based on the 3D simulation. For a common straight blade Darrieus type turbine, a C_P of 0.4 is very high and difficult to achieve. However, the proposed D-VAWT is still far from being fully optimized. It is also important to note that because the D-VAWT requires the wind to be perpendicular to its longitudinal side to have optimal performance, this turbine now becomes dependent on wind direction, which is a drawback not encountered in traditional VAWTs.

A preliminary parametric study was performed, where it was found that the D-VAWT has a low sensitivity to the change of TSR compared to most other wind turbines. The incident wind angle study showed that a maximum of 10% aerodynamic efficiency is lost for a $\pm 20^\circ$ range of incident angles while a maximum of 40% aerodynamic efficiency is lost for a $\pm 60^\circ$ range of incident angles. The AEF study showed that increasing the AEF will lower the peak C_P , increase power output, and reduce the TSR sensitivity. By studying a two bladed turbine, it was shown that the D-VAWT maintained its high performance while reducing its TSR value at peak performance and increasing its sensitivity to TSR change. Cambered airfoils were shown to reduce the overall

performance of D-VAWTs. Finally, the blade mounting point study showed no improvement in performance but a shift in TSR at peak performance is possible.

6.2 Contributions

The following is the list of contributions of this thesis:

- Proving the D-VAWT concept and performing a preliminary parametric study of design variables;
- Developing three moving mesh techniques to model the motion of a D-VAWT;
- Comparison of different turbulence models for D-VAWT applications.

6.3 Future Work

Future studies will continue the investigation of the D-VAWT to further understand the flow and turbine behavior for different geometrical parameters and operating conditions. Future studies can still be performed in 2D as the trends and behaviors predicted will still be valid for future designs, while the results can be obtained in a matter of days instead of months. A more in-depth parametric analysis is required to optimize the D-VAWT. This will also require a multi-objective study where more than one parameter is modified at once since the behavior from the parameter combinations could result in new trends. For example, one should combine the AEF with the incident wind angles study or the AEF study with multiple blades. More analyses are required for more multi-blade type D-VAWTs as a turbine with a single and two blades were simulated. However, the additional blades will create more interaction between all the blades and the flow, which require further simulations to comprehend that said interaction.

The dimensions of the turbine should be also investigated as only a single turbine size was investigated in this study. This should be done in conjunction with a structural analysis to obtain a viable design. The mechanism of the D-VAWT will also need to be designed and included in the structural analysis.

One interesting concept will be to simulate a turbine with variable TSR in a cycle. Since the D-VAWT's translating regions operated more efficiently at high TSR, while the rotating regions operated more efficiently at low TSR, combining a high and low TSR value in one cycle could result in much more aerodynamically efficient turbine. The difficulty will be designing a mechanism to account for a variable TSR during the blade rotation.

Once a complete design is obtained from future 2D investigations, a full scale 3D simulation, without the symmetry condition, should be performed with an atmospheric velocity inlet boundary condition to obtain an even more realistic estimate of its performance. Also, to obtain even more realistic results, one should simulate the D-VAWT mechanism as it will add additional drag and fluid-structure interactions (FSI) with the blades as well as using a 6 degree of freedom (DOF) type simulation in Fluent to consider the inertia of the components. The D-VAWT is not limited to urban applications. It can be used on a much larger scale in the field outside cities, however, the large scale version of the D-VAWT will also require investigation to ensure its optimal performance.

Since the D-VAWT requires the wind to be normal to its longitudinal side for optimal performance, combining the D-VAWT with a shroud could help align the flow in the desired direction. The shroud should provide the D-VAWT with a larger operating range of incident wind angles. The other solution to help with the wind dependency problem is a mechanical solution, where one of the two axes is allowed to pivot so that the flow is always normal to the longitudinal side of the turbine. Both solutions are viable and require further investigation.

With the D-VAWT concept proven, it is also possible to investigate a turbine with different blade paths such as one with a triangular shape with three axes to make the turbine performance even less sensitive to wind direction. Finally, a study where one combines the D-VAWT with the morphing blade technology to maximize the airfoil's lift potential throughout the entire blade path could be interesting to investigate.

6.3.1 Future Work Summary

- Perform a multi-objective parametric study and optimization.
- Investigate the D-VAWT for different sizes and develop its mechanism.
- Study a case with variable TSR in a cycle (i.e. High TSR in translational region and low TSR in rotating regions).
- Perform full 3D simulations with atmospheric inlet velocity, multiple blades, and mechanical components.
- Combine the D-VAWT with a shroud or axis pivotal system.
- Investigate new blade paths such as a triangular shaped path.
- Investigate morphing blade technology with the D-VAWT.

REFERENCES

- [1] OECD and IEA, “Key World Energy Statistics,” IEA Publishing, Paris, 2015.
- [2] Natural Resources Canada, “Energy Fact Book,” 2015-2016.
- [3] Global Wind Energy Council, “Global Wind Report - Annual Market Update,” Brussels, 2015.
- [4] World Wind Energy Association, J.-D. Pitteloud, and S. Gsanger, “Small Wind World Report,” Tokyo, 2016.
- [5] Reve, “Siemens Provides 157 Wind Turbines for Three Wind Power Projects in South Africa.” [Online]. Available: <http://www.evwind.es/2015/02/18/siemens-provides-157-wind-turbines-for-three-wind-power-projects-in-south-africa/50574>. [Accessed: 23-Jul-2016].
- [6] Québec en Saisons, “Découvrez les secrets de «Éole Cap-Chat».” [Online]. Available: http://www.quebecensaisons.com/ete2009/eole_cap_chat.php. [Accessed: 23-Jul-2016].
- [7] R. D, “Vertical Axis Wind Turbine Installed in P-Town.” [Online]. Available: <http://www.alternativeconsumer.com/2009/06/30/vertical-axis-wind-turbine-installed-in-p-town/>. [Accessed: 23-Jul-2016].
- [8] Quiet Revolution, “The qr6 Vertical Axis Wind Turbine.” [Online]. Available: <http://www.quietrevolution.com/>. [Accessed: 23-Jul-2016].
- [9] Wind Harvest International, “WHI 70 kW.” [Online]. Available: <http://www.windharvest.com/>. [Accessed: 23-Jul-2016].
- [10] P. Kozak, “Effects of Unsteady Aerodynamics on Vertical-Axis Wind Turbine Performance,” MS Thesis, Dept. of Mech. and Aero. Eng., Illinois Institute of Technology, Chicago, Ill., 2014.
- [11] S. Eriksson, H. Bernhoff, and M. Leijon, “Evaluation of different turbine concepts for wind power,” *Renewable Sustainable Energy Rev.*, vol. 12, no. 5, pp. 1419–1434, 2008.
- [12] R. Guillo, “Darrieus vertical axis wind turbine.” [Online]. Available: http://www.ecosources.info/en/topics/Darrieus_vertical_axis_wind_turbine. [Accessed: 02-Feb-2016].
- [13] E. Hau, *Renewable Energy, Fundamental, Technology, Applications and Economics*, Berlin Heidelberg. Springer-Verlag, 2006.
- [14] Gamma Energy, “Teoria delle turbine eoliche.” [Online]. Available: <http://www.gammaenergy.it/eolico/teoria-delle-turbine.html>. [Accessed: 07-Jul-2016].
- [15] I. Paraschivoiu, *Wind Turbine Design with Emphasis on Darrieus Concept*. Montreal: Presse Internationales Polytechniques, 2002.

- [16] S. N. Zadeh, M. Komeili, and M. Paraschivoiu, “Mesh Convergence Study for 2-D Straight-Blade Vertical Axis Wind Turbine Simulations and Estimation for 3-D Simulations,” *Can. Society Mech. Eng.*, vol. 38, no. 4, pp. 487–504, 2014.
- [17] ANSYS Inc., 2011. ANSYS FLUENT 14.0 User’s Guide, URL: www.fluent.com.
- [18] X. Jin, G. Zhao, K. Gao, and W. Ju, “Darrieus vertical axis wind turbine: Basic research methods,” *Renewable Sustainable Energy Rev.*, vol. 42, pp. 212–225, 2015.
- [19] F. L. Ponta, J. J. Seminara, and A. D. Otero, “On the aerodynamics of variable-geometry oval-trajectory Darrieus wind turbines,” *Renewable Energy*, vol. 32, no. 1, pp. 35–56, 2007.
- [20] F. L. Ponta and L. I. Lago, “Analysing the suspension system of variable-geometry oval-trajectory (VGOT) Darrieus wind turbines,” *Energy Sustain. Dev.*, vol. 12, no. 2, pp. 5–16, 2008.
- [21] T. Kinsey and G. Dumas, “Computational Fluid Dynamics Analysis of a Hydrokinetic Turbine Based on Oscillating Hydrofoils,” *ASME J. Fluids Eng.*, vol. 134, no. 2, p. 021104, 2012.
- [22] T. Kinsey and G. Dumas, “Three-Dimensional Effects on an Oscillating-Foil Hydrokinetic Turbine,” *ASME J. Fluids Eng.*, vol. 134, no. 7, p. 071105, 2012.
- [23] T. Kinsey, G. Dumas, G. Lalande, J. Ruel, a. Méhut, P. Viarouge, J. Lemay, and Y. Jean, “Prototype testing of a hydrokinetic turbine based on oscillating hydrofoils,” *Renewable Energy*, vol. 36, no. 6, pp. 1710–1718, 2011.
- [24] É. Gauthier, T. Kinsey, and G. Dumas, “Impact of blockage on the hydrodynamic performance of oscillating-foils hydrokinetic turbines,” vol. 138, no. 9, p. 091103, 2016.
- [25] P. Delafin, T. Nishino, L. Wang, A. Kolios, and T. Bird, “Comparison of RANS CFD and lower-order aerodynamic models for 3D Vertical Axis Wind Turbines,” *Eur. Wind Energy Conf. Exhib.*, 2015.
- [26] M. H. Mohamed, A. M. Ali, and A. A. Hafiz, “CFD analysis for H-rotor Darrieus turbine as a low speed wind energy converter,” *Eng. Sci. Technol. an Int. J.*, vol. 18, no. 1, pp. 1–13, 2015.
- [27] W. Yamazaki and Y. Arakawa, “Inexpensive airfoil shape optimization for vertical axis wind turbine and its validation,” *J. Fluid Sci. Technol.*, vol. 10, no. 2, 2015.
- [28] Q. Xiao, W. Liu, and A. Incecik, “Flow control for VATT by fixed and oscillating flap,” *Renewable Energy*, vol. 51, pp. 141–152, 2013.
- [29] Y. C. Lim, W. T. Chong, and F. B. Hsiao, “Performance investigation and optimization of a vertical axis wind turbine with the omni-direction-guide-vane,” *Procedia Eng.*, vol. 67, pp. 59–69, 2013.
- [30] W. T. Chong, A. Fazlizan, S. C. Poh, K. C. Pan, W. P. Hew, and F. B. Hsiao, “The design, simulation and testing of an urban vertical axis wind turbine with the omni-direction-guide-vane,” *Appl. Energy*, vol. 112, pp. 601–609, 2013.
- [31] R. Gosselin, G. Dumas, and M. Boudreau, “Parametric study of H-Darrieus vertical-axis

- turbines using uRANS simulations,” *21st Annu. Conf. CFD Soc. Canada*, vol. 178, 2013.
- [32] F. Balduzzi, A. Bianchini, R. Maleci, G. Ferrara, and L. Ferrari, “Critical issues in the CFD simulation of Darrieus wind turbines,” *Renewable Energy*, vol. 85, pp. 419–435, 2016.
- [33] P. Chatterjee and R. N. Laoulache, “Performance Modeling of Ducted Vertical Axis Turbine Using Computational Fluid Dynamics,” *Mar. Technol. Soc. J.*, vol. 47, no. 4, 2013.
- [34] A. Untaroiu, H. G. Wood, P. E. Allaire, and R. J. Ribando, “Investigation of Self-Starting Capability of Vertical Axis Wind Turbines Using a Computational Fluid Dynamics Approach,” *J. Sol. Energy Eng.*, vol. 133, no. 4, p. 041010, 2011.
- [35] M. R. Castelli, A. Englaro, and E. Benini, “The Darrieus wind turbine: Proposal for a new performance prediction model based on CFD,” *Energy*, vol. 36, no. 8, pp. 4919–4934, 2011.
- [36] M. R. Castelli, G. Pavesi, L. Battisti, E. Benini, and G. Ardizzone, “Modeling Strategy and Numerical Validation for a Darrieus Vertical Axis Micro-Wind Turbine,” *Int. Mech. Eng. Congr. Expo.*, vol. Vol. 7, no. IMECE2010–39548, pp. 409 – 418, 2010.
- [37] F. Trivellato and M. Raciti Castelli, “On the Courant-Friedrichs-Lewy criterion of rotating grids in 2D vertical-axis wind turbine analysis,” *Renewable Energy*, vol. 62, pp. 53–62, 2014.
- [38] M. H. Mohamed, “Performance investigation of H-rotor Darrieus turbine with new airfoil shapes,” *Energy*, vol. 47, no. 1, pp. 522–530, 2012.
- [39] R. Howell, N. Qin, J. Edwards, and N. Durrani, “Wind tunnel and numerical study of a small vertical axis wind turbine,” *Renewable Energy*, vol. 35, no. 2, pp. 412–422, 2010.
- [40] H. Beri and Y. Yao, “Effect of Camber on Airfoil on Self Starting of Vertical Axis Wind Turbine,” *J. Environ. Sci. Technol.*, vol. 4, no. 3, pp. 302–312, 2011.
- [41] B. Yang and C. Lawn, “Fluid dynamic performance of a vertical axis turbine for tidal currents,” *Renewable Energy*, vol. 36, no. 12, pp. 3355–3366, 2011.
- [42] T. Maître, E. Amet, and C. Pellone, “Modeling of the flow in a Darrieus water turbine: Wall grid refinement analysis and comparison with experiments,” *Renewable Energy*, vol. 51, pp. 497–512, 2013.
- [43] S. Lain and C. Osorio, “Simulation and evaluation of a straight-bladed darrieus-type cross flow marine turbine,” *J. Sci. Ind. Res. (India)*, vol. 69, no. 12, pp. 906–912, 2010.
- [44] A. Rossetti and G. Pavesi, “Comparison of different numerical approaches to the study of the H-Darrieus turbines start-up,” *Renewable Energy*, vol. 50, pp. 7–19, 2013.
- [45] C. J. S. Ferreira, H. Bijl, G. van Bussel, and G. van Kuik, “Simulating Dynamic Stall in a 2D VAWT: Modeling strategy, verification and validation with Particle Image Velocimetry data,” *J. Phys. Conf. Ser.*, vol. 75, p. 012023, 2007.
- [46] J. McNaughton, F. Billard, and a. Revell, “Turbulence modelling of low Reynolds number flow effects around a vertical axis turbine at a range of tip-speed ratios,” *J. Fluids Struct.*, vol. 47, pp. 124–138, 2014.

- [47] R. Lanzafame, S. Mauro, and M. Messina, “2D CFD modeling of H-Darrieus Wind Turbines using a transition turbulence model,” *Energy Procedia*, vol. 45, pp. 131–140, 2014.
- [48] M. S. Siddiqui, N. Durrani, and I. Akhtar, “Quantification of the effects of geometric approximations on the performance of a vertical axis wind turbine,” *Renewable Energy*, vol. 74, pp. 661–670, 2015.
- [49] M. R. Castelli, A. D. Monte, M. Quresimin, and E. Benini, “Numerical evaluation of aerodynamic and inertial contributions to Darrieus wind turbine blade deformation,” *Renewable Energy*, vol. 51, pp. 101–112, 2013.
- [50] S. M. Salim and S. C. Cheah, “Wall y^+ Strategy for Dealing with Wall-bounded Turbulent Flows,” *Int. MultiConference Eng. Comput. Sci.*, vol. II, 2009.
- [51] K. M. M. Almohammadi, D. B. B. Ingham, L. Ma, and M. Pourkashan, “Computational fluid dynamics (CFD) mesh independency techniques for a straight blade vertical axis wind turbine,” *Energy*, vol. 58, pp. 483–493, 2013.
- [52] T. Lee and Y. Y. Su, “Surface Pressures Developed on an Airfoil Undergoing Heaving and Pitching Motion,” *ASME J. Fluids Eng.*, vol. 137, no. 5, pp. 1–11, 2015.
- [53] J. Dacles-Mariani, G. G. Zilliac, J. S. Chow, and P. Bradshaw, “Numerical Simulations of a Wingtip Vortex in the Near Field,” *AIAA J.*, vol. 33, no. 9, pp. 1561–1568, 1995.
- [54] J. Dacles-Mariani, D. Kwark, and G. G. Zilliac, “On numerical errors and turbulence modeling in tip vortex flow prediction,” *Int. J. Numer. Methods Fluids*, vol. 30, pp. 65–82, 1999.
- [55] *ANSYS Inc., 2011. ANSYS FLUENT 14.0 Theory Guide*, URL: www.fluent.com.
- [56] M. F.R., “Two-equation eddy-viscosity turbulence models for engineering applications,” *AIAA J.*, vol. 32–8, no. 8, pp. 1598–1605, 1994.
- [57] F. R. Menter, M. Kuntz, and R. Langtry, “Ten Years of Industrial Experience with the SST Turbulence Model,” *Turbul. Heat Mass Transf. 4*, vol. 4, pp. 625–632, 2003.
- [58] F. R. Menter, R. B. Langtry, S. R. Likki, Y. B. Suzen, P. G. Huang, and S. Völker, “A Correlation-Based Transition Model Using Local Variables—Part I: Model Formulation,” *J. Turbomach.*, vol. 128, no. 3, pp. 413–422, 2004.
- [59] R. B. Langtry, F. R. Menter, S. R. Likki, Y. B. Suzen, P. G. Huang, and S. Völker, “A Correlation-Based Transition Model Using Local Variables—Part II: Test Cases and Industrial Applications,” *J. Turbomach.*, vol. 128, no. 3, p. 423, 2006.
- [60] I. Paraschivoiu, *Aérodynamique Subsonique*. Montreal Canada: Ed. École Polytechnique, 1998.
- [61] G. Naccache and M. Paraschivoiu, “Two Dimensional Flow Simulations of a Dual Axis Wind Turbine,” in *EIC Climate Change Technology Conference*, 2015.
- [62] P. J. Roache, “Perspective: A method for Uniform Reporting of Grid Refinement Studies,” *ASME J. Fluids Eng.*, vol. 158, pp. 109–121, 1993.

- [63] W. A. Timmer, “Two-dimensional low-Reynolds number wind tunnel results for airfoil NACA 0018,” *Wind Eng.*, vol. 32, no. 6, pp. 525–537, 2009.
- [64] M. S. Selig and J. J. Guglielmo, “High-Lift Low Reynolds Number Airfoil Design,” *J. Aircr.*, vol. 34, no. 1, pp. 72–79, 1997.
- [65] A. J. Fiedler and S. Tullis, “Blade Offset and Pitch Effects on a High Solidity Vertical Axis Wind Turbine,” *Wind Eng.*, vol. 33, no. 3, pp. 237–246, 2009.